FRM II
Forschungs-Neutronenquelle
Heinz Maier-Leibnitz

Jülich Centre for Neutron Science

HZB Helmholtz Zentrum Berlin

Helmholtz-Zentrum Geesthacht
Zentrum für Material- und Küstenforschung

Annual Report 2011

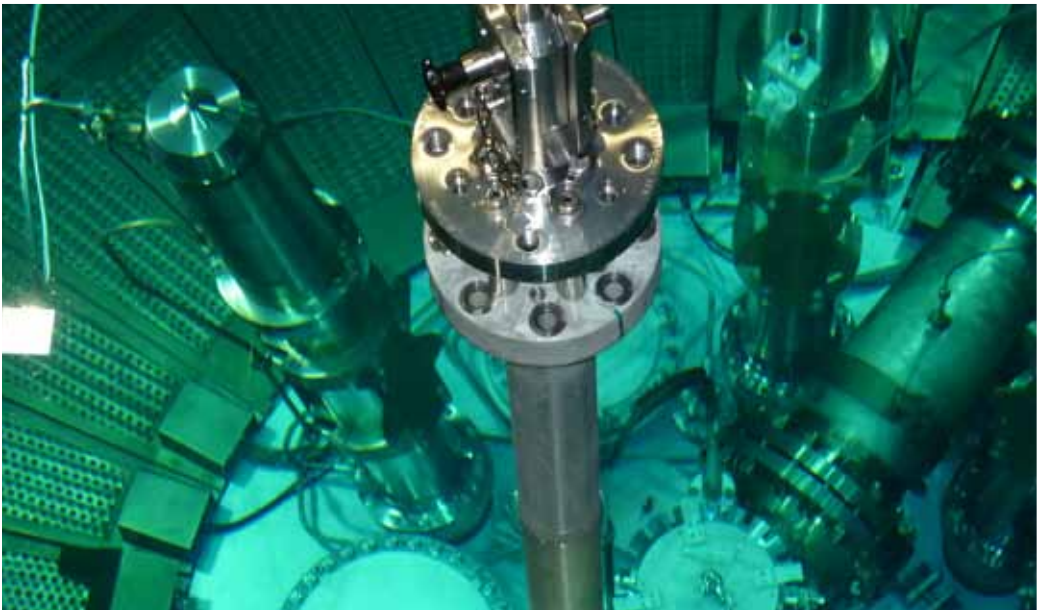

Technische Universität München
Forschungs-Neutronenquelle
Heinz Maier-Leibnitz (FRM II)
www.frm2.tum.de

Title images (clockwise, starting at the top left of the back side): Dismantling of the radiography instrument ANTARES; newly invented shielding material; Christian Breunig of the FRM II neutron optics group aligning new neutron guides; Dr. Michael Schulz (left) and a contractor dismantling parts of the beam tube of the positron source in a hot cell; the new green ANTARES shielding under construction; the old thimble of the high flux irradiation facility being removed from the reactor pool to make room for the new thimble to produce molybdenum-99.

FRM II Instrument Suite

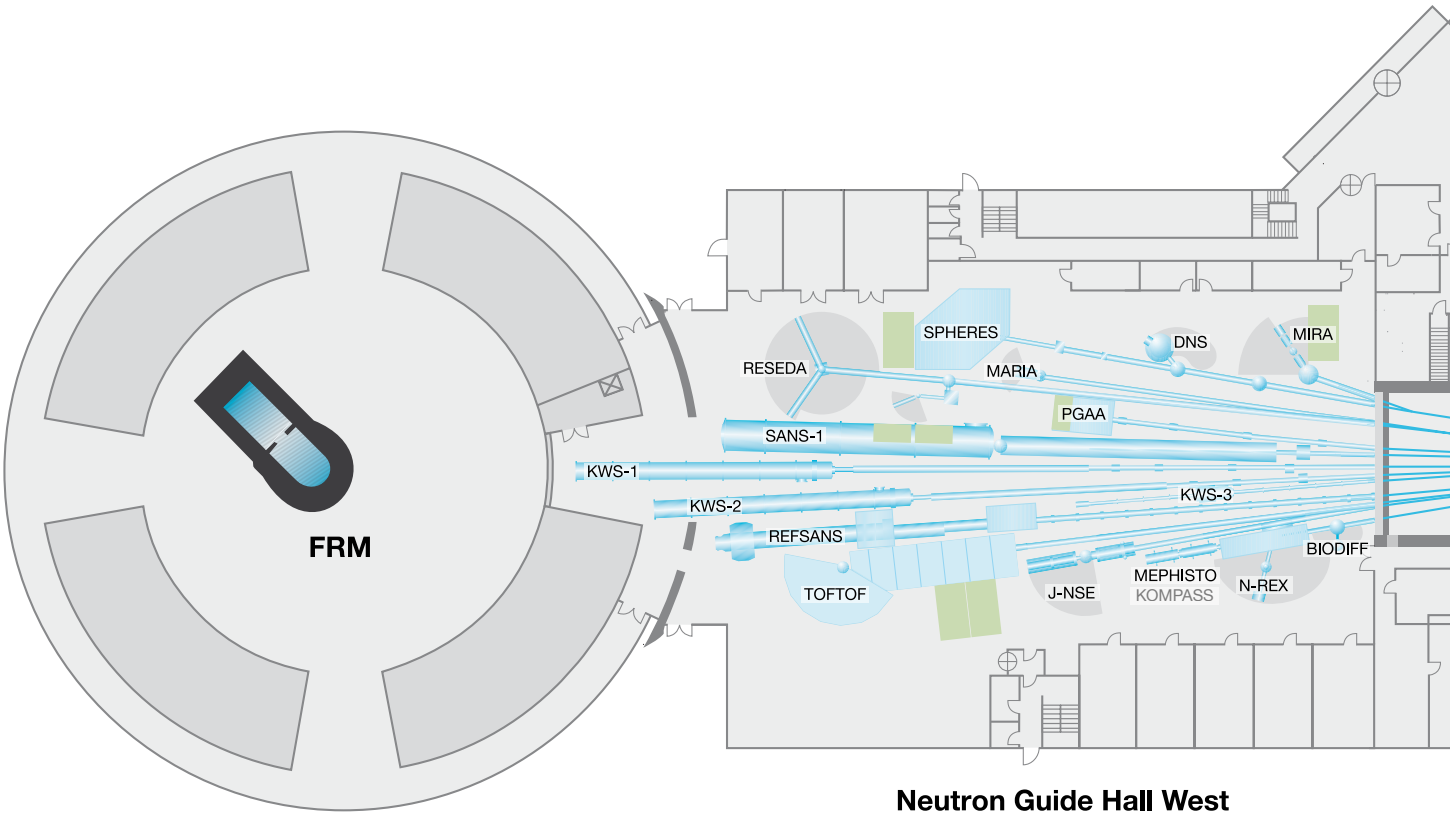

Instrument	Description	Neutrons	Status	Operated by
ANTARES	Radiography and tomography	cold	reconstruction until 2012	TUM
BIODIFF	Diffractometer for large unit cells	cold	operation	JCNS, TUM
DNS	Diffuse scattering spectrometer	cold	operation	JCNS
HEIDI	Single crystal diffractometer	hot	operation	RWTH Aachen, JCNS
J-NSE	Spin-echo spectrometer	cold	operation	JCNS
KOMPASS	Three axis spectrometer	cold	construction	TUM
KWS-1	Small angle scattering	cold	operation	JCNS
KWS-2	Small angle scattering	cold	operation	JCNS
KWS-3	Very small angle scattering	cold	operation	JCNS
MARIA	Magnetic reflectometer	cold	operation	JCNS
MEPHISTO	Facility for particle physics	cold	operation	TUM
MIRA	Multipurpose instrument	cold	operation	TUM
MEDAPP	Medical irradiation	fast	operation	TUM
NECTAR	Radiography and tomography	fast	operation	TUM
NEPOMUC	Neutron induced positron source	cold	reconstruction until 2012	UniBwM, TUM
NREX	Reflectometer with x-ray option	cold	operation	MPG
PANDA	Three axis spectrometer	cold	operation	TU Dresden, HZB

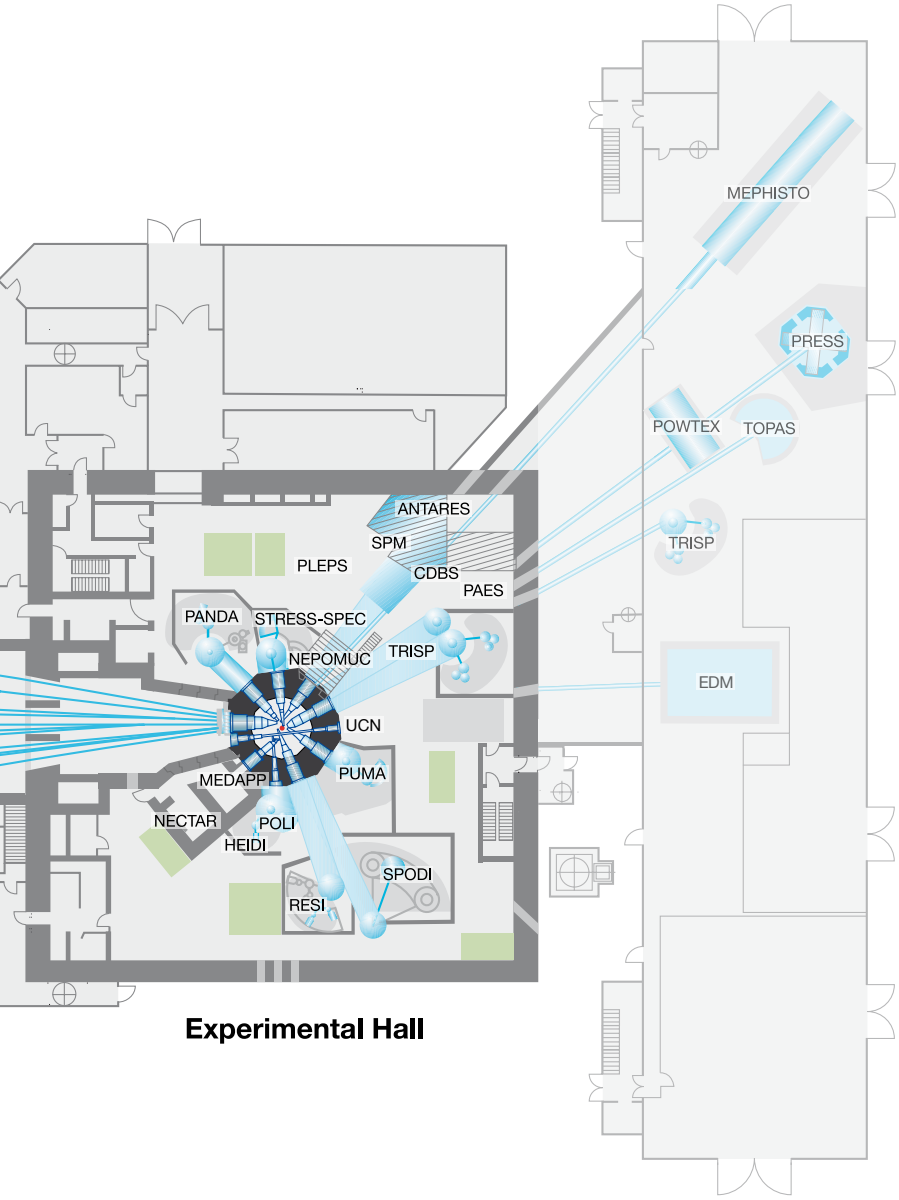

Experimental Hall

Neutron Guide Hall East

Instrument	Description	Neutrons	Status	Operated by
PGAA	Prompt gamma activation analysis	cold	operation	Uni Köln
PUMA	Three axis spectrometer	thermal	operation	Uni Göttingen, TUM
POLI	Polarized diffractometer	hot	construction	RWTH Aachen, JCNS
POWTEX	Time-of-flight diffractometer	thermal	construction	RWTH Aachen, Uni Göttingen, JCNS
PRESS	Time-of-flight diffractometer extreme environment	thermal	construction	BGI
REFSANS	Reflectometer	cold	operation	GEMS
RESEDA	Resonance spin-echo spectrometer	cold	operation	TUM
RESI	Single crystal diffractometer	thermal	operation	LMU, Uni Augsburg
SANS-1	Small angle scattering	cold	construction	TUM, GEMS
SPHERES	Backscattering spectrometer	cold	operation	JCNS
SPODI	Powder diffractometer	thermal	operation	LMU, TU Darmstadt, KIT
STRESS-SPEC	Materials science diffractometer	thermal	operation	TU Clausthal, TUM, GEMS
TOFTOF	Time-of-flight spectrometer	cold	operation	TUM
TOPAS	Time-of-flight spectrometer	thermal	construction	JCNS
TRISP	Three axis spin-echo spectrometer	thermal	operation	MPG
UCN	Ultra cold neutron source	cold	construction	TUM

Annual Report 2011
of the Scientific Cooperation
at the Forschungs-Neutronenquelle
Heinz Maier-Leibnitz (FRM II)

Content

Directors' Report

View of the neutron source
with reflection of the Atomic Egg.

1

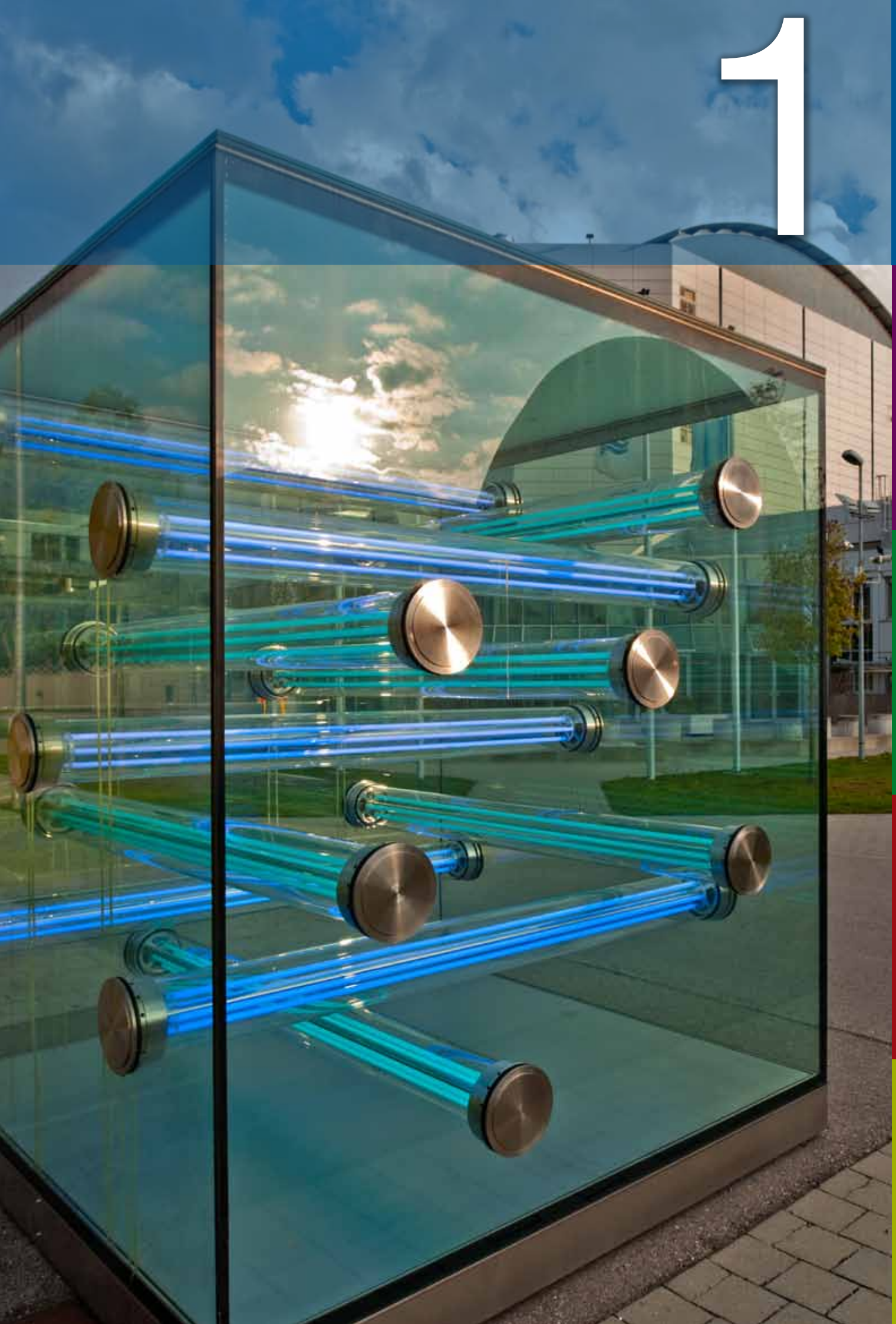

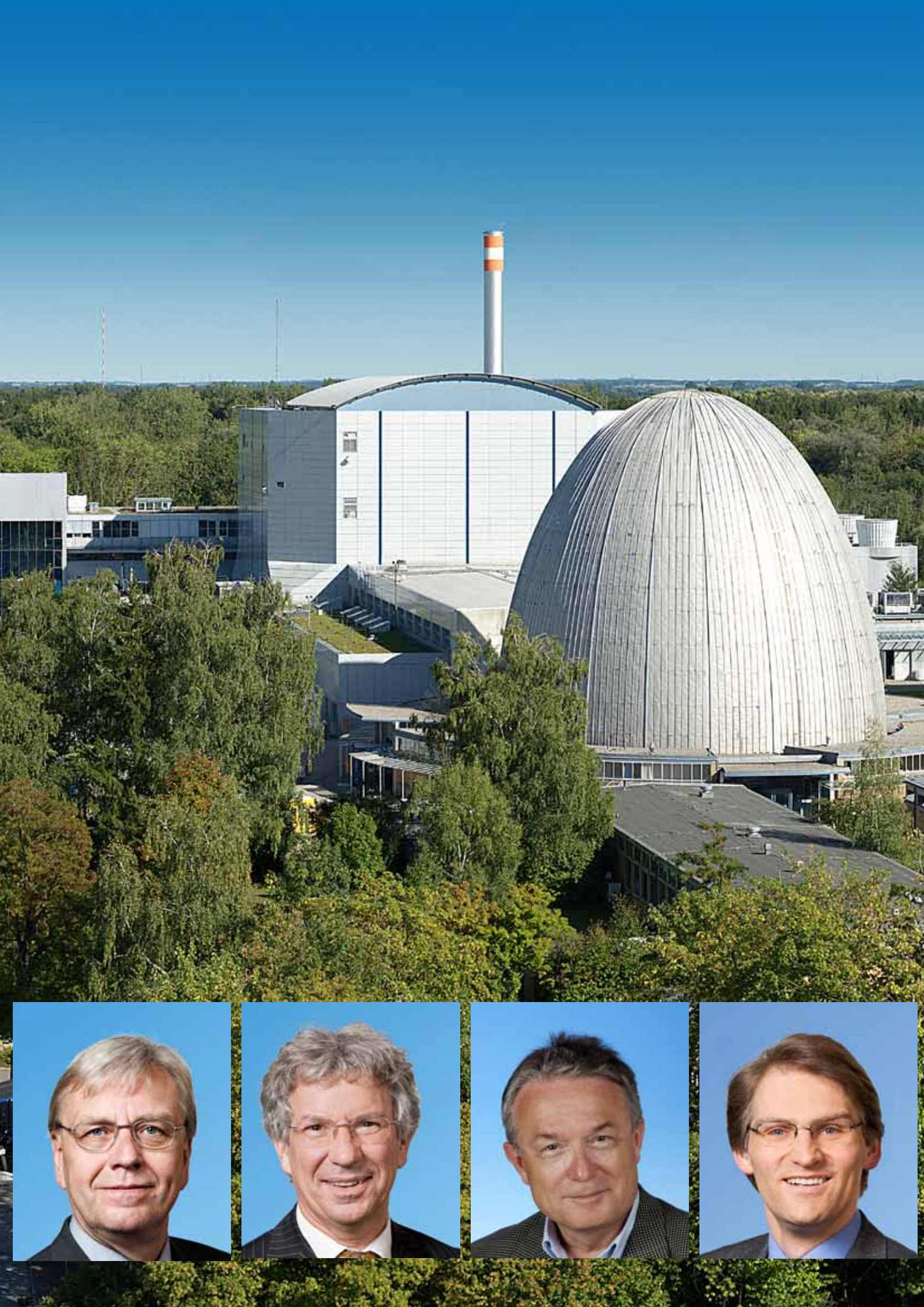

Directors' Report: New structures & instruments

On January 1st 2011, the scientific cooperation between the Technische Universität München and the Helmholtz centres at Jülich, Geesthacht and Berlin came into effect. Since then, the scientific use of the neutron source has been shared for the benefit of our international community. The Federal Government supports this cooperation with 20 million Euros per year, the Helmholtz centres have committed themselves to an additional 10 million Euros per year. Challenging tasks are to be fulfilled in the coming years. Reorganisation and the building up new structures to foster our successful partnership needs time. The cooperating partners have already expanded considerably in terms of staff during 2011. New positions and service groups such as that for scientific computing have been created.

The site of the FRM II will not only see more and newly organized staff, but also new facilities for neutron and positron experiments. With the expansion of the neutrons into the neutron guide hall east, new infrastructures and additional instruments will be provided. The instrumentation at FRM II now enters into its Phase III! This new guide hall will house six scientific instruments including those from the positron source NEPOMUC. It will be attached to the reactor building via an annex building. In accordance with the philosophy of the FRM patron Heinz Maier-Leibnitz that new instruments should aim for world leadership in at least one field, the instrument suite in the new guide hall will be exceptional: For example, the UCN source is to provide the world's highest flux of ultra cold neutrons, the newly constructed time-of-flight powder diffraction instrument POWTEX with its option for extreme environments at high pressure and temperature will simulate conditions in the inner earth. The thermal time-of-flight spectrometer TOPAS will offer full three dimensional polarisation analysis with thermal neutrons for the first time, opening a new chapter in the analysis of magnetic excitations.

The long maintenance break from the end of 2010 to 2011 has been successfully completed. Due to unfortunate circumstances following the earth quake and nuclear accident in Fukushima, some of the work was delayed and the safety authorities verified the preparedness of FRM II for simultaneous events such as earth quakes or flooding. Important modifications were able to be effected, such as the construction and insertion of a new thimble and the replacement of the secondary heat exchanger, both in preparation for the future production of molybdenum-99 (^{99}Mo). It was also in 2011 that the German Federal Ministry of Health awarded one million Euros for research and development for the efficient production of the cancer diagnostic agent ^{99}Mo. Furthermore, the entire beam tube for the positron source NEPOMUC has been exchanged. Equipped with a new insert, it will become available in autumn 2012. The placement of the radiography station ANTARES had to be changed in order to make way for an intense beam of cold neutrons for nuclear physics. Many other updates to instruments have successfully been finished. Now, both small angle cameras KWS 1 & 2 extend to 20 m long flight tubes, the time-of-flight spectrometer TOFTOF has acquired another 400 detectors, and the reflectometer MARIA and the single crystal diffractometer with complete polarization analysis POLI-HEIDI offer user-friendly operation.

Access to the FRM II is now via a clearly marked and friendly entrance hall connecting the gatehouse and the seminar room. Plans for two new central buildings in front of the Atomic Egg, replacing laboratory and office buildings from the 1950's, are already under way. They will provide urgently needed office space as well as laboratories and workshops.

We are looking forward to 2012. The year holds the promise of exciting experiments and results in neutron research, ensured by a full schedule of four reactor cycles.

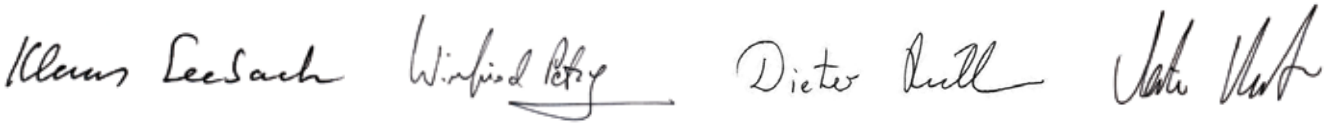

Klaus Seebach Winfried Petry Dieter Richter Anton Kastenmüller

The year in pictures

February 7th
The new thimble for the production of Molybdenum-99 is inserted into the reactor pool by FRM II staff.

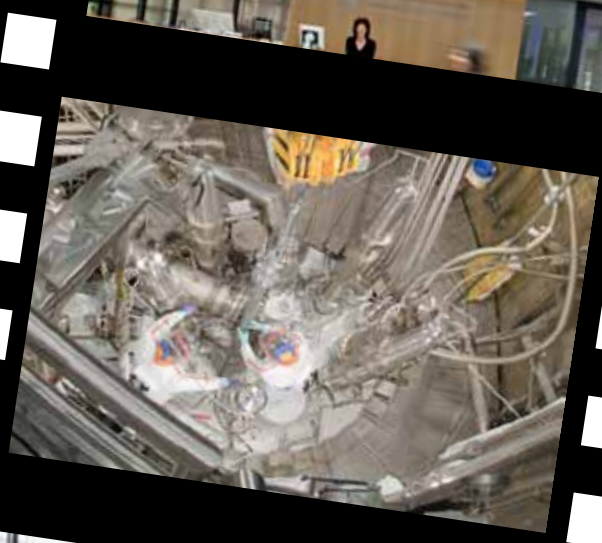

Feburary 21st
The German „Komitee Forschung mit Neutronen“ holds its meeting in the seminar room of the FRM II neutron research source.

March 25th
The lecture hall for 700 people is filled to capacity by staff of the Technische Universität München, listening to the talk of Dr. Anton Kastenmüller, Technical Director of the FRM II. He explains the background of the nuclear accident in Fukushima, Japan, and why such an incident cannot happen at the FRM II neutron research source.

March 28th
High-ranking guests at the Heinz Maier-Leibnitz colloquium in honour of his 100th birthday (from left): Prof. Dr. Matthias Kleiner, President of the German Research Foundation, Dr. Wolfgang Heubisch, Bavarian Minister for Science, Prof. Dr. Wolfgang A. Herrmann, President of the TUM, Prof. Dr. Winfried Petry, Scientific Director of the FRM II.

March 28th
Two founding fathers of the neutron source meet at the Heinz Maier-Leibnitz colloquium: Dr. Rainer Kuch (left) and Prof. Dr. Tasso Springer (right), who had worked at the Atomic Egg.

April 11th
Students of the Bayerische Elite Akademie visit the neutron source. Prof. Dr. Winfried Petry (second row, left) in his capacity as advisor of the physics department at the TUM to the Elite Akademie introduces the talented young women and men to neutron science.

May 15th
The new entrance hall of the FRM II is ready for visitors and users. It connects the gate house and the seminar room.

July 7th
As is the tradition at the neutron source, the staff is invited to a summer festival once a year. Tasty food and beverages as well as beautiful Bavarian sunshine are always included.

July 21st
Ten FRM II staff members take part in the company run „b2run" in Munich. Stefan Söllradl (5th from the left) comes in 31st taking 20:35 min. for the 6.4 km run.

July 30th
Two IT-apprentices at the FRM II IT service group completed their training with excellent grades and are congratulated by the Technische Universität München: Alexander Lenz (right) will continue to work in the field of software development at the FRM II, while and Christoph Kick (left) will go on with his training.

The year in pictures

August 9th
The PhD students Georg Brandl (left) and Philipp Schmakat (right) supervise Claudio Polisseni, a student on the DAAD exchange program (RISE) from Imperial College London, during a practical course at the instrument MIRA.

August 11th
The conservation area of the FRM II has become a nature reserve for all kinds of rare animals and plants.

August 15th
Josef Waronitza completed his apprenticeship in mechatronics at the FRM II as one of the best students. He is also congratulated by the Technische Universität München as one of the best apprentices of the year.

September 15th
Students on the JCNS neutron lab course get the opportunity to visit the Atomic Egg, accompanied by Dr. Tobias Schrader, JCNS, and a former PhD student of the Technische Universität München, who performed his first experiments at the Atomic Egg.

October 15th
Well-attended on the open day of the Technische Universität München in Garching: Radiation protection at the FRM II, with Dr. Helmut Zeising (left) explaining the sources of natural radiation to the visitors.

October 29th
After the long maintenance break, the neutron source is restarted in small steps from 0.1 MW via 1 MW up to 20 MW maximum power.

November 8th
For the first time, members of the green party visit the neutron source. Accompanied by the FRM II directors Prof. Dr. Winfried Petry (left) and Dr. Anton Kastenmüller (second from right), Munich city council member Jutta Koller (second from left) and her colleague take a look into the reactor pool.

November 11th
New temporary offices at the site of the FRM II are completed. They are located next to the industrial application centre.

November 25th
15 public relations managers from neutron sources all over Europe meet for the first time at the Heinz Maier-Leibnitz research neutron source to exchange PR-concepts and form a network.

December 11th
Happy users from Japan measuring at the JCNS instrument KWS 2 in the first full reactor cycle in 2011.

Instruments & Methods

Sample position at the new small angle neutron scattering instrument SANS-1.

2

Higher, faster, further: Instrumental improvements

T. Bücherl[1], R. Georgii[1], Ch. Hugenschmidt[1], Y. Khaydukov[3], J. Neuhaus[1], A. Ostermann[1], Z. Revay[1], B. Schillinger[1], T. Schrader[2], F.M. Wagner[1]

[1]Technische Universität München, Forschungs-Neutronenquelle Heinz Maier-Leibnitz (FRM II), Garching, Germany

[2]Forschungszentrum Jülich GmbH, Jülich Centre for Neutron Science at FRM II, Garching, Germany

[3]Max-Planck-Institute for Solid State Research, Stuttgart, Germany

Almost every one of the 24 instruments operating at the Heinz Maier-Leibnitz neutron source has undergone a refurbishment during the long reactor shutdown. As a result, they are faster in changing their positions, have a higher neutron flux or are equipped with an improved control software.

World record flux and lowest background

The reconstruction of the PGAA facility had two purposes. First, the radiation background had to be reduced, both in terms of dose rate and spectra. A solution also had to be found so that the instrument could be used in medium- and high-flux modes without any constraints. As a consequence of the reconstruction, the facility can now be used in any mode. Besides a medium-flux working beam suitable for routine applications, a high-flux beam for special applications also became available. It then becomes a simple matter to change from one to the other mode (see fig. 1). As a result of the modifications, the spectral background became an order of magnitude lower in all measuring modes, so that a dynamic range of almost three orders of magnitude is now available for useful spectrum counts in standard PGAA, and more than an order of magnitude in the high-flux mode.

Figure 1: A moving mechanism changes the beam collimator and the elliptical neutron guide (back part) at the PGAA.

This provides an uniquely low signal-to-background ratio in standard PGAA, but also enables the measurement of extremely low-mass or low-cross-section samples in high neutron flux; for instance, it is possible to determine major and minor elements (i.e. those with concentrations above 1%) in the range of microgram and certain trace elements below 1 ng.

When using the focusing guide element, a thermal flux of $6 \cdot 10^{10}$ cm^{-2} s^{-1}, the highest reported beam flux, was achieved.

Weight reduction at ANTARES

While other instruments have added or improved components, the radiography and tomography facility ANTARES has been completely dismantled. The ANTARES-team removed 550 tons of shielding to make room for a new guide feeding the future guide hall east with cold neutrons. This involved tearing off of the platform of the positron source NEPOMUC. ANTARES has filled its new green shielding (fig. 2) using a recyclable shielding material and installed it in the experimental hall. The material has, and maintains, the consistency of wet sand and does not solidify. Since the new material contains only elements that

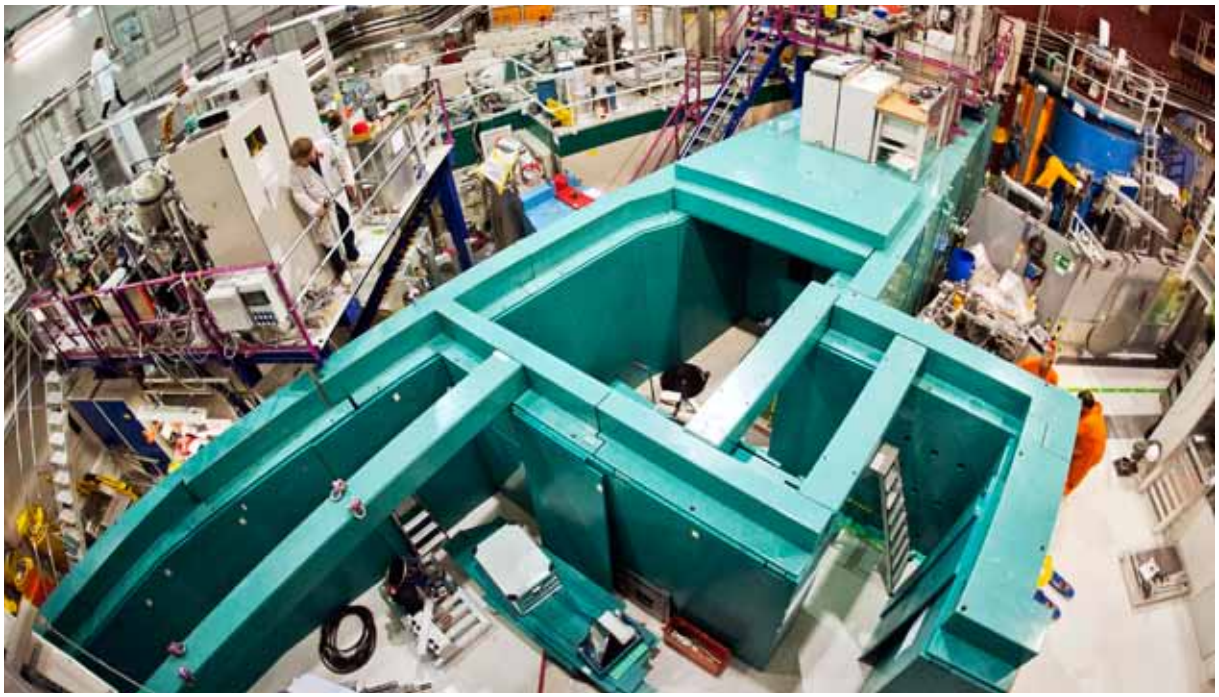

Figure 2: The newly constructed ANTARES facility uising the patented shielding material saving weight and space.

contribute significantly to radiation shielding, the total thickness can be reduced by 20 percent as compared to heavy concrete, saving more than 50 tons of weight in the case of ANTARES. The Technische Universität München has patented this invention. The new ANTARES will offer two measuring positions, an improved resolution, and polarised and monochromatic neutrons. The restart is anticipated for the second half of 2012.

New irradiation site at SR10 (MEDAPP)

The facility for tumour irradiation at the FRM II, MEDAPP, performed 24 irradiations on 4 patients during the last cycle in 2011. A new irradiation site at the lid of beam tube SR10 has been set up where technical objects can be irradiated with a thermal beam of high purity and an area of 23 x 18 cm. A new lamellar collimator is under development.

Larger beam area for NECTAR

The NECTAR radiography and tomography station has been equipped with a new beam stop made of the newly developed shielding material for ANTARES. This allows for a neutron beam with higher intensity and cross section area, as is required for the real time radiography of technical objects with fast neutrons.

PANDA is newly wired

Major improvements and upgrades were carried out at PANDA in 2011. A decentralized motor control was prepared and some devices (control of analyser blocks, attenuator, slits) acquired new control electronics as well as a corresponding software. Also, the main motor control electronics was rearranged into units supporting all necessary connections for 8 axes.

The new Göttingen triple motor cards were integrated as well as additional diagnostics. A new electronics box to change the monochromator during an experiment was designed, built and commissioned. Its control is included in the new and upgraded instrument control software NICOS2. The software now also includes a lot of new features: state persistence, status monitor, experiment management and a central cache containing the whole instrument state at any given time.

Positron source to restart in 2012

After the replacement of the beam tube SR11 including the in-pile positron source and the subsequent restart of the FRM II, an insufficient heat bridge between the second barrier and the beam tube caused an unexpected increase in the tem-

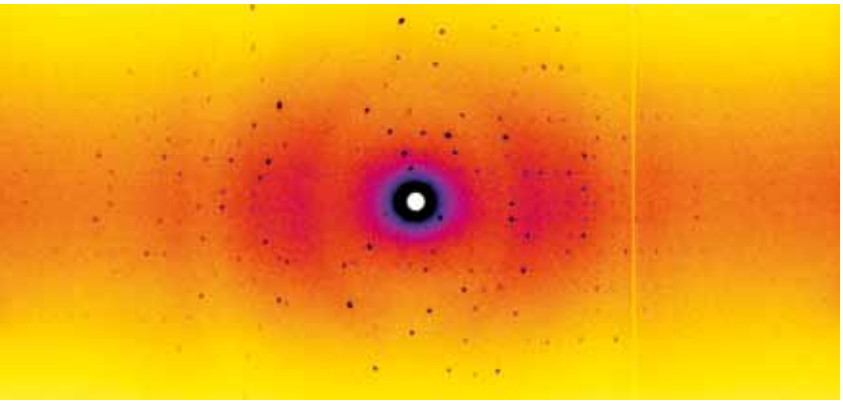

Figure 3: Image obtained by the image plate detector of the instrument BIODIFF.

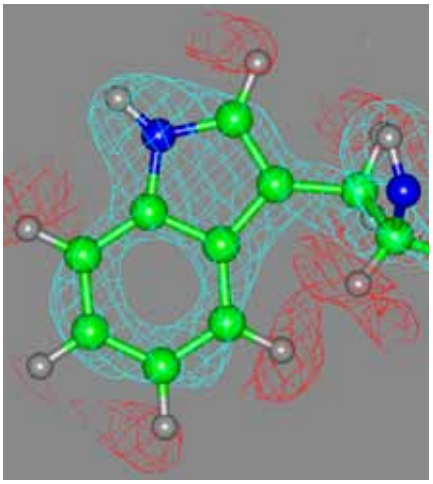

Figure 4: First calculated nuclear map of a myoglobin crystal showing as an example the tryptophan residue no. 7, contour map at +1.5 σ (cyan, indicating C, N and ^{2}H) and at -1.5 σ (red, indicating ^{1}H).

perature. For this reason, the second barrier and the innermost experimental tube, were removed while the outer beam tube including the new Cd converter, remained in place. Experiments at the NEPOMUC positron beam facility are due to restart in late 2012.

General overhaul of NREX

The neutron reflectometer NREX (fig. 5), operated by the Max Planck Society, has undergone a general overhaul. The instrument has acquired new software, new detector electronics, new polarizers and a new focusing monochromator. As a result, the operation is now more stable and the handling easier. NREX now provides up to three times more flux and features a reduced background. Further improvements include a wide aperture polarisation analyser and an advanced sample cell for solid/liquid interfaces.

High pressure measurements at TRISP

The three-axes spectrometer TRISP has been upgraded to a new dilution cryostat with a cooling power of 400 µW at 100 mK which also provides space for large samples, i.e. for high pressure measurements. It reaches temperatures down to 8 mK.

MIRA has increased intensity

A newly focusing monochromator increases the intensity at MIRA and makes it even more attractive. The diffractometer has been optimized for a fast change between different operating modes, three-axes measurements, small angle scattering and MIEZE. Hard- and software for the instrument control have been exchanged and the sample environment revised. MIRA now also owns a new area detector for SANS and MIEZE measurements.

More detectors at TOFTOF

The time-of-flight spectrometer TOFTOF had the number of its detectors increased from 605 to 1006, resulting in shorter measuring times. Further improvements include new detector electronics and enhanced electronic shielding, which leads to a reduced and more stable background. The insertion of an adaptive optics focusing neutron guide has been finished. The intensity gain is up to 2.5 fold, especially for cold neutrons The background from the sample is lower at all wavelengths.

Users welcome at BIODIFF

During the maintenance break, the new biological diffractometer BIODIFF was equipped with a velocity selector and an image plate detector system is now available for scientifc experiments. Within the first cycle after the break, first crystallographic data sets were recorded on a myoglobin crystal with both detector systems of BIODIFF: the CCD-camera and the image plate detector. A typical detector image is depicted in figure 3. A nuclear density map calculated from a data-set recorded with the image plate detecto within 9 days of beam time is shown in figure 4.

Laser system at SANS-1

Not yet in operation, but on the home straight is the new small angle scattering instrument SANS-1. The shielding around the collimation area and the velocity selector has been strengthened and a new one constructed at the sample position. The fully automated sample positioning and the safety control system have been installed. Furthermore, first neutron tests on the large area detector integrated in the 22 m detector tank have been successfully performed using a laboratory source. SANS-1 has a laser system to check the position of all optical components, which has been installed and adjusted (fig. 6).

20 percent higher flux at RESI

Time saving at the single crystal diffractometer RESI: The new mechanics of the monochromator saves several days of adjustment and guarantees a better focus control. An encoder allows for a fast change of positions. A twenty percent higher neutron flux has been achieved thanks to a new adjustment. RESI will soon provide an additional Laue camera. The beam exit and sample table have already been prepared. The peak integration software of the single crystal diffractometer is now available for academic use, rather than under commercial licence.

Figure 5: The N-REX reflectometer has undergone a general overhaul.

RESEDA with MIEZE option

A new CASCADE detector has been successfully commissioned at the resonance spin echo spectrometer RESEDA. The MIEZE option is now available.

Extended Q-range at KWS 3

The small angle scattering instrument KWS 3 underwent some crucial changes during the maintenance phase: It has been equipped with a new sample chamber, beam stop changer, entrance aperture and software. The Q-range was extended to $4{\cdot}10^{-5}$ - $3{\cdot}10^{-2}$ $Å^{-1}$. The flux boosted three times.

Figure 6: The SANS-1 team working on the collimation of the small angle scattering instrument. The laser system is visible on the left.

^{3}He spin filters for spherical neutron polarimetry at the new single crystal diffractometer POLI@HEiDi

V. Hutanu[1], M. Meven[2], S. Masalovich[2], G. Heger[1], G. Roth[1]

[1]RWTH Aachen University, Institute for Crystallography, Aachen, Germany

[2]Technische Univerisität München, Forschungs-Neutronenquelle Heinz Maier-Leibnitz (FRM II), Garching, Germany

Spherical Neutron Polarimetry (SNP) is a powerful method for the detailed investigation of complex magnetic structures. The precise control of the in-coming and scattered neutron polarisation is essential for this technique. Here, we show a method that has recently been implemented on the new single crystal diffractometer POLI@HEiDi (POLI) at the FRM II to perform SNP experiments using two ^{3}He spin filters for the production and analysis of neutron polarisation. Dedicated spin filter cells and the correction procedure for the time dependent relaxation were developed. Statistical precision of 1 % has been achieved for the measurements of the polarisation matrix under real experimental conditions.

Gaseous ^{3}He neutron spin filter cells (SFC) are simple transmission devices, with predictable characteristics, that do not require any special optical adjustments on a neutron beam. Since the polarized nuclei of ^{3}He possess very high spin-dependent neutron absorption efficiency over a wide range of energies, the ^{3}He SFC can be used as a broadband neutron polariser or analyser, with the possibility of optimising its efficiency for nearly all neutron wavelengths. However, SFC is particularly efficient in combination with hot neutrons. According to the calculations [1] the combination of the focused Cu [2 2 0] crystal monochromator with ^{3}He spin filter with 70 % He polarisation will increase the efficiency of the instrument in the production of the hot polarised neutron beam by a factor 1.7 as compared to a Heussler monochromator. It is precisely this design that has been used in the new polarised diffractometer POLI. The drawback is a degradation in the incident beam polarisation and analysing efficiency of an analyser with time. When using two SFC as polariser and analyser at the same time, the resulting polarisation measured includes a product of two independent time functions. The correction is only possible if the polarisation of the ^{3}He gas in the polariser and analyser are measured independently. Only when precise control of the in-coming polarisation has been developed and corrections for the time-dependent depolarisation performed do measurements of the polarisation matrices with the required precision POLI become possible [2].

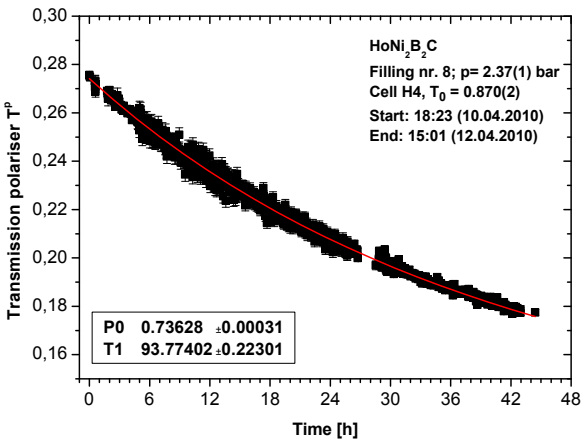

Figure 1: Time-dependent transmission of the polariser cell measured using two transmission monitors situated before and after the polariser. The result of the least squares fit of ^{3}He initial polarisation and T_1 according to equation 1 are given in the inset.

Measurements and corrections of the data

In SNP, the usual experimental strategy is to measure the scattered beam polarisation P' when the incident polarisation P is set alternatively along x, y or z axis. This determines the polarisation matrix. The matrix element P'_{ij} gives the i^{th} component of the scattered polarisation vector when the incident polarisation is in the j^{th} direction. Using the time marking and the same time scale for the polariser and analyser, the precise measurement of P'_{ij} is possible. The incident polarisation at the moment t_m $P(t_m)$ is calculated precisely using transmission measurements

$P_{in.}$ / $P_{out.}$	Asymmetry as measured			Corrected polarisation matrix		
	x	y	Z	x	y	z
x	0,730(3)	0,003(5)	0,009(5)	0,99(1)	-0,00(1)	0,01(1)
y	0,030(5)	0,714(3)	-0,006(5)	0,04(1)	0,98(1)	-0,01(1)
z	0.001(5)	0,005(3)	0,715(3)	-0,00(1)	0,00(1)	0,99(1)

Table 1: Polarisation matrices for nuclear Bragg peak "as measured" and corrected for ^{3}He relaxation.

from two neutron monitors, placed in front of and behind the polariser. Figure 1 shows an example of the time-dependent measured transmission in one particular experiment. Transmission of the spin filter calculated for a non-polarised beam depends on a ^{3}He gas polarisation in the cell as:

$T^P(t) = T_0^P e^{-O^P} \cosh(O^P P^p_{He}(t))$ [equation 1],

where T_0^p is the transmission of the empty polariser cell, O^P is the opacity of the polariser cell depending on cell geometry and pressure, $P^p_{He}(t)$ is the time dependent polarisation of ^{3}He gas in the polariser cell. Fitting the experimental transmission data using this equation results in precise values for the ^{3}He initial polarisation and T_1 of the polariser cell (inset fig. 1). The measurement of the scattered polarisation matrix element P'_{ij} requires precise knowledge of the time-dependent analysing efficiency $A_n(t)$:

$A_n(t) = \tanh(O^a P_{He}^a(0) \exp(-t/T_1^a))$ [equation 2],

where O^a is the opacity of the analyser cell, $P_{He}^a(0)$ is the polarisation of the ^{3}He gas at the time moment zero (initial gas polarisation), T_1^a is the relaxation time constant of the analyser.

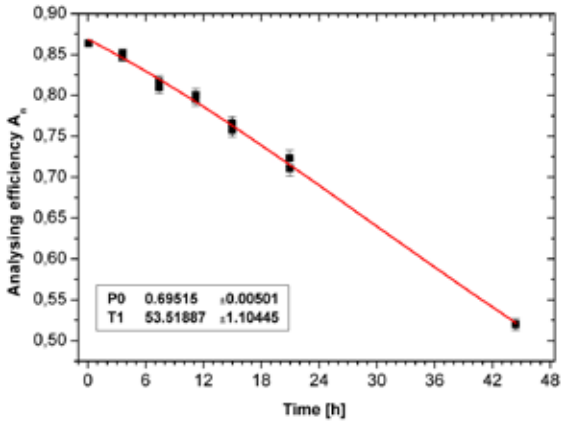

Figure 2: Measured time dependent analysing efficiency of an analyser cell. The result of the least squares fit gives the ^{3}He initial polarisation and T_1 according to equation. 2.

Using known O^a the problem reduces to the determination of the initial polarisation and T_1^a in the analyser. Time dependent measurements of non-magnetic Bragg reflection permits, however, a direct measurement of $A_n(t)$. In this particular case $A_n(t)$ can easily be found by normalising measured asymmetry to the incoming polarisation measured earlier. Taking the predefined O^a to be a fixed parameter and fitting $A_n(t)$ to measured data using equation 2, one obtains the required parameters of the analyser cell: $P_{He}^a(0)$ and T_1^a. Figure 2 shows an example of the time-dependent analyser efficiency calculated for the set of experimental data presented in figure 1, measured with nuclear Bragg peak.

High resolution and optimal efficiency assured

Measured and corrected polarisation matrices for the nuclear [200] Bragg reflection in the $HoNi_2B_2C$ sample are presented in table 1. The measurements were made at 4.2 K using neutrons with a wavelength of 0.87 Å.

Spin filter cells with optimised parameters are employed to produce and analyse neutron polarisation at the new polarised diffractometer POLI (RWTH Aachen) at FRM II. The use of SFC assures high resolution and optimal efficiency for hot neutrons. SNP using third generation zero-field polarimeter Cryopad for the investigation of the complex magnetic structures is implemented on POLI. The correction procedure for the time-dependent polariser (analyser) efficiency has been developed and successfully applied.

[1] E. Lelievre-Berna and F. Tasset, Physica B, 267, 21 (1999).

[2] V. Hutanu et al., J. Phys.: Conf. Ser., 294, 012012 (2011).

Solid oxygen as converter for the production of ultra-cold neutrons

A. Frei[1], F. Böhle[2], R. Bozhanova[2], E. Gutsmiedl[2], T. Huber[2], J. Klenke[1], S. Paul[2], R. Stoepler[2], S. Wlokka[2]

[1]Technische Universität München, Forschungs-Neutronenquelle Heinz Maier-Leibnitz (FRM II), Garching, Germany

[2]Technische Universität München, Physik Department, Garching, Germany

We have investigated solid oxygen as converter material for the production of ultra-cold neutrons (UCN). In a first series of experiments, the crystal preparation was examined. An optically semi-transparent solid α-oxygen crystal was produced. In a second series crystals, prepared identically to the first ones, were exposed to the cold neutron flux of the MEPHISTO beam line at the FRM II. UCNs, produced inside the oxygen crystal were extracted and the count rates measured at different converter temperatures. The results of these measurements gave a clear signal of the super-thermal UCN production mechanism in α-oxygen. The mean free loss length of UCN inside the crystal at a temperature of 7 K was determined to be of the order of 20 cm. This is the first experimental proof of UCN production by magnonic and phononic crystal excitations in solid α-oxygen.

Anomaly with solid oxygen crystals

Precision experiments with ultra-cold neutrons, such as the search for a possible electric dipole moment or the measurement of the lifetime of the free neutron, require high UCN densities. At the FRM II [1,2], and worldwide, stronger UCN sources are presently being developed, based on the principle of super-thermal UCN production [3,4], using cryo-converters made of solid deuterium, superfluid helium or solid oxygen. Until now, promising results have been achieved with converters made of deuterium or helium. Another very promising candidate is solid oxygen, where UCN can be produced via phonon and magnon excitations in the crystal lattice [5]. It has a large inelastic scattering cross section and a small nuclear absorption cross section, and therefore offers the possibility of realizing large (several decimeters) converters with high UCN production rates. Experimentally, the neutron scattering cross sections and UCN production cross sections of solid α-oxygen have been investigated by different groups [6,7], concluding that the UCN production rate should increase by cooling down the solid oxygen crystal to temperatures below 20 K. However, direct measurements of the UCN count rates from such crystals conducted recently could not confirm the anticipated results [8]. On the contrary, the measured UCN count rates decreased when lowering the crystal temperature. The reason for this is unknown. Losses due to UCN-extraction out of the oxygen crystal are one possible explanation for this anomaly.

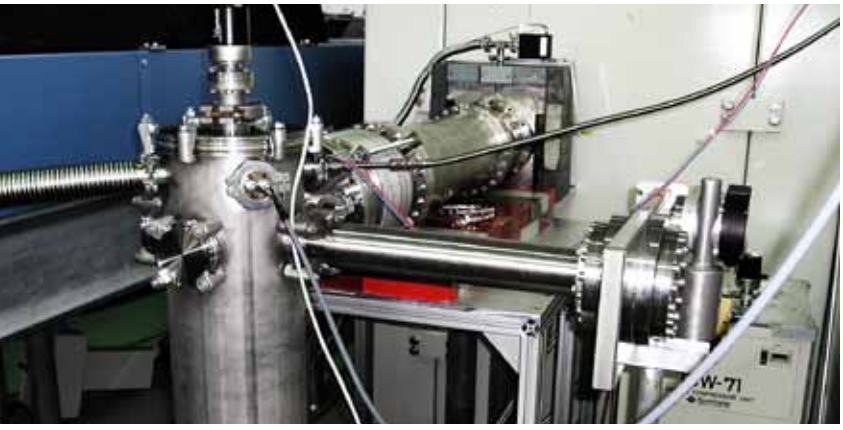

Figure 1: Experimental setup (partially dismantled) at MEPHISTO. The sample cell is placed inside the stainless steel vacuum chamber on the left side and irradiated by cold neutrons arriving from the back side of the picture. UCN are extracted perpendicular to the incoming beam, and guided to a detector (not shown).

Measurements at the cold beam line MEPHISTO

The converter cell was placed in the cold neutron beam line MEPHISTO at the FRM II. UCN produced were extracted horizontally and guided perpendicularly to the incoming beam through a thin aluminium window to an UCN detector (see fig. 1).

To prepare the solid α-oxygen converter, the cool down rates especially at the solid-solid phase

Figure 2: Pictures of the oxygen crystal at different phases. Top left: Liquid oxygen in the sample cell (partially filled). Top right: Transparent γ-oxygen (sample cell completely filled). Bottom left: Cloudy β-oxygen. Bottom right: Cloudy α-oxygen.

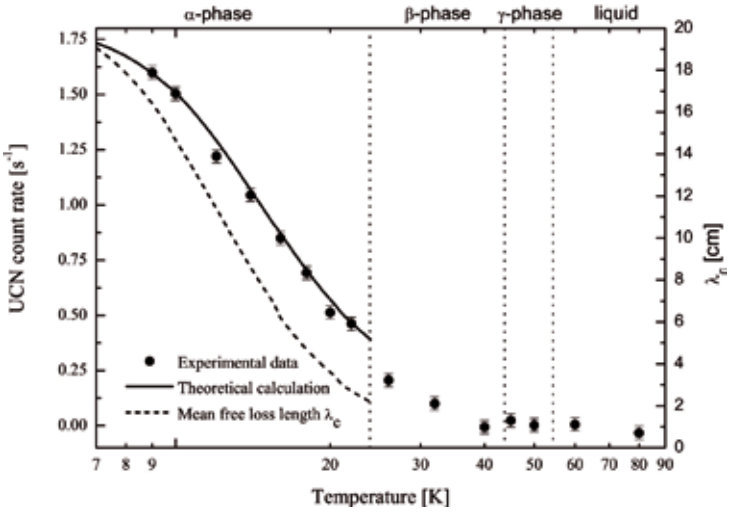

Figure 3: Circles: Measured UCN count rates produced by a solid oxygen converter, depending on its temperature and solid state phase. Error bars indicate statistical uncertainties. Solid line: Calculated UCN count rate. Dashed line: Mean free loss length λ_c (axis to the right) in the oxygen converter used for the calculations.

transitions were optimized, and the crystal was optically inspected. An optically non transparent sample is a polycrystalline sample, leading to additional losses of UCN being scattered at the polymorphic cell boundaries. At the transition liquid ↔ γ, which occurs at 54.4 K at vapour pressure, and at the transition β ↔ α, occurring at 23.9 K, the cooling rate had no influence on the transparency of the resulting crystal. The cooling rates were varied in the range of 1.0 to 0.1 K/h. The γ ↔ β phase transition is a polymorphic transformation at a temperature of 43.8 K. This transition is critical in respect of the optical transparency of the resulting β-crystal. In our experiments, we found that only at cooling rates below 10 mK/h the resulting β-crystal was optically cloudy having a blue colour. At faster cooling rates the resulting β-crystal was completely black and optically opaque. Figure 2 shows the different crystals described above.

UCN increase with decreasing temperature

In figure 3 the UCN count rates measured at different temperatures of the oxygen converter are depicted. The UCN count rate increases with decreasing temperature. This trend is a clear indication of the theoretically anticipated UCN production and extraction mechanism via the super-thermal principle of detailed balance. Based on theoretical models these measured values have been fitted, with the mean free loss length λ_c of UCN inside of the sample as a fit parameter, resulting in $\lambda_c \approx 20$ cm at T = 7 K.

Useable converter size of 20 cm

In summary, we have developed a method to produce an optically semi-transparent solid oxygen crystal in its α-phase. The solid oxygen converter has been exposed to a cold neutron beam, and the UCN count rates have been measured. The measured temperature dependence of the UCN count rate can be explained with theoretical models of a super-thermal UCN production mechanism. The usable converter size was determined to be of the order of 20 cm, a value that is significantly smaller than the theoretical neutron absorption length of 380 cm, but also significantly higher than the UCN loss lengths of several mm, measured by other groups. This discrepancy motivates further measurements and improvements in this field of research.

[1] U. Trinks et al., Nucl. Instr. Meth. A, 440, 666 (2000).
[2] A. Frei et al., Eur. Phys. J. A, 34, 119 (2007).
[3] R. Golub, J.M. Pendlebury, Phys. Lett. A, 53, 133 (1975).
[4] R. Golub et al., Z. Phys. B, 51, 187 (1983).
[5] C.-Y. Liu, A.R. Young, arXiv:nucl-th/0406004v1, (2004).
[6] F. Atchison et al., Nucl. Instrum. Methods Phys. A, 611, 252 (2009).
[7] E. Gutsmiedl et al., Europhys. Lett.. 96, 62001 (2011).
[8] F. Atchison et al., Europhys. Lett., 95, 12001 (2011).

Long-range crystalline nature of the skyrmion lattice in MnSi

T. Adams[1], S. Mühlbauer[1,2,3], C. Pfleiderer[1], F. Jonietz[1], A. Bauer[1], A. Neubauer[1], R. Georgii[1,2], P. Böni[1], U. Keiderling[4], K. Everschor[5], M. Garst[5], A. Rosch[5]

[1]Technische Universität München, Physik Department E21, Garching, Germany

[2]Technische Universität München, Forschungs-Neutronenquelle Heinz Maier-Leibnitz (FRM II), Garching, Germany

[3] Eidgenössische Technische Hochschule Zürich, Institut für Festkörperphysik, Zürich, Switzerland

[4]Helmholtz-Zentrum Berlin, Berlin Neutron Scattering Center, Berlin, Germany

[5]Universität zu Köln, Institute for Theoretical Physics, Köln, Germany

We report small angle neutron scattering of the skyrmion lattice in MnSi using an experimental set-up that minimizes the effects of demagnetizing fields and double scattering. Under these conditions the skyrmion lattice displays resolution-limited Gaussian rocking scans that correspond to a magnetic correlation length in excess of several hundred μm. This is consistent with exceptionally well-defined long-range order. We further establish the existence of higher-order scattering, discriminating parasitic double-scattering using Renninger scans. The field and temperature dependence of the higher-order scattering arises from an interference effect. It is characteristic of the long-range crystalline nature of the skyrmion lattice, as shown by mean field calculations.

In recent SANS experiments we investigated the skyrmion lattice as a six-fold scattering pattern in the A-phase of the helimagnetic B20 compound MnSi [1]. The six-fold scattering pattern can be seen almost independently from the crystal orientation. The skyrmion lattice is an incommensurable hexagonal lattice of topological stable knots of the spin structure. The non trivial nature of this new magnetic structure leads to the topological Hall effect, which is an extra contribution to the abnormal Hall effect in ferromagnets [2]. In simple mean field calculations in combination with thermal fluctuations, the skyrmion lattice has a ground state for small magnetic fields and just below the transition temperature of the helimagnet MnSi. In our recent SANS experiments there was no direct microscopic evidence of the skyrmion lattice since we were not able to measure higher order scattering.

In order to examine the magnetic variation on long length scales and to establish the existence of higher order scattering of the skyrmion lattice, we performed high resolution SANS experiments at MIRA and V4 at BENSC in Berlin. To avoid non isotropic effects of the demagnetization of the sample, we prepared thin MnSi samples and illuminated the thin slices only in the center. As a result, we obtained rocking scans with sharp Gaussians and an extremely narrow width, $\eta = 0.45°$, slightly larger than the resolution limit. Thus, the intrinsic magnetic correlation length of the skyrmion lattice exceeds 100 μm and is therefore more than a magnitude larger than for the helical state.

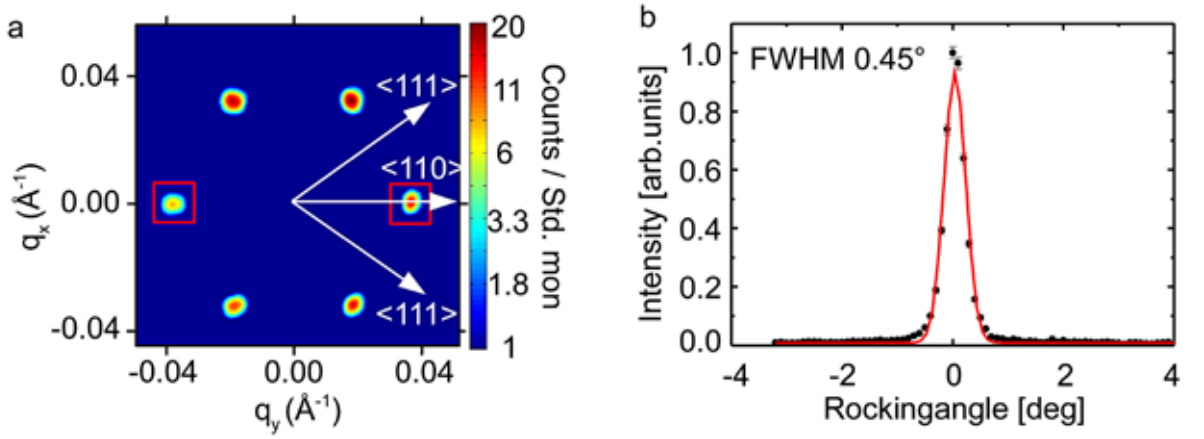

Figure 1: Typical SANS data in the A phase of MnSi: (a) Intensity pattern in thin platelet at $\mu_0 H = 200$ mT. (b) Rocking scan of the data shown in (a); note the narrow Gaussian dependence.

In order to distinguish double scattering from higher order scattering, we used the so-called Renninger scans depicted in figure 2a. The sample is thereby first rotated together with the magnetic field around the vertical axis through an angle χ until the sum of two scattering vectors $q_1 + q_2$ touches the Ewald sphere, thus satisfying the scattering condition. This is followed by the actual Renninger scan, which is a rocking scan with respect to $q_1 + q_2$ through the angle φ, while recording the intensity at $q_1 + q_2$. In this way, double scattering is "rocked out" of the scattering condition, while higher-order scattering continues to satisfy the scattering condition for all φ. The background for T was determined well above Tc for each rocking angle and subsequently subtracted. The intensity at $q_1 + q_2$, as indicated by box 1 in figure 2b, was then compared with the intensity in a box of equal size at a position slightly to the side of $q_1 + q_2$, labeled box 2. Typical variations of the intensities in box 1 and box 2 with the angle φ are shown in figure 2c for T = Tc – 0.5 K and $\mu_0 H$ = 200 mT. The intensity observed at $q_1 + q_2$ clearly displays two contributions: (i) two Gaussian peaks due to double scattering when either $q_1 + q_2$ intersects the Ewald sphere and (ii) a constant intensity arising due to true higher-order reflections (red shading). As seen in figure 3 we performed Renninger scans as a function of different magnetic fields and temperatures.

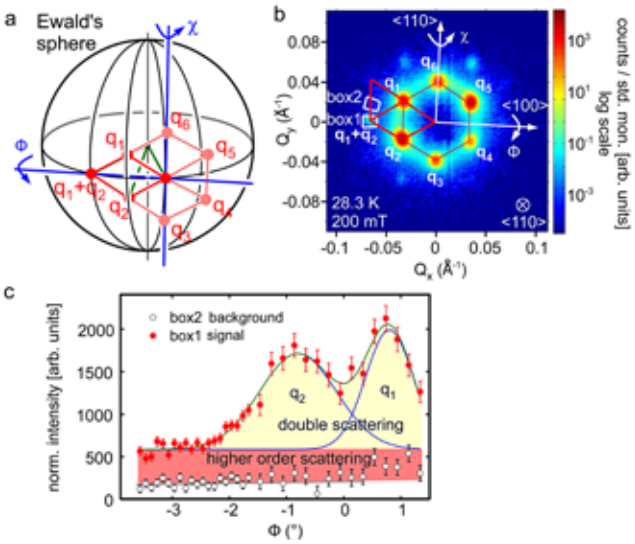

Figure 2: Operating principle and typical data of Renninger scans: (a) Ewald sphere depiction of the Renninger scans. (b) Typical scattering pattern obtained by summing over a rocking scan around φ after background substraction recorded at high T. (c) Intensity as a function of rocking angle φ in a Renninger scan. The intensity was integrated over the areas of box 1 and 2 in (b).

Main experimental results [3]: (i) A strong magnetic field dependence of the second-order intensity, which appears to vanish for a certain field inside the A phase. (ii) An increase in the second-order intensity with increasing T. (iii) A tiny weight of the higher-order peaks of the order of 10^{-3}. Simple mean field calculations which take thermal fluctuations into account qualitatively reproduce the field and temperature dependence of the second order scattering in our experimental results, and as a result we provide a microscopic evidence of the skyrmion lattice in MnSi.

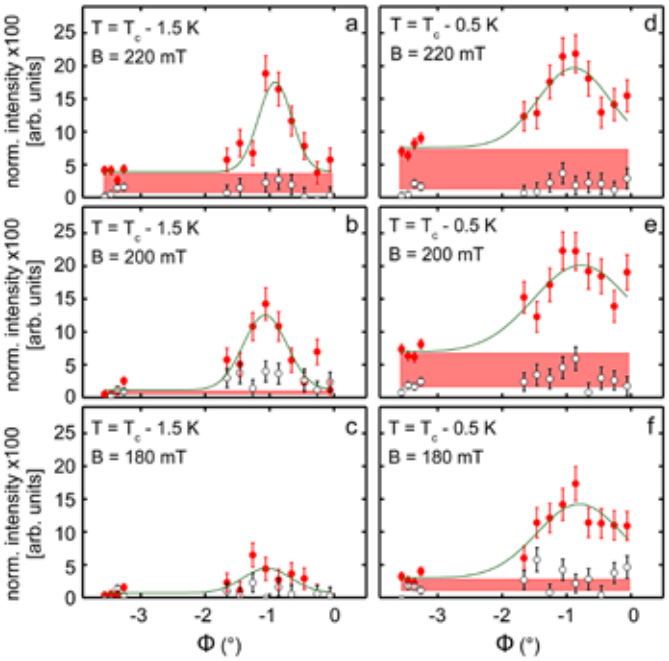

Figure 3: Typical Renninger scans at various T and B in the A phase of MnSi. (a)–(c) were recorded at T = Tc – 1.5 K and magnetic fields $\mu_0 H$ = 180, 200, and 220 mT. (d)–(f) show Renninger scans for T = Tc = 0.5 K and magnetic fields of $\mu_0 H$ = 180, 200, and 220 mT. True higher-order scattering is shaded in red and remains constant for large Φ.

[1] S. Mühlbauer et al., Science 323, 915 (2009).
[2] A. Neubauer et al., Phys. Rev. Lett., 102, 186602 (2009).
[3] T. Adams et al., Phys. Rev. Lett., 107, 217206 (2011).

Better neutron guides, improved detectors and sample environment, new software developments

P. Link[1], S. Masalovich[1], K. Zeitelhack[1], J. Peters[1], J. Krüger[1], J. Wuttke[2]

[1]Technische Universität München, Forschungs-Neutronenquelle Heinz Maier-Leibnitz (FRM II), Garching, Germany

[2]Forschungszentrum Jülich GmbH, Jülich Centre for Neutron Science at FRM II, Garching, Germany

The year 2011 was marked by the long maintenance break that had already started in October 2010 and lasted for over one year. The corporate service groups used that time to replace neutron guides, to improve or to upgrade existing equipment and detectors, or to develop new devices. All these services will serve to support the scientists in order to achieve the best neutron beams with highest flux and ideal neutron detection. In addition, sample environments for the individual experimental requirements were improved. Newly developed software facilitates the control of instruments and the diverse sample environment parameters. Furthermore, the recently formed scientifc computing group will assist scientists with complex data analysis in future.

The neutron optics group at work: Neutron guides for the FRM II

In 2011, the laboratory installations required for the production of complete neutron guides were finished. The neutron optics group is now able to build curved and straight neutron guides with supermirror (NiTi) coatings up to m = 3.5. As one of the first neutron guides fully constructed in-house, the JCNS small-angle diffractormeter KWS-3 acquired a neutron guide end element.
Moreover, neutron ray-tracing simulations using the McStas software package of a wavelength adaptive focusing beam nose element for the time-of-flight spectrometer TOFTOF were performed as part of the PhD-thesis work of Roxana Valicu. A prototype element was constructed, built in-house, and installed at TOFTOF. Verification of the expected performance using neutrons is under-way.

Figure 1: Members of the neutron optics group align a new neutron guide element in the neutron guide tunnel.

A major task of the neutron optics group is the maintenance of the existing neutron guide system that provides neutrons for the neutron guide hall west. During a well prepared maintenance session, guide elements were replaced in the neutron guide tunnel (fig. 1) for the four main guide lines NL1 (BioDiff, N-REX, MEPHISTO), NL3 (KWS-1, -2, -3), NL5 (RESEDA, TREFF, MARIA) and NL6 (MIRA, MIRA-2, DNS, SPHERES) The previously installed borofloat glass guides situated at distances from 8 - 14 m from the cold source clearly showed that neutron irradiation had caused damage. Now, boron-free float glass guides are used throughout the FRM II up to a distance of 14 m from the cold source. At the same time, the vacuum housings of these guide lines have been replaced by aluminium housings in order to avoid further activation of the steel housings previously used in the neutron guide tunnel.
Another challenge for the group was the installation of the in-pile section of the neutron guide for the future MEPHISTO instrument in the neutron guide hall east at beam tube SR4b. When the collimator of the former instrument ANTARES on this beam tube had been taken out, the neu-

tron guide elements with a m = 3.3 supermirror coating on aluminium substrate were built in and aligned.

HELIOS – polarized ^{3}He gas for neutron polarization analysis at the FRM II

The optical pumping station HELIOS supplies neutron instruments at the FRM II with polarized ^{3}He gas for neutron polarization analysis. During the shutdown period, the polarized gas was mainly used for testing new cells and for the development of a new NMR setup at POLI-HEiDi. This NMR setup allows the gas polarization to be monitored during long-lasting neutron experiments.

The HELIOS itself was equipped with two new high power lasers with better stability of the laser beam polarization. This ensures a constistently high production rate of 1 bar-liter per hour of ^{3}He gas with about 72 % gas polarization. It is planned to add the two original lasers into the optical path, in order to increase of the final gas polarization.

Following the restart of the neutron source in 2011 the cells with polarized ^{3}He gas were provided for neutron polarization analysis at the instruments POLI-HEiDi, MIRA and REFSANS. REFSANS started in 2011 using neutron polarization analysis in scattering experiments and the very first measurements were performed with ^{3}He gas filter cells prepared at HELIOS.

One of the advantages of using ^{3}He filter cells for polarization analysis is the capability of building an “ideal” analyzer with almost 100 % analyzing efficiency. Such cells filled at HELIOS have also been implemented at the instrument MIRA for a precise calibration of a new solid-state polarizing device constructed for MIRA, and a new radio-frequency spin-flipper device.

Furthermore, the new ^{3}He filter cell with glued Si single-crystal windows (fig. 2) has finally been prepared and tested. This scattering free cell fits very well with the requirements for neutron polarization analysis at neutron small-angle scattering instruments and neutron reflectometers. The cell has a diameter of 90 mm with 75 mm length

Figure 2: ^{3}He filter cell with beam windows made from single crystal silicon.

and currently features a wall relaxation time of 90 hours. It is planned to build two more of these cells in the near future.

In order to cater for the growing demand for polarized ^{3}He gas, a further transportation device with a shielded solenoid has also been built at the neutron optics group.

Improved neutron detection: New detectors for TOFTOF and SANS-1

Apart from a series of smaller detector and read out electronics upgrades, the long shutdown period in 2011 was used to complete two major detector projects. The upgrade of the time-of-flight instrument TOFTOF was brought to a successful conclusion, involving as it did an increase in the number of detector tubes from 600 to 1000 and including a partial renewal of the detector electronics installation. The new detector is now fully operational with significantly improved performance. At the same time, the new 1 x 1 m^2 detector for the new small angle scattering instrument SANS-1 was finally commissioned and is now waiting for the instrument to commence operation (fig. 3).

Better detector performance at StressSpec

In order to improve the detector performance of the diffractometer StressSpec a new high resolution (1 x 1 mm^2) Multiwire Proportional Counter is under construction based on a concept de-

veloped within the “MILAND” Joint Research Activity of the NMI3 consortium in the European Framework Programme 6 (FP6). Taking advantage of the Time-over-Threshold (ToT) information of each of the 256 x 256 individual readout channels, the systems provide 2D-position and time stamp for each detected neutron. Following successful prototype tests, the series production of the readout electronics has been started and the detector MWPC-250-HR is currently beeing assembled (fig. 4).

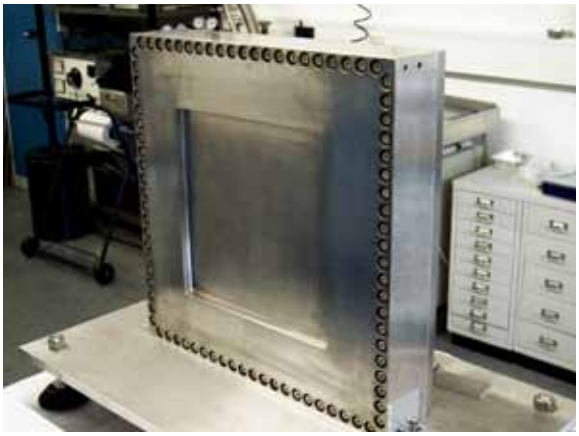

Figure 4: Pressure vessel of the new high resolution detector MWPC-250-HR for StressSpec.

Solid boron-10 converters in gaseous detectors

Driven by the dwindling supply of ^{3}He, the search for alternative technologies to ^{3}He detectors for neutron scattering applications has become more and more important. In a joint collaboration with other research groups, the FRM II is actively involved in the development of technologies using solid boron-10 converters in gaseous detectors. The deposition of uniform ~1 µm thin boron-10 layers on very large areas at reasonable cost and the detector design of multilayer arrangements using up to 30 boron-10 layers to achieve adequate efficiency presents a considerable challenge when applying this technology to neutron scattering applications. Efficiency, homogeneity and long term stability are the most important parameters of the boron coatings in view of their potential use. A small prototype device capable of handling up to six boron layers of size 10 x 10 cm^2 has been built to study the performance of boron coatings on aluminium substrates produced using different evaporation technologies (fig. 5). The results obtained can then be compared to sophisticated GEANT4 Monte-Carlo Calculations, which have already been performed in parallel with the development of the boron-10 converter.

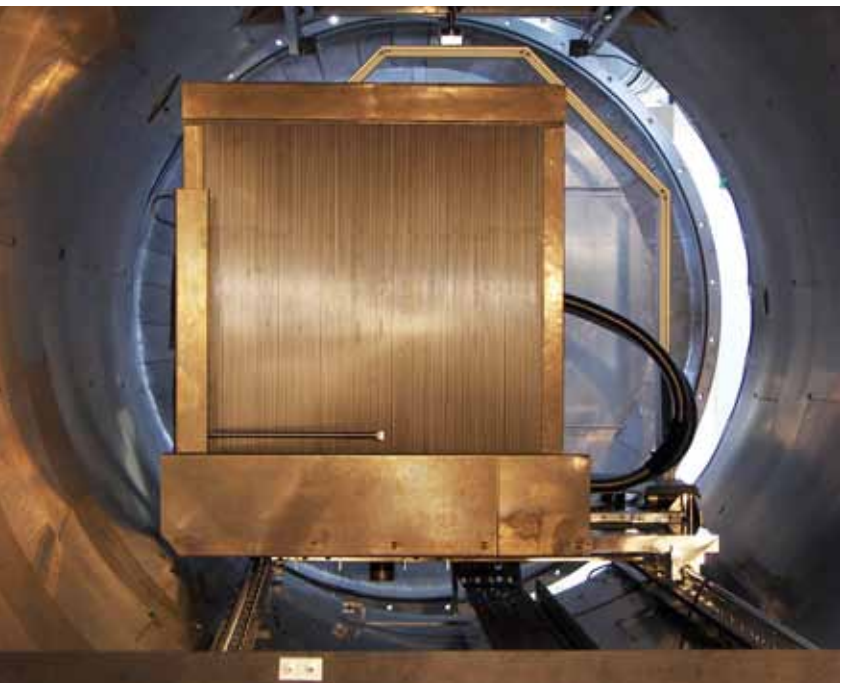

Figure 3: The new 1 x 1 m^2 detector at SANS-1.

Within a Joint Research Activity of the NMI3 collaboration in the Seventh European Framework Programme (FP7), the FRM II detector group has started to investigate the use of Graphical processing Units (GPU) in the readout chain of Gaseous Scintillation Proportional Counters (GSPC) with ANGER type readout. Modern graphic cards for PCs have considerable processing power at low cost and they promise to be an appropriate device for implementing highly parallelizable algorithms, such as the maximum likelihood method used for the position reconstruction of detected neutron events.

Improvements of sample environments

In 2011, the activities of the sample environment group have been dedicated to general maintenance work, upgrades and test runs to improve

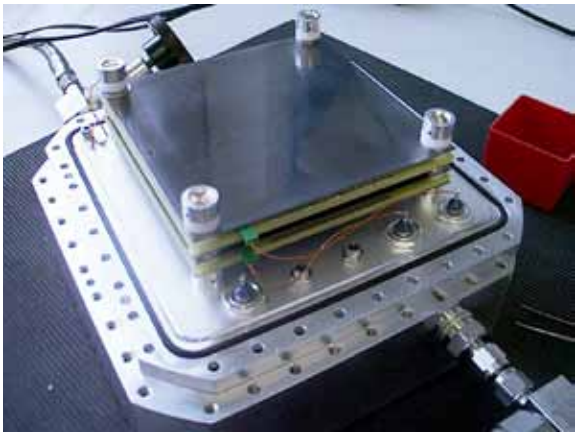

Figure 5: Small size gaseous detector to study the performance of solid boron-10 converters.

the availability and performance of sample environment equipment.
Furthermore, some new devices have been developed. Examples include high voltage sample sticks allowing for electric fields up to 15 kV, depending on the sample. Special care was taken to protect temperature sensors and controllers from harmful overvoltage.

The performance of the dry high pressure rig cryostat developed at the FRM II was improved. The setup allows for in situ pressure variation. Now, sample temperatures below 10 K are possible, operating at pressures of up to 14 GPa and a sample diameter of 6 mm. The pressure is applied by a 400 kN pressure rig acting directly through the cryostat via a thermally insulated piston in the cylinder setup.

The upgraded CCR cools samples down to 1.3 K

The design of the "FRM II 1 Kelvin Top Loading Closed Cycle Refrigerator (CCR)" was upgraded (fig. 6). A Joule-Thomson expansion and an evaporation stage provides a temperature extension down to 1.3 K with the sample in exchange gas. The objective was to optimise the integration and performance of the 3rd cold stage.

A heat switch, for instance, reduces the cooling down time significantly to 3 h and the design takes into account a limited required space. Thus, the standard tail dimensions are kept and the operation of a CCR in combination with the 7.5 T room temperature bore magnet is possible. A similar setup was used to design a bottom loading cryostat providing adequate sample space to cool huge cold masses such as pressure cells. In this case, a ^{3}He stage allows for temperatures from 400 mK to room temperature.

Development of a universal control box for CCR

Remote control of experiments is an essential tool for the effective use of beam time. The integration of sample environment equipment is an important aspects of this, even more so since sample change time and time for equipment setup are going to be the limiting factors in terms of experimental turnover.

The dry top loading cryostats (CCR) developed at the FRM II offers users, in principle, full remote controlled operation. Different components such as start/stop of the cold head, control of exchange-gas pressure and temperature control are accessible via the TACO/TANGO control software.

Figure 6: Closed cycle refrigerator (CCR) (right) with the newly developed universal control box (top left).

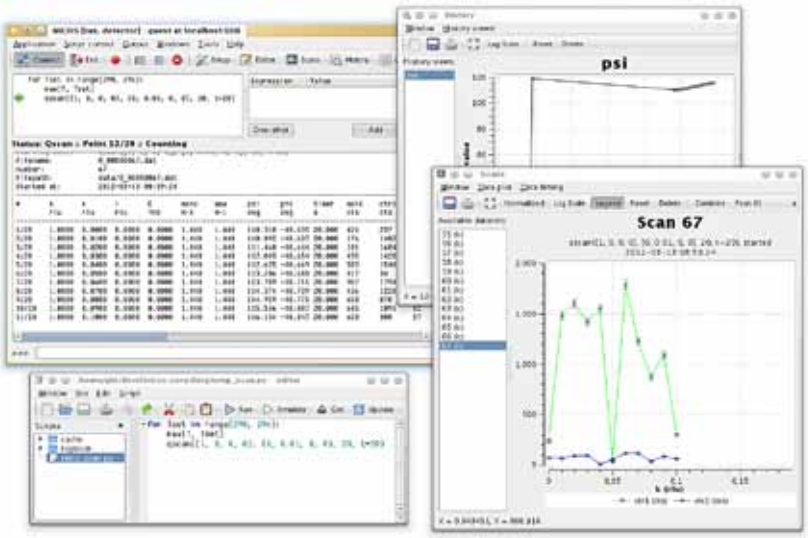

Figure 7: Use of the NICOS software will become the standard instrument control software at the FRM II.

A further step towards facilitating the communication setup is a new universal control box developed recently (fig. 6). The corresponding software was provided by the IT Services group of the FRM II (see next paragraph). As far as the refrigerator of type CCR is concerned, this involves integrating CCR-control, temperature and optional peripheral devices control such as rotation tables etc. in one “black box”.

Instrument control and software developments: TACO-Box-Development

In close collaboration with the Sample Environment group, a common software interface for mobile sample environments such as Closed Cycle Refrigerator (CCR) and Halogen Lamp Oven was developed. The software interface will be installed on small computers that will be provided with the sample environment.

By plugging in the network cable, the system is accessible via a web interface as well as via a TACO interface. The web interface displays the current state of the sample environment in respect of temperature, pressure of the gas and of the insulation vacuum. In addition, it allows one to control the parameters of the temperature controllers, switch on the compressor, to open/close valves, switch on the halogen lamps in the case of ovens, and to set up the controllers. In this way, the sample environment group is easily able to manage the temperature control devices (LakeShore temperature controllers LS336 with double control loops).

The web interface further allows to install sensor curves and setting the right curves for the sensors used. It ensures a correct setup for the user experiments of the delivered sample environment that can be easily integrated into the instrument control software via the TACO interface.

Instrument control software

In 2011, the instrument control software took a major step towards becoming more unified. Beside the development of TACO/Tango device drivers for various hardware systems, the NICOS system was completely rewritten and a lot of new features such as data cache (including a history function), status monitor, and others were added.
The main goal of the development was to make NICOS ready for use at many instruments. At the moment, the new NICOS is running on PANDA, MIRA, PUMA, RESI, TOFTOF, and it will be installed in 2012 on REFSANS, PGAA, and ANTARES. The modularity of NICOS allows specific configurations for each instrument optimally adjusted to its requirements. NICOS will become the standard instrument control software at the FRM II (fig. 7).

Digital User Office software

In a joint collaboration of several research facilities, the core of libraries to setup a Digital User Office has been developed. Besides the usual tasks of a Digital User Office the software allows for an easy configuration of additional tasks specific for the facility.
The main new task in 2011 was the integration of different types of database engines like MySQL and ORACLE in addition to the existing integration of the PostgreSQL database engine into the Digital User Office. In addition the core libraries have been rewritten.

Organisational software

Additionally, the software group at the FRM II develops and maintains some systems in support of device operation and safety, mainly for the regular periodic checks of the neutron source, collecting and managing the radio protection data, archiving documents concerned with the facility, and managing the access of persons to the FRM II.

Scientific computing group for data analysis

A joint group for scientific computing was created within the framework of the HZG-TUM cooperation. The group will support instrument scientists and user communities by developing dedicated open-source software for the data analysis of neutron scattering experiments.

Growing demand for professional computing

Since computing pervades the practice of science, there is a growing need for scientific computing to become more professional. Scientists employing neutron scattering would benefit from this as the power of the experimental method is often underexploited because of insufficient software support. Two trends drive the quest for ever better software. One is the progress in data quantity and quality.

Two-dimensional detectors have caused a huge increase in data production rates, resulting in an urgent need for automated data reduction and fitting procedures. Qualitative improvements, such as an enhanced signal-to-noise ratio in inelastic spectroscopy, expose the limitations of established procedures and models, and prompt the need for more realistic models and more refined analysis procedures.
The other trend is the evolution of neutron scattering from a highly specialized field of physics into a service tool for application domain specialists: to remain attractive, neutron centres must strive for the same ease of use as it is customary, for instance, in NMR.

Therefore, the Jülich and TUM partners at the FRM II decided to create a joint group for scientific computing. The group is located at the JCNS outstation at the FRM II in Garching.

The initial staff of five experts consists of: Joachim Wuttke, group leader, former instrument responsible of SPHERES; Christian Felder, software engineer; Genady Pospelov, whose background is in experimental particle physics; and Walter Van Herck, software engineer and theoretical physicist (fig. 8).

Upcoming projects

The first projects of the group are determined by a program of the Helmholtz Association, the High Data Rate Processing and Analysis Initative (HDRI). Jülich is formally involved in two of three workpackages. Workpackage 1 is concerned with data archives and access; it responds to the political demands for open access to all data obtained through public funding. In workpackage 3, an exemplary data analysis package will be developed.
The chosen application is Grazing Incidence Small Angle Scattering (GISAS), which is of interest for synchrotron as well as for neutron centres.

Figure 8: Members of the newly formed Scientific Computing group (from left to right): Walter Van Herck, Joachim Wuttke, Christian Felder, and Gennadi Pospelov.

In situ tensile rig experiment on high temperature CoRe alloy at the instrument STRESS-SPEC.

Scientific Highlights

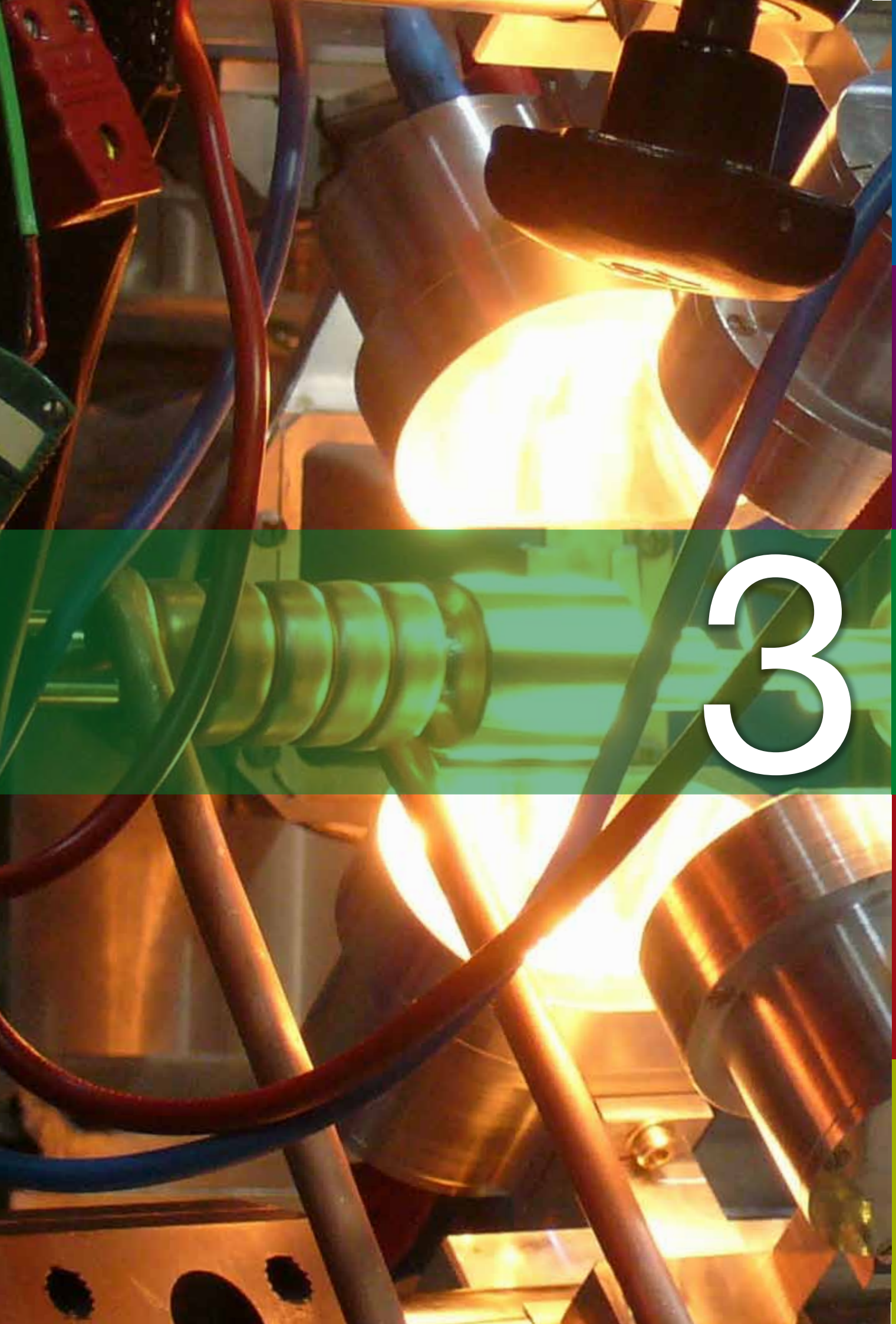

3

Phase behaviour and structure of zwitanionic mixtures of perfluorocarboxylates and TDMAO

K. Bressel[1], S. Prévost[1,2], M.-S. Appavou[3], M. Gradzielski[1]

[1]Technische Universität Berlin, Institut für Chemie, Stranski Laboratorium für Physikalische und Theoretische Chemie, Berlin, Germany

[2]Helmholtz-Zentrum Berlin für Materialien und Energie, Berlin, Germany

[3]Forschungszentrum Jülich GmbH, Jülich Centre for Neutron Science at FRM II, Garching, Germany

Phase behaviour and structure of zwitanionic surfactant mixtures based on the zwitterionic tetradecyldimethylamine oxide (TDMAO) and anionic $C_nF_{(2n+1)}CO_2Li$ have been investigated for various chain lengths of the perfluoro surfactant. Head group interactions as well as the volume of the hydrophobic chains play a central role in the ability to form vesicles. The ability of mixed systems to form well-defined unilamellar vesicles can be controlled by the length of the chain of the perfluorinated surfactant and depends on the charge conditions, to be tuned by pH-variation [1].

Observation of the formation of vesicles

Mixtures of cationic or zwitterionic and anionic surfactants (catanionics or zwitanionics) have been studied previously. Catanionic mixtures are well-known to form vesicles spontaneously but have a tendency for precipitation [2-4]. In contrast, zwitanionic mixtures possess fewer synergistic interactions between the surfactant pairs, and are therefore less prone to precipitation, but may also form vesicles. For the case of the mixing of a zwitterionic hydrocarbon surfactant with an anionic perfluoro surfactant in particular one may observe the formation of vesicles.

SANS-measurements at KWS-2

SANS-experiments on the system TDMAO-$C_7F_{15}CO_2Li$ were performed at the instrument KWS-2 of JCNS (operating at FRM II) and compared to measurements on the systems TDMAO-$C_5F_{11}CO_2Li$ and TDMAO-$C_6F_{13}CO_2Li$ performed on the instrument V4 of the Helmholtz-Zentrum Berlin (HZB). The samples consisted of aqueous solutions of TDMAO and a lithium perfluoro alkanoate ($C_5F_{11}CO_2Li$, $C_6F_{13}CO_2Li$, or $C_7F_{15}CO_2Li$) with a total surfactant concentration of 50 mM. All measurements were made at 25° C.

Rod-like micelles

Figure 1 depicts the SANS curves for various surfactant mixtures as a function of the mixing ratio. From its analysis a detailed structural picture of the contained surfactant aggregates was derived. In the micellar region with high TDMAO content rod-like micelles are found. The length of the rod-like micelles increases with decreasing TDMAO content, reaching a maximum around equimolar mixing for TDMAO-$C_5F_{11}CO_2Li$. For $C_7F_{15}CO_2Li$ the typical oscillations of vesicle shells are seen in the equimolar range.

Figure 2 compares the phase behaviour of the three systems. Over the whole mixing range of α(TDMAO) = 0-1 micellar regions (L_1), vesicle

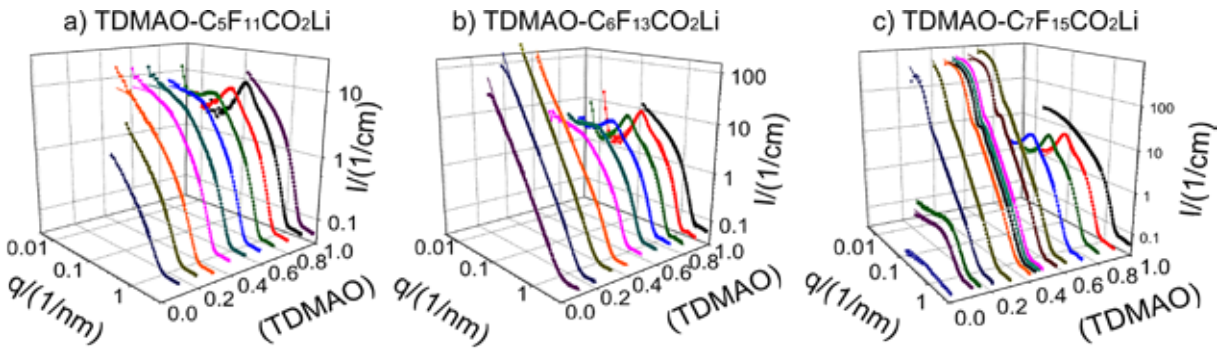

Figure 1: Small angle neutron scattering (SANS) measurements of mixtures of TDMAO with various perfluoro surfactants (50 mM, 25 °C): a) $C_5F_{11}CO_2Li$, b) $C_6F_{13}CO_2Li$, c) $C_7F_{15}CO_2Li$. For TDMAO-$C_5F_{11}CO_2Li$ and TDMAO-$C_6F_{13}CO_2Li$ at α(TDMAO) = 0, no measurement is shown since here one is below the cmc.

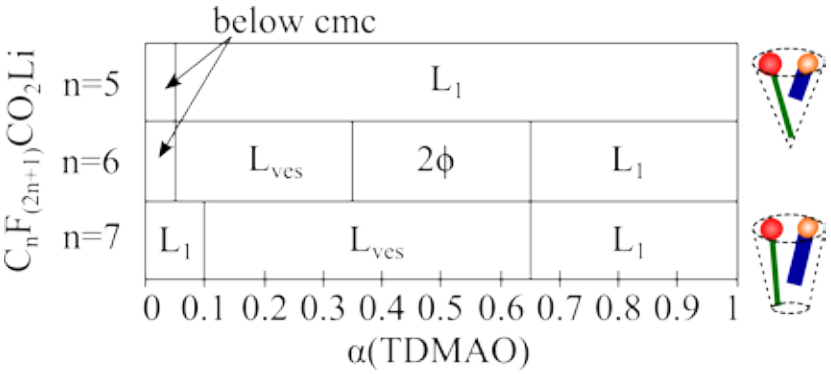

Figure 2: Comparison of the phase behaviours of the systems TDMAO/$C_nF_{2n+1}CO_2Li$ with n = 5, 6, 7, c_{tot}=50 mM, 25 °C.

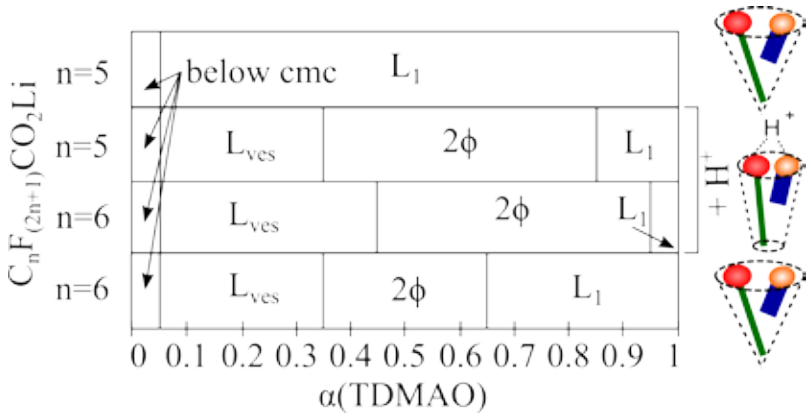

Figure 3: Comparison of the phase behaviours of the systems TDMAO/HCl/$C_nF_{2n+1}CO_2Li$ with n = 5, 6, influence of addition of HCl, c_{tot} = 50 mM, 25°C.

regions (L_{ves}) and two phase areas (2φ) with a phase separation into a vesicular precipitate and a micellar phase is observed. The ability to form vesicles strongly depends on the chain length of the perfluoro surfactant. In the system TDMAO-$C_5F_{11}CO_2Li$ only micellar aggregates are found and SANS measurements show that these micelles are rod-like micelles whose length increases with increasing perfluoro surfactant content.
Figure 3 depicts the change of the phase behaviour with the pH. With decreasing pH the TDMAO head group becomes protonated which leads to an increased head group interaction and thereby to a reduced head group size. This has the same effect as an increase in the perfluoro surfactant chain length.

Two influencing factors: chain length and pH

The phase behaviour in systems TDMAO/TDMAOH$^+$Cl$^-$-$C_nF_{2n+1}CO_2Li$ is mainly influenced by the chain length of the perfluoro surfactant (fig. 2) and the degree of protonation of the TDMAO head group (fig. 3). Protonation of the TDMAO head group leads to an increased attractive interaction between the alkanoate head group and the TDMAOH$^+$ head group, which leads to a shift from the zwitanionic system to a more catanionic system with stronger head group interactions and to a decreased head group area. Increasing the surfactant chain volume as well as decreasing the surfactant head group area increases the packing parameter, which facilitates a transition from micelles to vesicles.

In summary, we found that zwitanionic surfactant mixtures composed of TDMAO and lithium perfluoro alkanoates are structurally versatile systems in which vesicle formation can be tuned either by changing the chain length of the perfluoro alkanoate or by changing the pH. This means that spontaneous formation of vesicles can be achieved by an appropriate choice of composition and vesicle formation can easily be tuned by pH.

[1] K. Bressel et al., Soft Matter, 7 (23), 11232 (2011).
[2] K.L. Herrington et al., J. Phys. Chem., 97, 13792 (1993).
[3] E.W. Kaler et al., J. Phys. Chem., 96, 6698 (1992).
[4] E.F. Marques et al., J. Phys. Chem. B, 102, 6746 (1998).

Structure and dynamics of polymer rings: breakdown of the Rouse diffusion

A. Brás[1], S. Gooßen[1], R. Pasquino[2], Th. Koukoulas[3], G. Tsolou[3], O. Holderer[4], A. Radulescu[4], V. G. Mavrantzas[3], J. Allgaier[1], W. Pyckhout-Hintzen[1], A. Wischnewski[1], D. Vlassopoulos[2], D. Richter[1]

[1]Forschungszentrum Jülich GmbH, Jülich Centre for Neutron Science, Jülich, Germany

[2]Institute of Electronic Structure and Laser and University of Crete, Department of Materials Science and Technology, Heraklion, Greece

[3]University of Patras, Department of Chemical Engineering, Patras, Greece

[4]Forschungszentrum Jülich GmbH, Jülich Centre for Neutron Science at FRM II, Garching, Germany

We present a neutron scattering study on both the structure and dynamics of a ring polymer. In the first case, using small angle neutron scattering (SANS at KWS 2) the ring structure proved to be significantly more compact when compared to the linear chain with the same molecular weight, in accordance with both theory and simulations. The dynamical behaviour of both systems, which has been explored for the first time using neutron spin echo spectroscopy (NSE at JNSE), shows a surprisingly fast centre of mass diffusion as compared to the linear polymer. These results agree qualitatively with the presented atomistic MD simulations. The fast diffusion turned out to be an explicit violation of the Rouse prediction.

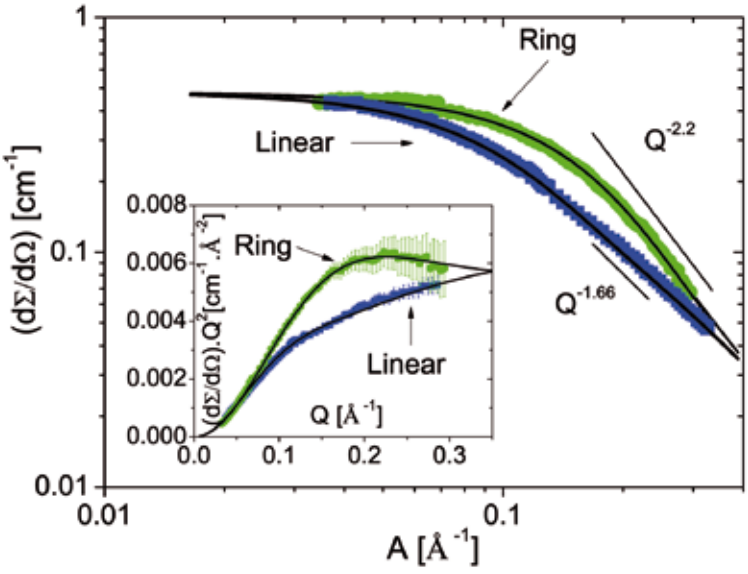

Figure 1: SANS data on the linear and ring melts. The inset shows the respective Kratky plot for both systems.

Ring polymers are of strong academic interest

The dynamics of cyclic polymers having no chain ends is one of the most attractive subjects of polymer dynamics. On the one hand polymer rings play an important role in industry and daily life (e.g. DNA, viscosity modifier) and on the other rings are of strong academic interest. Whereas the relaxation of linear polymers is to a large extent determined by chain ends, these are completely absent in ring polymers. It is well accepted that the dynamics of linear polymers can be described by the reptation theory as proposed by de Gennes [1] and Doi and Edwards [2]. On the basis of an extended tube concept, there a polymer chain starts to release from its confinement from both chain ends (contour length fluctuations, CLF) thereby accelerating the reptation process. Here, considering the local Rouse structure, cyclic polymers are expected to show significantly different dynamical behaviour.

Thus the intriguing question of how cyclic polymers relax without contribution from chain ends has not yet been solved. Here, neutron scattering is of utmost importance in understanding the underlying mechanisms from both a structural and dynamical point of view.

Experiments at KWS 2 and JNSE

Experiments were performed at the SANS diffractometer KWS 2 and the spin-echo spectrometer JNSE at the FRM II, Garching. At KWS 2 the scattering vector range 0.01 Å^{-1} < Q < 0.4 Å^{-1} was accessed, whereas the Q-range in JNSE was varied in discrete steps between 0.05 Å^{-1} < Q < 0.2 Å^{-1}.

Breakdown of the Rouse prediction

For the first time, the dynamics of short PEO ring polymers has been studied using NSE spec-

troscopy and the coherent single chain dynamic structure factor of cyclic polymers measured. The molecular weight studied is M_n = 1770 g/ mol.

A combination with SANS and rheological measurements, which were also performed, showed that the ratio of the squared radius of gyration (R_G) of the linear chains to the ring as well as the ratio of their viscosities (η) differ by a factor of 2, as expected within the Rouse theory.

Figure 1 shows the SANS scattering profiles obtained, i.e., the intensity I(Q) versus scattering vector Q of the linear and the ring polymer. The respective form factors were well described by means of a multivariate Gaussian distribution approach, as shown by the full lines in figure 1. This allowed one to extract their respective R_G (ring polymer, R_G = 9.9 Å, and linear polymer, R_G = 15 Å). A quantitative analysis in the $QR_G > 1$ region shows a distinct Q dependence for the different systems. Whereas the polymers effectively agree with Gaussian chain statistics for short chains, the Kratky plot, shown in the inset of figure 1, illustrates the different architecture of the rings unequivocally. The shallow peak developing in the plot is indicative of the increased compact structure.

Figure 2 presents the coherent dynamic structure factor of the pure ring and linear polymer at the lowest Q value (Q = 0.05 Å^{-1}). Within the

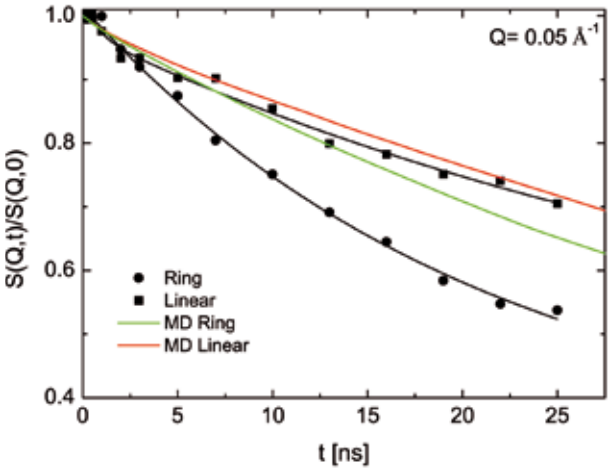

Figure 2: Comparison of the normalized dynamic structure factor S(Q, t) vs. t for the ring and linear melts at the lowest Q value (Q = 0.05 Å^{-1}) from MD simulations with NSE data.

Figure 3: Instrument scientists at KWS 2 at the FRM II.

Rouse model [2] the diffusion of both ring and linear chains should be identical since the centre of mass diffusion in this model does not depend on the architecture. However, a comparison between the centre of mass diffusion of the linear chains, with the ring determined by fitting the Rouse model to the lowest Q value, as shown by the solid lines in figure 2, revealed that the latter is faster by a factor of ~2. This result of the first NSE experiments on pure rings was also qualitatively corroborated by molecular dynamics simulations [3]. The surprisingly fast centre of mass diffusion turned out to be an explicit violation of the Rouse prediction.

Summarizing the neutron scattering results we have found

- the ring polymers are more compact in the melt than the linear PEO,
- R_G^2 and the viscosity of the ring are both 2-fold smaller than the linear precursor as expected and
- in contrast to the Rouse expectation the diffusion of the Rouse ring is twice as fast compared to the linear reference with identical molecular weight.

[1] P.G. de Gennes, J. Chem. Phys., 55 (2), 572 (1971).
[2] M. Doi and S.F. Edwards, The Theory of Polymer Dynamics, Oxford University Press, Oxford, UK (1986).
[3] A.R. Bras et al., Soft Matter, 7,11169 (2011).

The α relaxation dynamics of a pure semicrystalline polymer studied using spin echo

A. Sanz[1, 2], W. Haeussler[3], A. Nogales[1], T. A. Ezquerra[1]

[1]Consejo Superior de Investigaciones Científicas, Instituto de Estructura de la Materia, IEM-CSIC, Madrid, Spain

[2]Consejo Superior de Investigaciones Científicas, Instituto de Química Física Rocasonalo, IQFR-CSIC, Madrid, Spain

[3]Technische Universität München, Forschungs-Neutronenquelle Heinz Maier-Leibnitz (FRM II), Garching, Germany

By performing NSE measurements at the RESEDA instrument above the T_g of deuterated semicrystalline poly(ethylene terephthalate), we were able to gain access to the dynamics governed by the α relaxation, revealing that the intermolecular cooperativity is rather similar in both amorphous and semicrystalline polymers, and suggesting that the dynamics of semicrystalline polymers occurs in an homogeneous scenario, similar to that valid in the description of the dynamics of totally amorphous polymers.

Mismatch between relaxation and fragility

The amorphous phase in a semicrystalline polymer can be considered as self-confined (schematic view in fig. 1) within the restricted environment imposed by the lamellar crystals. In response to an external perturbation, the amorphous phase of semicrystalline polymers decays in a non-exponential way, normally described by the KWW function

$$\Phi(t) \propto e^{-\left(t/\tau_{KWW}\right)^{\beta}}$$

where τ_{KWW} is the characteristic relaxation time.

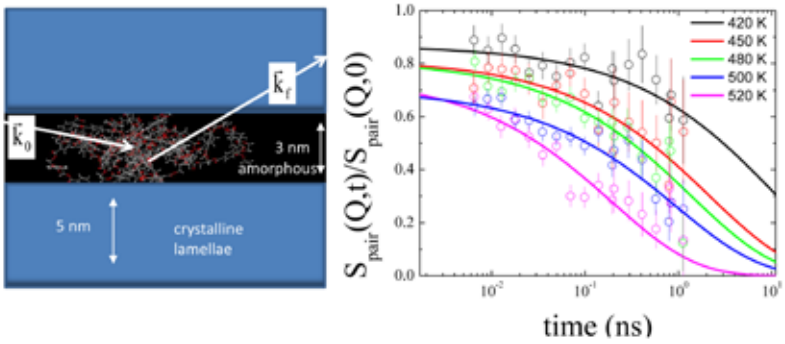

Figure 1: Schematic drawing showing the lamellar two-phase structure of semicrystalline d-PET. Values of the thickness of the amorphous and crystalline layers have been obtained by x-ray scattering measurements. On the right: time evolution of the dynamic structure factor of semicrystalline d-PET at Q = 13.8 nm^{-1} at different temperatures above T_g. Continuous lines correspond to the fits of the KWW function to the experimental data.

Values of β ≈ 0.5 are typical for amorphous polymers. In contrast, much broader segmental dynamics is observed for semicrystalline polymers which may render values as low as β ≈ 0.2. For glass forming systems, a certain correlation has been found between β and the fragility index m as $m = m_0 - s\beta$ [1] with $m_0 = 250 \pm 30$ and $s = 320$. This relation suggests that the more fragile the system is, the more non-exponential the relaxation functions will be. In semicrystalline polymers, the empirical relation described above seems to fail when the α process is explored using a macroscopic relaxation technique such as dielectric spectroscopy. Whether this apparent mismatch between broadening of the relaxation and dynamical fragility is caused by inhomogeneous broadening due to the intrinsic structural heterogeneity of a semicrystalline polymer or to a modification of the dynamical scenario provoked by the confinement of the amorphous phase by the lamellar crystals is a question that can be solved through the use of neutron spin echo (NSE).

NSE offers a direct molecular assessment of dynamical processes both in space and in time, through a direct observation of the dynamic structure factor $S_{pair}(Q,t)$. By carrying out NSE measurements above the T_g of the polymer in the Q-range close to the first static structure factor maxima, we were able to gain access to the dynamics governed by the α relaxation.

Experiments at RESEDA

NSE experiments on semicrystalline (crystallinity of 32.5 %) poly(ethylene terephthalate, PET) (fully deuterated) were performed at the RESEDA instrument (FRM II, neutron guide NL5a) at a fixed Q value of 13.8 nm^{-1}. Different temperatures were investigated in the Fourier intervals of

0.001 ns ≤ t ≤ 5 ns, restricted to 2 ns at maximum, with an incident wave length of λ = 0.545 nm. The calorimetric glass transition temperature T_g of the semicrystalline d-PET was 345 K.

Decay times decrease with temperature

Figure 1 shows the dynamic structure factor of semicrystalline d-PET at Q = 13.8 nm^{-1} and different temperatures above T_g. At first glance the experimental data of normalized S_{pair} (Q,t) exhibit a stretched time evolution, with characteristic decay times becoming faster the higher the temperature. The time dependence of the NSE dynamic structure factor can be written as:

$$\frac{S_{pair(Q,t)}}{S_{pair(Q,0)}} \propto exp\left[-\left(\frac{t}{\tau_{NSE(Q)}}\right)^{\beta}\right]$$

where $\tau_{NSE\ (Q)}$ represents the Q-dependent characteristic time of the relaxation as measured by NSE. These values of $\tau_{NSE(Q)}$ fit reasonably well into the Vogel-Fulcher Theory [2] line corresponding to the dielectric data also obtained for semicrystalline d-PET, indicating that both techniques explore the same segmental relaxation. However, the data analysis presented here reveals that while the dielectric response of the semicrystalline PET associated with α relaxation would require a very broad KWW function with β ≈ 0.2, the corresponding decay function measured by NSE provided a value of β ≈ 0.5. Curiously, the values of β_{NSE} for the semicrystalline sample are closer to the dielectric ones of the amorphous polymer. Moreover, if we consider the values of β obtained from NSE and we replot the data for the semicrystalline d-PET shown in the inset of figure 2, then the value returns to within the limits of what it is expected by the relation between m and β. All these results point toward the existence of a homogeneous dynamics in the case of a semicrystalline polymer since the value of β_{NSE} is close to that observed for the amorphous polymer and both are within the expectations for homogeneous dynamics in amorphous polymers. Consequently, we propose that the dynamic scenario for the α relaxation of a semicrystalline polymer is that of the homogeneous case.

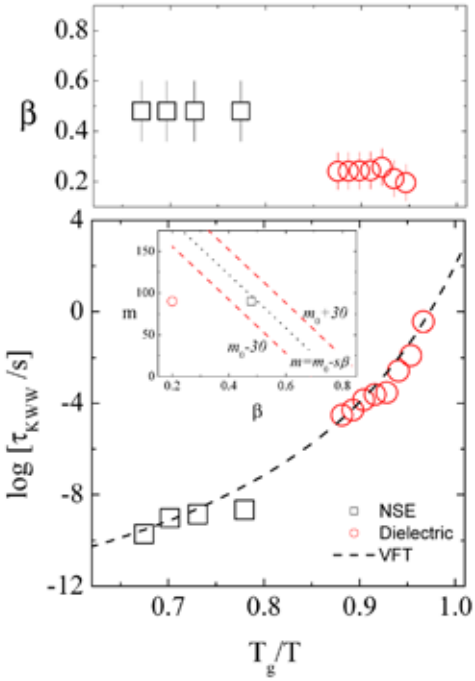

Figure 2: Fragility plot for the values of β (top) and of τ_{KWW} (bottom) obtained from the fitting of KWW function to the dielectric (circles) and NSE (squares) data for semicrystalline deuterated PET. The inset shows a graphical representation of m against β with boundaries in m_0.

Homogenous dynamics

The combination of dielectric and neutron spin echo measurements performed in a model deuterated polymer has shown that the dynamics of semicrystalline polymers occurs in a homogeneous scenario similar to that valid for describing the dynamics of amorphous polymers. Thus, the intermolecular cooperativity is expected to be rather similar in both amorphous and semicrystalline polymers [2]. The slowing down of the characteristic segmental relaxation in a semicrystalline polymer as compared to that of an amorphous one seems to be caused by a retardation of the intramolecular mobility provoked by the anchoring of the polymer chains of the amorphous phase bounded to the crystalline one.

[1] R. Bohmer et al., J. Chem. Phys. 99 (5), 4201 (1993).
[2] A. Sanz et al., Macromolecules, 44 (20), 8124 (2011).

The influence of cholesterol on the pico- to nanosecond dynamics of phospholipid molecules

S. Busch[1,2,3] and T. Unruh[1,2,4]

[1]Technische Universität München, Physik Department E13, Garching, Germany

[2]Technische Universität München, Forschungs-Neutronenquelle Heinz Maier-Leibnitz (FRM II), Garching, Germany

[3]University of Oxford, Department of Biochemistry, Laboratory of Molecular Biophysics, Oxford, United Kingdom

[4]Friedrich-Alexander-Universität Erlangen-Nürnberg, Lehrstuhl für Kristallographie und Strukturphysik, Erlangen, Germany

The dynamics of the phospholipid dimyristoylphosphatidylcholine (DMPC) was studied with time-of-flight neutron spectroscopy at the instrument TOFTOF at the FRM II. It was found that the molecules move on a pico- to nanosecond time scale in transient clusters, performing flow-like motions. It is proposed that these collective motions should be understood as a general feature of dense systems known as dynamical heterogeneities. Additionally, it could be shown that cholesterol already decreases the dynamics of the phospholipid molecules after one nanosecond by almost as much as on a macroscopic time scale.

Phospholipids are one of the main components of cell membranes. The cell can influence the mobility of its membrane by varying the concentration of cholesterol. We aimed to study the motions of the phospholipid molecules on a pico- to nanosecond time scale during which the molecules cover distances of about the molecular size, i.e. to see the first steps of the long-range motion. In earlier studies, the view of collective, flow-like motions of the molecules could be corroborated [1,2]. As a subsequent step, we wanted to determine (a) why the molecules move in this fashion and (b) how the addition of cholesterol influences the motions.

Experiments at TOFTOF

The phospholipid DMPC was obtained as dry powder. Pure phospholipid samples were hydrated with D_2O via the vapour phase until a clear liquid formed. Further liquid D_2O was added to ensure full hydration of this liquid crystalline phase during the whole experiment. Cholesterol, also obtained as dry powder, was added to the corresponding samples before hydration.

The samples were studied at several temperatures (described here: 20 °C and 40 °C) in the bio furnace available at the time-of-flight spectrometer TOFTOF at the FRM II. By varying the energy resolution of the incoming neutron beam, it was possible to adjust the observation time to 60 and 900 picoseconds. The mobility of the molecules was determined by measuring the excess half width at half maximum of the quasielastic line compared to the elastic line measured on a vanadium standard.

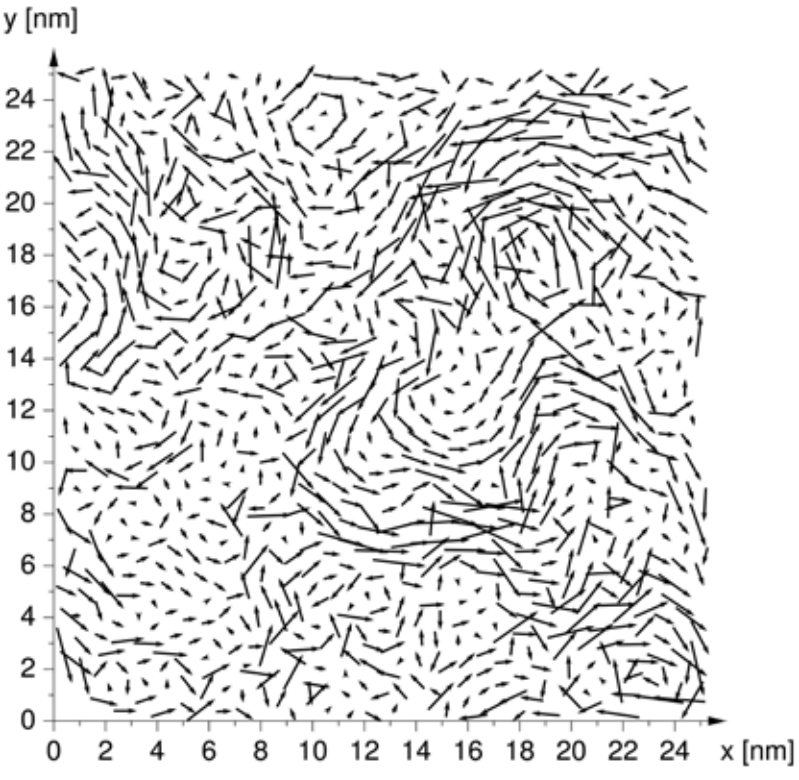

Figure 1: The displacement field of particles in a simulation of a two-dimensional Lennard-Jones liquid. It can be seen that fast particles are spatially separated from slow particles and that the displacements of the fast particles show flow-like patterns. Drawn after [3].

Mobility of DMPC and the effect of cholesterol

In order to understand why the observed flow-like motions of the phospholipid molecules in the plane of the membrane form, a very simple model system was studied: a molecular dynamics (MD) simulation of a two-dimensional Lennard-Jones liquid [3]. Marking the displacements of the molecules over a given time with an arrow (shown in figure 1) resulted in a very similar picture to the one that had been observed in previous MD simulations of phospholipid bilayers [4]. Therefore, it can be concluded that the flow-like motions of small transient clusters of molecules are a general feature of densely packed systems and do not depend on the particular interactions between the molecules. In fact, many glass-forming systems show very similar features, referred to as “dynamical heterogeneities”, because regions of fast molecules are clustered and spatially separated from regions of slow molecules. In those systems, an increase in temperature results in a decrease in the correlation time and length of these clusters. Indeed, the motion of the phospholipid molecules can also be better described by simple diffusion at high temperatures [5].

It is well known that cholesterol decreases the dynamics of the phospholipid molecules. In the study presented here [3], it was possible to follow the increasing influence over time. While an increase in the cholesterol concentration did not show a very pronounced effect on the mobility of the phospholipid molecules on a time scale of 60 picoseconds, shown in figure 2, the mobility on a 900 picosecond time scale was strongly decreased – by about the same amount as measured at macroscopic times and distances [6]. The decelerating effect of cholesterol is therefore already almost completely unfolded within one nanosecond.

The concept of dynamical heterogeneities

The normal way of describing the motions of phospholipid molecules within the membrane, the free volume theory, was a very successful loan from glass physics. It is now time to take a new loan and use the many concepts that have been developed for dense systems since then,

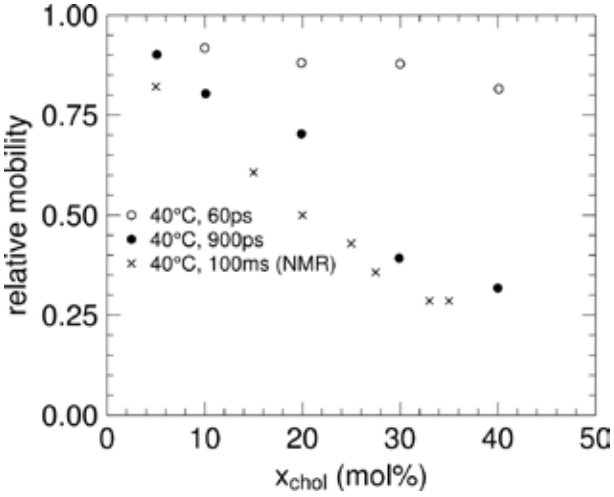

Figure 2: The decrease of the relative mobility of DMPC as a function of the cholesterol concentration at different observation times. The two measurements at 60 and 900 picoseconds are neutron measurements, the NMR measurement was taken from the literature [6]. Drawn after [3].

for example the idea of dynamical heterogeneities. We have not only shown that the free volume theory fails on a nanoscopic scale to describe the motions of phospholipid molecules, but also mentioned that the collective flow-like motions are present in all densely packed systems and can therefore also be expected to be present in the phospholipid systems.

Concerning the influence of cholesterol, these studies give a time scale during which the molecules manifest their influence, namely below about one nanosecond. We propose that the decelerating effect on this short time scale could be due to a reduced correlation length of the flow-like motions.

[1] S. Busch et al., J. Am. Chem. Soc., 132, 3232 (2010).
[2] S. Busch and T. Unruh, J. Phys.: Condens. Matter, 23, 254205 (2011).
[3] S. Busch and T. Unruh, Biochim. Biophys. Acta, Biomembr., 1808 (1), 199 (2011).
[4] E. Falck et al., J. Am. Chem. Soc.,130 (1), 44 (2008).
[5] S. Busch et al., Soft Matter, 8 (13), 3576 (2012).
[6] A. Filippov et al., Biophys. J., 84 (5) 3079 (2003).

Water migration into a casein micelle film: a neutron radiography study

E. Metwalli[1], H.E. Hermes[2], E. Calzada[3], S.U. Egelhaaf[2], P. Müller-Buschbaum[1]

[1]Technische Universität München, Physik Department E13, Garching, Germany

[2]Heinrich-Heine-Universität, Lehrstuhl für Physik der weichen Materie, Düsseldorf, Germany

[3]Technische Universität München, Forschungs-Neutronenquelle Heinz Maier-Leibnitz (FRM II), Garching, Germany

This study demonstrates the use of neutron radiography as a viable method for determining the diffusion profile of water in biological samples. Profiles of water concentration were successfully probed in films of the milk protein casein which form a micelle structure. By imaging the water concentration in a casein micelle film, we observed two diffusion processes: (a) fast diffusion with a decaying diffusion constant, resulting from water exchange with the hydration water bound to the casein proteins, and (b) slow and constant diffusion due to Fickian water transport into the voids and holes between the casein micelles and their aggregates in the porous protein film. From this study on the penetration of water into casein-based materials we were able to gain insights into the impact of water on the durability and mechanical stability and, hence, the performance of adhesive films based on casein.

Casein is a protein found in the milk of all mammals, forming hydrated micelles of about 100 – 300 nm in diameter. Casein micelles in milk are unique bio-colloids of calcium, phosphate, and casein proteins. The latter play an important biological role in stabilizing the colloidal form of calcium phosphate in milk and are also used in non-food related applications such as adhesives (labelling glass bottles), binders, and protective coatings. Recently, we have investigated the structure of casein micelles in thin films [1-4]. In the present investigation, we study water diffusion in thick sub-millimeter films of casein micelles. From this study on water penetration into casein-based materials we aim to provide information that improves our understanding of the durability as well as the mechanical stability and, hence, the performance of adhesive films based on casein micelles.

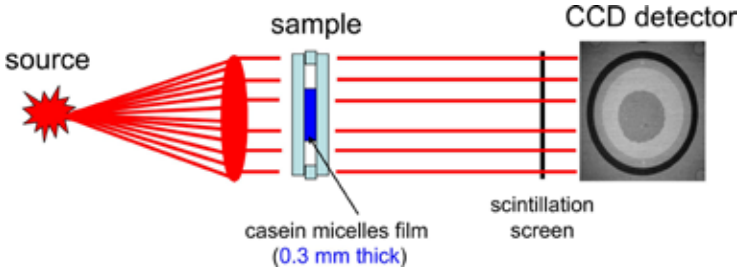

Figure 1: Schematic view of the neutron radiography setup.

Experimental setup at ANTARES

A gel resembling casein micelles in D_2O (50 wt%) was prepared and cast on an open-cell aluminium plate. The sample was then squashed using a second aluminium plate to create a disk-like 0.3 mm thick film. The neutron radiography (NR) experiment was performed at the neutron imaging facility ANTARES at the Forschungs-Neutronenquelle Heinz Maier-Leibnitz (FRM II). The neutron beam transmits through the sample cell and strikes a scintillator plate that emits a cascade of photons from every spot that absorbs a neutron. The light produced from the scintillator plate is deflected by a mirror to a CCD camera set to 2048 x 2048 pixels (fig. 1). Prior to the NR experiment, the casein film in the cell was heat-treated at 50 °C for 30 min to create a “dry” film. Water (H_2O) was injected into the cell containing the casein film via an inlet to replace the air around the film by water (fig. 2). Neutron radiography images were collected periodically at a time frame of 30 s.

Water migration into the casein micelle

The “dry” casein micelle film as seen with neutron radiography is shown in figure 2a. Figure 2 shows the initial water injection into the cell at different time periods, illustrating the high time resolution of the neutron radiography experiment. The “zero” time of the water migration ex-

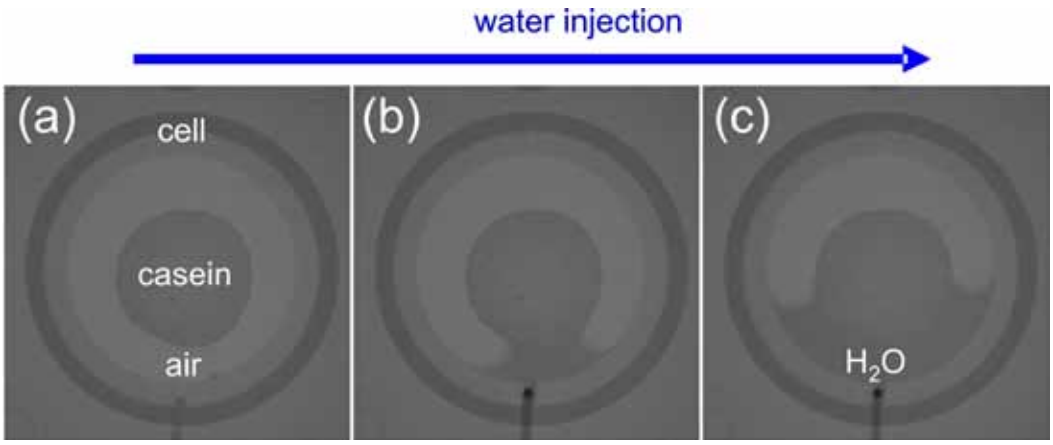

Figure 2: Set of neutron transmission images showing the initial water injection into an aluminium cell where a 0.3 mm thick dry casein micelle film is located in the centre of the cell. The time zero is set to a time at which the film is completely surrounded by water instead of air.

periment is the time when the water completely surrounded the casein film. We determined the water penetration into the film by radial averaging the two-dimensional neutron radiography images. Figure 3 shows the normalized (to pure H_2O transmission) intensity profiles at different elapsed times. The corresponding spatial water distribution θ(x,t) at different times is calculated and an example is plotted in the inset of figure 3. The water distribution profiles (inset in fig. 3) are fitted using the solution to a one-dimensional diffusion equation. The diffusion constant D as a function of time t (with t = 0 being the time of complete water-film contact) is obtained as an output of the fitting procedure.

"Self-diffusion" processes dominate

From the diffusion coefficient constants determined as a function time, a non-steady diffusion behaviour is observed. It substantially decreases with time in the initial stages of the process (up to t = 630 s). At longer times (t > 630 s), a constant D value (1.31 x 10^{-3} mm^2/s) is observed within an error of 14 %. The higher initial D value is attributed to the strong tendency of the casein micelles to form hydrogen bonds with water. It is assumed that the observed water migration into the casein micelle film is dominated by a "self-diffusion" process where "free" water molecules easily bind or fast exchange with the monolayer hydration water shell surrounding the casein micelles. Interestingly, a constant diffusion regime was reached after a time of about 630 s, consistent with our previous observations of the hydration kinetics of casein micelle thin films in saturated water vapour atmosphere [4]. In this latter study we employed grazing incidence small-angle neutron scattering (GISANS) to probe the hydration water content in thin casein film as a function of time after a saturated water vapour environment was brought into contact with the film [4].

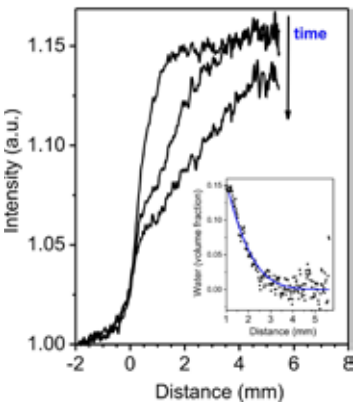

Figure 3: Normalized intensity profiles (radially averaged) of the neutron radiographs from the casein micelle film in contact with water. The inset in the graph shows the spatial distribution of the water content that is fitted (solid line) using a one-dimensional diffusion equation.

Neutron radiography as ideal method to study water diffusion processes in biological samples

Casein sub-millimeter "dry" film is put into contact with water and the water migration is systematically probed using neutron radiography. The study successfully demonstrates the use of neutron radiography for the determination of the water diffusion profile in soft and biomaterial films. Profiles of the water concentration were imaged in casein films at a high time resolution of thirty seconds. From the water concentration in the casein micellar film, we observed two diffusion processes: (a) fast diffusion due to high water exchange with the protein hydration water, and (b) slow and constant diffusion due to Fickian water transport into the porous film.

[1] P. Müller-Buschbaum et al., Biophys. J., 93, 960 (2007).
[2] P. Müller-Buschbaum et al., Biomacromolecules 7 (6), 1773 (2006).
[3] R. Gebhardt et al, Int. Dairy J., 20 (3), 203 (2010).
[4] E. Metwalli et al., Langmuir, 25, 4124 (2009).

Acceleration of complex fluids near a wall and its significance for enhanced oil recovery

H. Frielinghaus[1], M. Kerscher[2], O. Holderer[1], M. Monkenbusch[2], D. Richter[1,2]

[1] Forschungszentrum Jülich GmbH, Jülich Centre of Neutron Science at FRM II, Garching, Germany

[2] Forschungszentrum Jülich GmbH, Institute for Complex Systems 1, Jülich, Germany

In the enhanced oil recovery, complex fluids are pumped to the oil field for various reasons. The fluid drives the oil towards the bore hole in the secondary/tertiary oil recovery. High viscosity inhibits the `fingering´, i.e. bypassing of the fluid. The fracturing fluid deposits the pressure energy inside the sandstone close to the bore hole due to the high viscosity. The cracks generated serve higher recovery rates after the application. Microemulsions often form when the aqueous surfactant system comes into contact with the oil.

Grazing incidence method

The surface dynamics near microemulsions have been characterized using grazing incidence neutron spin echo spectroscopy (GINSES) [1] at the instrument J-NSE (fig. 1). This method allowed us to obtain detailed information on the depth of the dynamics for the first time. We found a relaxation three times faster adjacent to the surface as compared to the bulk. The wall-reflected hydrodynamic field explains the faster dynamics. The static structure of this system has been characterized in a previous study [2]. While a bicontinuous structure is formed in the bulk, the structure near the surface is lamellar.

Figure 1: Grazing incidence neutron spin echo spectroscopy (GINSES) at the Jülich Neutron Spin Echo Spectrometer (J-NSE) at the FRM II.

The relaxation times were obtained from a single stretched exponential function as a function of the scattering depth. The information on depth is obtained from the evanescent (tunneling) wave at the surface and was varied using different incident angles below the angle of total reflection and/or different contrasts between the solid (hydrophilic modified silicon) and the overall microemulsion (fig. 2). The exponentially decaying intensity thus highlights different thickness near surface layers of the microemulsion. The relaxation times (fig. 3) show a considerable acceleration near the solid, and the transition is described by the intensity ratio of the bulk and near surface scattering obtained from the static experiments.

Theoretical understanding

The intermediate scattering function was also modeled using individual fluctuating membranes of a finite patch size. The Zilman-Granek theory holds for the bulk structure and includes the hydrodynamic self-interactions of the membrane patch. Undulations with wave vectors between the reciprocal patch size and molecule size are considered. The near surface lamellar membranes have an almost infinite patch size, and thus the deviating dispersion relation from isolated patches to near surface patches becomes clear. This dispersion relation of confined mem-

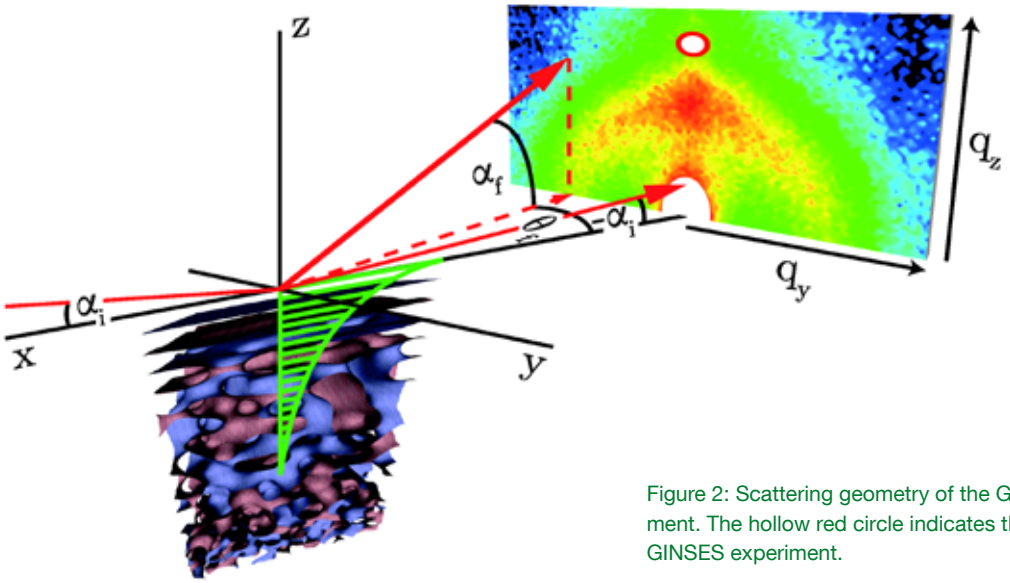

Figure 2: Scattering geometry of the GINSES experiment. The hollow red circle indicates the Q-vector of the GINSES experiment.

branes is faster compared to the bulk due to the reflected hydrodynamic waves (the feedback is faster). This overall picture describes the three-fold acceleration of the near surface membranes.

Applications and impact

The overall concept of the dispersion relation can also be connected to viscosities. At small wave vectors the lamellar ordering leads to the well known lubrication effect. This means that the lamellae can slide away easily along the surface. A macroscopic slip length might be defined by this arrangement. This result is also highly interesting for complex fluids in porous environments such as enhanced oil recovery. The order near the surface leads to better pumping conditions with lower dispersive energy losses at the sandstone walls. This is highly desirable, especially in oil production after the application of the cracking fluid.

The results might also be fundamental to an understanding of the capture process of leukocytes (or immune cells in general) to vessel walls. The capture process must have a surface bound state of the leukocyte before receptors strengthen the surface binding. The confinement of the cell membrane might explain this initial bound state, which has not been described elsewhere.

Meaning of GINSES in the future

As to the future, this new method promises to be highly interesting for lipid bilayers with embedded membrane proteins. From these studies the protein effect on the membrane undulations can be studied. Quicker results are expected from measurements of polymer additives in microemulsions and/or other model complex fluids. First measurements lead us to believe that the polymer additive is driven towards the solid surface by the translational entropy which finally causes a slowing down of the near surface dynamics. Hence, the known thickening of polymers is amplified at surfaces.

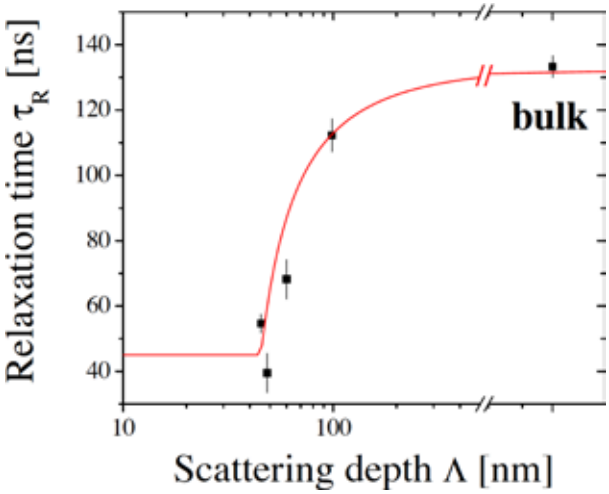

Figure 3: Relaxation times obtained from a single stretched exponential fit as a function of the scattering depth. The solid line arises from intensity ratios of static measurements.

[1] H. Frielinghaus et al., Phys. Rev. E, accepted (2012).

[2] M. Kerscher et al., Phys. Rev. E, 83 (3), 030401(R) (2011).

Trace elements in metalloenzymes determined by neutron activation analysis (NAA)

X. Li[1], A. Pelzmann[2], L. Canella[1], F. Mickoleit[2], O. Meyer[2], H. Gerstenberg[1]

[1]Technische Universität München, Forschungs-Neutronenquelle Heinz Maier-Leibnitz (FRM II), Garching, Germany

[2]Universität Bayreuth, Lehrstuhl für Mikrobiologie, Bayreuth, Germany

Carbon monoxide (CO) dehydrogenases are metalloenzymes which operate in several kinds of aerobic and anaerobic bacteria. They oxidize CO to CO_2 and thereby continuously remove CO from the atmosphere. CO oxidation in the catalytic site of CO dehydrogenases is accomplished at unique metal clusters, which combine S atoms with the metals Mo and Cu or Zn and Fe. The understanding of proper metal clusters holds considerable interest for fundamental science and is also essential to preserving the global biological sink of atmospheric CO. The metal composition of such enzymes was determined by using neutron activation analysis (NAA).

The maturation of metal centres in enzymes is a life-sustaining activity. Numerous metal centres in proteins catalyze important functions. The spectrum of metalloproteins is extensive and some maturation processes are still unknown. *Oligotropha carboxidovorans* OM5 [1] is a bacterium which inhabits water and soil. These microorganisms are the most important biotic sink of atmospheric CO since the gas serves as an excellent chemolithoautotrophic growth substrate. CO dehydrogenase is the key enzyme of the Gram-negative chemolithoautotrophic eubacterium OM5, which catalyzes this process under aerobic conditions. The active site of the butterfly shaped enzyme is represented by a novel bimetallic [$CuSMoO_2$]-cluster harboured in the largest one of its three subunits, namely CoxL [2].

We are interested in studying the functions of three maturation proteins: CoxD, CoxE and CoxF. Their genes were genetically disrupted leading to *Oligotropha carboxidovorans* OM5 mutants, which synthesized apo-CO dehydrogenases with differences in their active site structures [3]. Since all three apo-enzymes are unable to catalyze the oxidation of CO, one can assume that one or more metal components might be missing in the inactive enzymes. Neutron Activation Analysis (NAA) is a sensitive multi-element analytical technique used for quantitative analysis of trace and rare elements. It should yield more information about the concentration of the metal elements Cu, Mo, Fe and Zn in the apo-enzymes.

Irradiation with thermal neutrons

Four samples were prepared in PE tubes. Each of them contains 2 ml protein solution with a protein concentration of 9.5 mg/ml. The sample WT (wild type) was the CO-dehydrogenase from the *Oligotropha* strain without any mutation. The samples E and F contained the inactive apo-CO dehydrogenases synthesized by the *Oligotropha* mutants for the genes coding for CoxE and CoxF. The fourth sample P was the matrix substance (buffer solution) without protein. All samples were irradiated on the rabbit system RPA2 with a thermal neutron flux density of about $1.5 \cdot 10^{13}$/ cm^2 s and measured without any chemical treatment directly on a highly sensitive Ge-detector with a relative efficiency of 40 % after cooling.

After counting the first two samples WT and E irradiated for 30 min, the irradiation time was extended to 1 h for the other two samples (F and P), in order to increase the count rates of the long lived isotopes ^{59}Fe and ^{65}Zn. The fluctuation of the thermal neutron flux at the irradiation position was determined using a flux monitor of gold standard.

Samples were measured after a cooling of about 7 ~ 10 days, in order to reduce the influence of

	WT			E			F			P (matrix)		
Au	40	6	ppt	<29		ppt	36	5	ppt	50	3	ppt
Br	138	10	ppb	4.1	0.3	ppm	36	4	ppb	31	2	ppb
Ca	14	4	ppm	36	6	ppm	29	3	ppm	26	2	ppm
Co	25	2	ppb	23	2	ppb	3.9	0.3	ppb	<0.4		ppb
Cr	77	6	ppb	49	4	ppb	14	1	ppb	9	1	ppb
Cu	<6.2		ppm	<3		ppm	< 4.2		ppm	<4		ppm
Fe	14.7	1.0	ppm	14.7	1.0	ppm	14.5	1.0	ppm	<186		ppb
Mo	5.73	0.37	ppm	4.86	0.32	ppm	6.07	0.40	ppm	8.6	2.4	ppb
Na	456	32	ppm	427	30	ppm	406	28	ppm	278	13	ppm
Sb	1.6	0.5	ppb	1.2	0.3	ppb	1.1	0.2	ppb	0.9	0.2	ppb
Se	735	74	ppb	251	18	ppb	677	49	ppb	<5.2		ppb
Zn	398	30	ppb	389	29	ppb	508	38	ppb	105	7	ppb

Table 1: Concentration of trace elements in the protein samples, referring to a sample weight of 2 ml (~2 g). Counting error, flux fluctuation and uncertainty of efficiency calibration are included.

the high activity of ^{24}Na. More than 20 isotopes were able to be determined by using the k_0-method [5] in each sample. Mo was determined by counting the dominant ɣ-line of its daughter isotope ^{99m}Tc at 140.5 keV. Due to the very low count rate of about 10^{-2} cps, ^{59}Fe and ^{65}Zn were counted at the closest position on the detector for 2 days, in order to reduce the counting error down to 10 %.

Table 1 shows the concentration of 12 trace elements. All three samples (WT, E, F) contained almost the same concentration of Fe and Mo within the margin of measurement errors. The Zn concentration in the sample F was 40 % higher than in other samples.

A contamination of Zn and Mo (but only at ppb-level) could be detected in the matrix P. One of the main uncertainties in the whole analysis was the ɣ-counting efficiency, due to the sample geometry not beeing perfect. The counting of the annihilation ɣ-line of positrons emitted from ^{64}Cu at 511 keV was seriously compromised by the pair production effect of the high energy ɣ-rays of ^{24}Na activated by neutrons in the biological samples. The very short-lived isotope of copper ^{66}Cu could hardly be detected by a routine analysis procedure. In this work, the determination limit of Cu in each sample was calculated based on the counting of its very weak ɣ-line at 1345 keV.

An attempt was made to analyze the samples using the prompt-gamma activation analysis PGAA as a complementary method. However, due to the low concentrations of the metal elements and the neutron scattering on the PE-sample containers, the results of both methods could not be compared.

The NAA delivered very precise results for trace elements in the protein samples with very low concentrations, even down to the ppt-level (parts per trillion e.g. 1 part in 10^{12}).

The concentrations of Mo and Fe in the inactive CO-dehydrogenase samples E and F correspond very well to the values of the active wild type CO-dehydrogenase, which can be confirmed by the earlier analysis [2]. That means that no deficit of Mo and Fe content was found in either mutant. Fe does not take part in the maturation directly, but plays an important role in the transportation of electrons in the enzyme. Cu could not be determined quantitatively. However, a new method to minimize the interference of ^{24}Na is being investigated.

Previous studies have indicated that CO dehydrogenase also harbours large amounts of zinc ions [4]. The Zn concentration determined in this work will give therefore room for a speculative model of active sites with Zn.

[1] O. Meyer, Genus VII. Oligotropha: Bergey´s Manual of Systematic Bacteriology, 2, Ed. G.M. Garrity, Springer, New York, 468 (2005).

[2] H. Dobbek et al., Proc. Natl. Acad. Sci. USA, 99, 15971 (2002).

[3] A. Pelzmann et al., J. Biol. Chem., 284, 9578 (2009).

[4] O. Meyer, J. Biol. Chem., 257, 1333 (1982).

[5] F. De Corte et al., J. Radioanal. Nucl. Chem., 13, 145 (1987).

Inner morphology of TiO_2-ceramic composites for photovoltaic applications probed with GISANS

M. Rawolle[1], K. Sarkar[1], M. A. Niedermeier[1], P. Lellig[2], J. S. Gutmann[2,3], P. Busch[4], P. Müller-Buschbaum[1]

[1]Technische Universität München, Physik-Department, Lehrstuhl für Funktionelle Materialien, Garching, Germany

[2]Max Planck Institute for Polymer Research, Mainz, Germany

[3]Universität Duisburg-Essen, Deutsches Textilforschungsinstitut, Krefeld, Germany

[4]Forschungszentrum Jülich GmbH, Jülich Centre for Neutron Science at FRM II, Garching, Germany

The inner morphology of novel materials for applications in organic photovoltaics is probed in the case of a titania-ceramic composite with GISANS measurements at the small angle scattering instruments KWS 1 and KWS 2. The scattering contrast is increased by infiltration of the porous network with D_2O, allowing one to probe the inner morphology of porous titania embedded in a SiOC-type ceramic, prepared by different calcination settings. The pore sizes and arrangements in the nanostructured materials are determined, helping to find an optimum morphology for photovoltaic applications.

Titania is a widely studied material with great application potential to tackle the energy challenges of the future due to its photoelectronic properties, combined with cheap and easy production [1]. Surrounded by a silicon oxy carbide (SiOC) type ceramic, titania can act as an electron conductor embedded in an insulating blocking layer for solid-state dye-sensitized solar cells (ssDSSCs) or hybrid solar cells [2]. For these applications, the inner morphology of the composite film is of great importance: A conducting charge percolation path consisting of crystalline titania has to be created from the top of the active layer to the electrode. At the same time, direct contact between the hole conductor and the electrode has to be circumvented with a blocking layer, which is why the titania is embedded in a ceramic.

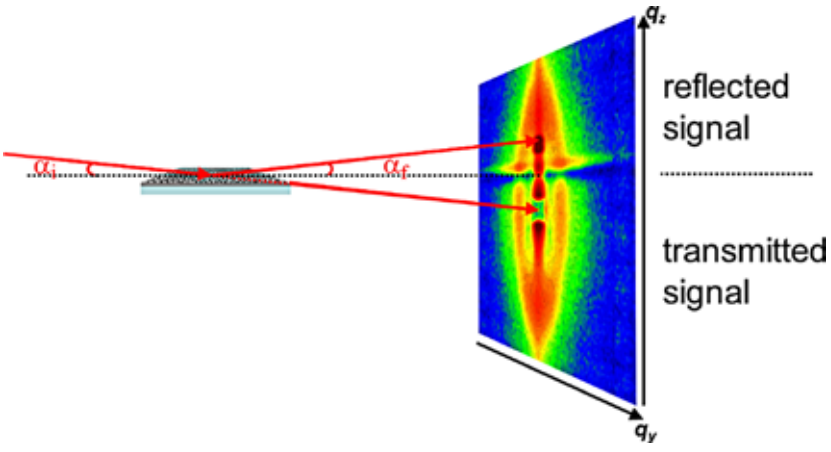

Figure 1: GISANS setup as used at the KWS 2 instrument. The dashed line indicates the sample horizon, the red arrows the neutron beam. The lower final beam points at the beamstop shielding the direct beam. The upper final beam points at the specular reflected peak at which incident angle α_i and exit angle α_f are equal.

Preparation of the titania nanostructures

The titania nanostructures are prepared by a combination of sol-gel synthesis with a structure templating by block copolymer micro-phase separation. In the present investigation, the novel PDMS-containing block copolymer poly(dimethyl siloxane)-block-methyl methacrylate(poly ethylene oxide) (PDMS-MA(PEO)) is used as a structure directing agent. This amphiphilic diblock copolymer is dissolved in a good-poor solvent pair, containing hydrochloric acid (HCl) as a poor solvent for the PDMS block, to induce micro-phase separation. By adding the titania precursor, titanium tetra isopropoxide (TTIP), the sol-gel process is started, and the resulting titania coordinates to the PEO block. The sol-gel process is further improved by the combination with micro-fluidics [3]. The fast reaction kinetics in the sol-gel process are controlled by mixing the block copolymer solution with the selective solvent HCl and the titania precursor in a micro-fluidic channel. The titania polymer nanocomposite solution is transferred to a substrate via spin-coating. The PDMS block of the diblock copolymer is transformed to a SiOC-type ceramic via calcination in an inert gas environment, while the amorphous titania embedded in the ceramic crystallizes. Different temperatures, namely 400, 600 and 1000 °C, are used.

Probing the inner film morphology

Surface structures can be probed using scanning techniques such as SEM or AFM. However, not only the surface structure but also the inner

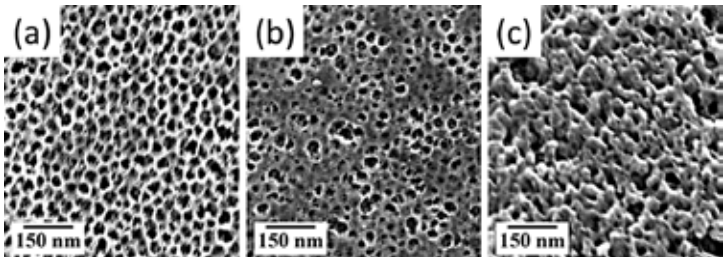

Figure 2: SEM images of titania-ceramic composites as prepared by calcination at 400 °C (a), at 600 °C (b) and at 1100 °C (c).

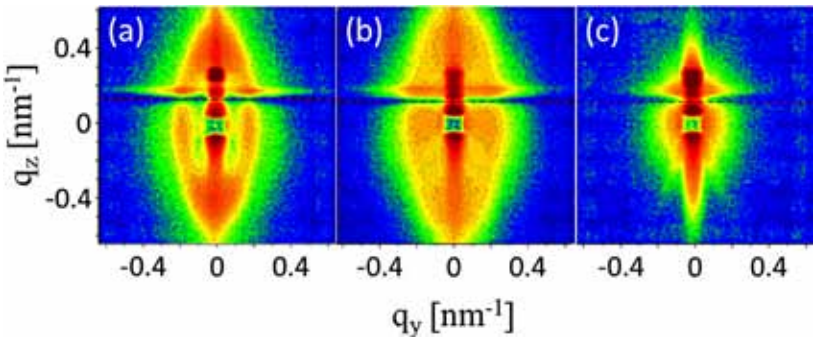

Figure 3: 2d GISANS images as measured at KWS 2 for calcination of the titania-ceramic composites at 400 °C (a), at 600 °C (b) and at 1100 °C (c).

film morphology is of importance. To probe the inner morphologies of the titania-ceramic nanocomposite films, grazing incidence small angle neutron scattering (GISANS) experiments are performed at the beamlines KWS 1 and KWS 2 of JCNS at the FRM II in Garching [4]. Figure 1 shows a sketch of the GISANS setup. A fixed incident angle of 0.54°, a wavelength of 0.48 nm and a sample-to-detector distance of 6.7 m have been used at KWS 2. To probe the titania morphology with higher efficiency, the scattering contrast is enhanced. For enhancement, the measurements were performed in a chamber filled with D_2O vapour at a temperature of 50 °C with a measurement time of only 3 h.

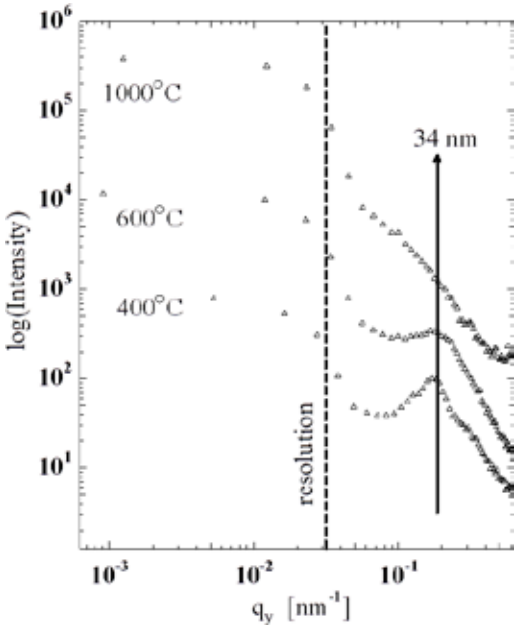

Figure 4: The horizontal cuts show the intensity profiles at a constant q_z corresponding to the material's critical angle, shifted along the intensity axis for illustrative purposes.

Promising structures for organic photovoltaics

SEM measurements (fig. 2) show that the surface morphology is affected by the calcination protocol. From the GISANS data (fig. 3), it is obvious that the mesoporous structure changes with calcination temperature, not only on the surface but in the whole volume of the film. The same trend is observed for the surface structures and for the inner morphology: For calcination at increased temperatures the structures appear less defined. Information on lateral structures is gained from horizontal cuts (in q_y-direction) at a constant q_z-value corresponding to the critical angle of the material (fig. 4). For the lowest calcination temperature, a well pronounced structure peak with higher orders corresponding to a hexagonally ordered system of pores with a distance of about 34 nm is observed. For a calcination temperature of 600 °C, the higher orders in the intensity profile and therefore the hexagonal order are lost. At an even higher temperature of 1000 °C, not only is the mean distance lost, but the structures collapse.

GISANS measurements reveal the principle of structural changes of titania-ceramic composites with increasing calcination temperature. For calcination at 400 °C, a hexagonally ordered mesoporous structure with a pore size of 34 nm is obtained. This structure appears most promising for an application in organic photovoltaics.

[1] X. Chen et al., Chem. Rev., 107, 2891 (2007).

[2] P. Lellig et al., Phys. Chem. Chem. Phys., 14 (5), 1607 (2012).

[3] M. Rawolle et al., Small, 7 (7), 884 (2011).

[4] P. Busch et al., J. Appl. Crystallogr., 44, 370 (2011).

Stability of phases at high temperatures in CoRe based alloys

R. Gilles[1], D. Mukherji[2], P. Strunz[3], M. Hofmann[1], M. Hoelzel[1], J. Roesler[2]

[1]Technische Universität München, Forschungs-Neutronenquelle Heinz Maier-Leibnitz (FRM II), Garching, Germany

[2]Technische Universität Braunschweig, Institut für Werkstoffe, Braunschweig, Germany

[3]Academy of Science, Nuclear Physics Institute, Řež near Prague, Czech Republic

In the development of new high-temperature alloys for gas turbine applications, a CoRe based alloy strengthened by $Cr_{23}C_6$ type carbide and Cr_2Re_3 type σ phase precipitations is under consideration. High-temperature cycling experiments show how the heating/cooling and the hcp ↔ fcc phase transformation of the Co-matrix influence the stability of these phases. Neutron diffraction experiments using a high-temperature vacuum furnace show that $Cr_{23}C_6$ carbides are almost completely dissolved above 1250 °C, while the σ phase is still present at 1300 °C.

The Co-Re based alloys are a new class of high temperature alloys with a relatively high melting point, which were introduced by the Technische Universität Braunschweig, Germany in 2007 [1] to supplement Ni-based superalloys in future gas turbines for application at and above 1200 °C ("Beyond Ni-Base Superalloys", DFG Forschergruppe 727). Co-based alloys are already used in gas turbines and have achieved sustained success. Their disadvantage is the limited strength and the low service temperature of around 1000 °C. In order to increase application temperatures, the melting point of Co-based alloys has to be enhanced. This is achieved by the addition of Re (which has the third highest melting point in the periodic table T_M = 3182 °C) to the Co-alloy. In this way, an increase in the melting range of the alloy of approximately 200 °C – in comparison with Ni-based superalloys – is obtained.

The microstructure of Co-Re alloy is complex and has a ε Co (hcp) matrix at room temperature (RT). The CoRe-1 (Co-17Re-23Cr-2.6C) alloy has additional phases, in particular $Cr_{23}C_6$ type carbides and a Cr_2Re_3 type σ phase. Furthermore, development of the CoRe alloy has shown that a small addition of boron (which is known to segregate to the grain boundaries) is needed in order to strengthen the weak grain boundaries in polycrystalline alloys, and to mitigate environmental embrittlement. Therefore, an alloy with the same composition as CoRe-1 but, with a further addition of 500 wt. ppm boron (CoRe-1B), was also studied.

Measurements at SPODI and STRESS-SPEC

Cylindrical samples of around 6 mm diameter and 30 mm length were cut for neutron diffraction measurements.

With a high temperature furnace in situ, heating/cooling in 5 °C steps (reached in 5 seconds) was effected to carry out measurements during a 10 minute hold at a given temperature. Measurements were performed at STRESS-SPEC (λ = 0.16225 nm) using an area detector having sufficient angular region to include all strong scattering Bragg reflections present [1]. Additional measurements at RT were done at SPODI (λ=0.15482 nm). At STRESS-SPEC, we employed the same temperature scheme for the first and the second thermal cycles of CoRe-1.

Figure 1: Sample change at the high-temperature furnace performed by Ralph Gilles, Pavel Strunz and Debashis Mukherji (from the left).

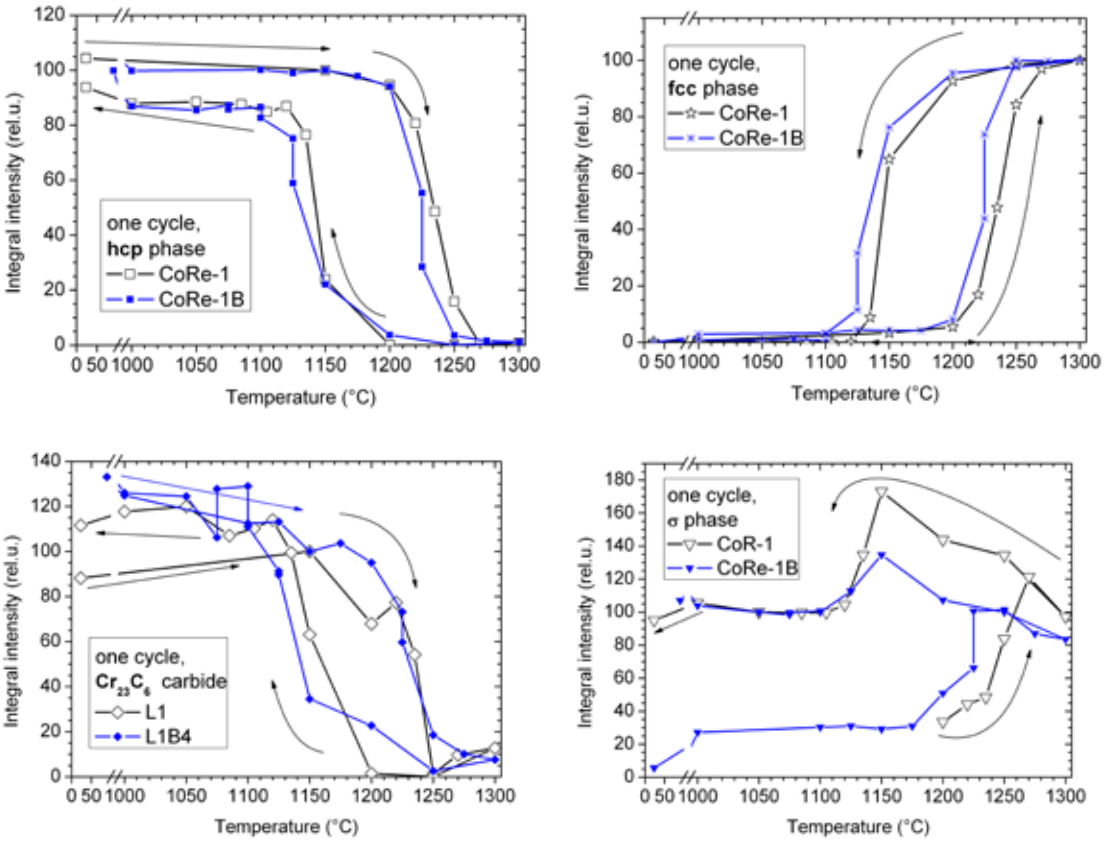

Figure 2: Evolution of hcp (a), fcc (b), $Cr_{23}C_6$ (c), and σ (d) phase in CoRe-1B alloy at high temperatures at the first cycle together with a comparison of CoRe-1 sample (without boron additions) measured at the first cycle. For a better overview error bars are not implemented. The error bars are +/- 1 for fcc and hcp phase, +/- 7 for $Cr_{23}C_6$ and +/- 3 for σ phase.

CoRe-1B was examined at SPODI. We followed the same thermal cycle as previously with the CoRe-1 [2]. The evolution of the main phases (hcp, fcc), as well as of the strengthening phases ($Cr_{23}C_6$ and σ phase) during the thermal cycle RT – 1300 °C – RT, was studied in this way and compared to the phase evolution previously measured in the CoRe-1 alloy [2].

Different transformation temperatures

The volume fraction evolution and peak intensities of the different phases in the CoRe-1 and CoRe-1B alloys during the cycle is shown in figure 2. In the CoRe-1B, the transformation hcp ↔ fcc (fig. 2a, b) with temperature increase occurs around 1225 °C (centre of transformation), and with temperature decrease around 1135 °C (centre of transformation). It differs slightly from the transformation temperature of CoRe-1 (1235 °C and 1140 °C, respectively). The shift in alloys with and without boron is less than 10 °C and part of the error is likely to be due to the uncertainty of temperature synchronization. The $Cr_{23}C_6$ phase shows no qualitative difference in CoRe-1 and CoRe-1B alloys. In CoRe-1, the hysteresis exhibited by the $Cr_{23}C_6$ carbides (fig. 2c) in the cycle is almost identical to that of the Co-hcp phase. On heating the Cr-carbide starts to dissolve at around 1120 °C and it is completely dissolved above 1250 °C (fig. 2c). During cooling, the precipitation of carbides starts below 1150 °C, rapidly reaching the original value. The amount of σ phase increases after cycling. The change in the σ content at RT before and after cycling is related to the change in the hcp matrix content. Similarly, the change in the σ content at high temperature is related to the change in the fcc matrix content. As in the case of CoRe-1, the alloy CoRe-1B stabilizes a greater amount of σ at the end of the thermal cycle compared to the initial amount before the thermal cycle (fig. 2d).

It should be stressed that the σ phase content in CoRe-1B follows the same evolution as in the alloy CoRe-1, the addition of boron does not exert a strong influence on the hysteresis.

[1] J. Rösler et al., Adv. Eng. Mater., 9, 876 (2007).

[2] R.Gilles et al., J. Phys: Conf. Ser., 340, 012052 (2012).

Hydrogen diffusion measurements in steels using neutron imaging

A. Griesche[1], K. Beyer[1], T. Kannengießer[1], E. Calzada[2]

[1]Bundesanstalt für Materialforschung und -prüfung, Berlin, Germany

[2]Technische Universität München, Forschungs-Neutronenquelle Heinz Maier-Leibnitz (FRM II), Garching, Germany

Revealing hydrogen embrittlement mechanisms in steels is of great interest to scientists and engineers. Neutron radiography makes it possible to measure in-situ hydrogen diffusion with high spatial and temporal resolution at concentrations as low as 20 ppm. We compare hydrogen-charged specimens with hydrogen-free reference specimens and use calibration standards to normalize the hydrogen concentrations. This allows quantitative tracking of the hydrogen concentration evolution as a function of time, space and temperature. Furthermore, a view into the material with "neutron eyes" facilitates the detection of cavities that contain molecular hydrogen.

The durability of steel can be limited by hydrogen assisted cracking. The uptake of hydrogen can occur during welding as well as during service due to corrosion. The associated failure mechanisms have been the subject of many investigations; see e.g. [1] for a review. However, the understanding of hydrogen mass transport by diffusion in steels is far from being fully comprehended.

Measuring the hydrogen distribution in steels with a sufficiently accurate local and temporal resolution allows for more detailed investigations of the hydrogen mass flow. Commonly used methods either destroy the sample, or yield insufficient spatial information on the hydrogen distribution. The feasibility of studying hydrogen diffusion in-situ using neutron radiography in steels has already been shown [2,3]. The temporal resolution of approximately 20 s per frame is fast enough to track the hydrogen diffusion with typical velocities in the µm/s range. The spatial resolution of about 70 µm is sufficiently accurate compared to the characteristic diffusion length, and also images the hydrogen concentration distribution at hydrogen concentrations as low as 20 ppmH.

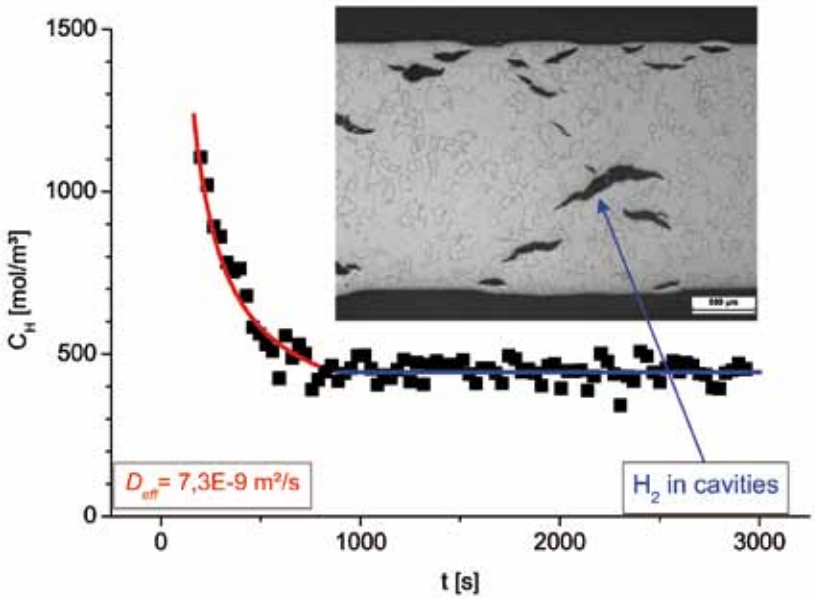

Figure 1: Hydrogen concentration (solid squares) as a function of time in technical iron at 350 °C. The red line is a fit of the appropriate solution of Fick's equation. The inserted light microscopic micrograph shows cavities in the sample.

Neutron radiography produces a two-dimensional attenuation distribution image. The large difference in the total scattering cross sections of hydrogen (σ_H = 82.02 barn) and iron (σ_{Fe} = 11.62 barn) results in a high contrast between the species of interest and the host matrix. In general, the transport of any species in a matrix can be monitored if the contrast is high enough, e.g. of Gd in Pd-alloys [4] or of Ag in Al-Cu-Ag [5].

Different aspects of diffusion behaviour

Transmission images of hydrogen-charged sample plates and non-charged references were taken simultaneously, together with three different mixtures of TiH_2 and SiC (containing 0, 10, and 200 ppmH) at ANTARES. The latter samples serve as calibration standards to convert image intensities into hydrogen concentrations. The scintillator screen was placed approximately 10 cm from the sample, reference and standards. The L/D = 400 setup offered good spatial resolution by sufficient flux. The exposure time was set to 20 s, using the optimal dynamic range of the camera.

Sample materials were technical iron, austenitic stainless steel and duplex stainless steel. The annealing temperature, the initial hydrogen concentration, the method of charging the samples with hydrogen, and the dislocation density of the materials were varied to study different aspects of the diffusion behavior. Effective diffusion coefficients were determined by fitting the appropriate solution of Fick's equation to the data.

Effusion of atomic hydrogen

Figure 1 shows an interesting concentration profile obtained in an isothermal effusion experiment. Instead of converging to zero, i.e. the atomic hydrogen completely diffuses out the sample, the hydrogen concentration remains constantly above zero for t > 1000 s.
The cavities were formed during electrochemical hydrogen charging of the samples. They contain excess hydrogen, which already recombines to H_2 when the solubility limit of the lattice is exceeded. Thus, the decay in figure 1 describes the effusion of atomic hydrogen coming from interstitial lattice sites (and we fit the diffusion equation only there) whereas molecular hydrogen remains inside. The elongation of the cavities corresponds to the rolling direction of the sheets [6].

Figure 2: Scientists of BAM work at ANTARES.

Neutron radiography is an excellent tool for investigating directly and in-situ hydrogen in steels. This method allows to gain insight into the material from a new and fascinating perspective.

[1] M. Dadfarnia et al., Adv. Mat., 22, 1128 (2010).
[2] K. Beyer et al., J. Mat. Sci., 46, 5171 (2011).
[3] K. Beyer et al., Nuc. Instrum. Meth. A, 651, 211 (2011).
[4] A. Griesche et al., BENSC Exp. Rep., ART-04-1080-EF, (2005).
[5] F. Kargl et al., J. Phys.: Cond. Matter, 23, 254201 (2011).
[6] D. Pérez Escobar et al., Corr. Sci., 53, 3166 (2011).

Enhanced kinetics of hydride-metal phase transitions in Mg by vacancy clustering

R. Checchetto[1], N. Bazzanella[1], A. Kale[1], A. Miotello[1], S. Mariazzi[1], R. S. Brusa[1], P. Mengucci[2], C. Macchi[3], A. Somoza[4], W. Egger[5], L. Ravelli[5]

[1]Università di Trento, Dipartimento di Fisica, Trento, Italy

[2]Università Politecnica delle Marche, Dipartimento di Fisica e Ingegneria dei Materiali e del Territorio, Ancona, Italy

[3]Istituto de Fisica de Materiales Tondil, UNCentro and CONICET, Tandil, Argentina

[4]Istituto de Fisica de Materiales Tondil, UNCentro and CICPBA, Tandil, Argentina

[5]Universität der Bundeswehr München, Institut für Angewandte Physik und Messtechnik, Neubiberg, Germany

The evolution of vacancies and vacancy clusters was studied using positron annihilation lifetime spectroscopy in nano-crystalline magnesium (Mg) samples submitted to successive H_2 sorption cycles. The desorption process was monitored measuring the H_2 desorption flux. The disappearance of intragranular vacancies after successive H_2 sorption cycles was found to be followed by an acceleration of the H_2 desorption process until stationary kinetics with the nominal H_2 absorption capacity of Mg was reached. The change in the kinetics is ascribed to the increase in vacancy clusters at grain boundaries, which assist the hydride in the metal phase transition.

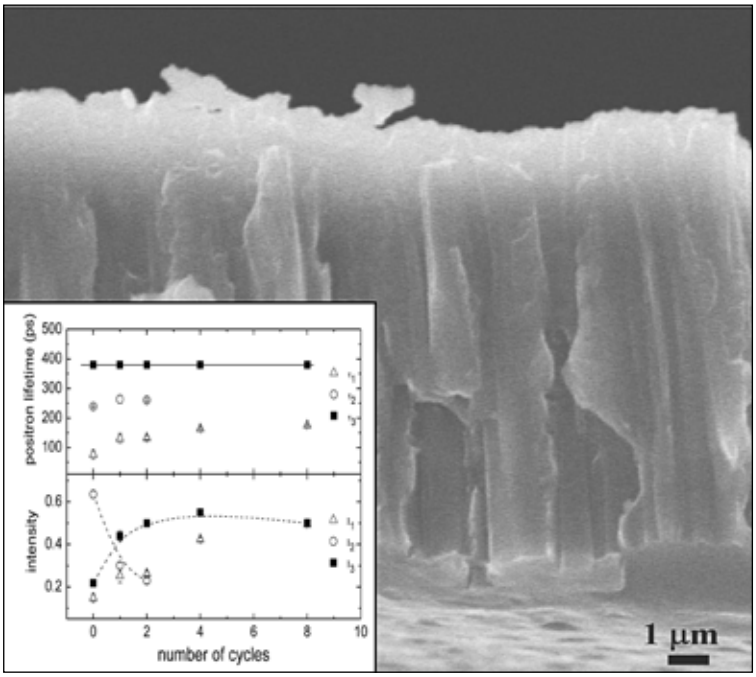

Figure 1: Scanning Electron Microscope micrograph: columnar structure of the Mg samples; Inset: Positron lifetimes and their associated intensities as a function of the H cycles. τ_1: reduced bulk lifetime. τ_2: positrons annihilated into vacancies. τ_3: positrons annihilated in vacancy-clusters. The lines are eye guides.

Mg is a good candidate for application in the hydrogen storage field since its hydride phase contains about 7.6 wt% of H. Basic research on Mg requires an understanding of the physical processes responsible for the reduction of the high temperature necessary for the dissociation of its hydride phase and the accelerated H_2 sorption kinetics which is slow in pure MgH_2 [1]. The kinetics is known to be accelerated either by reducing the Mg grain size, which improves the H diffusion and increases the active surface area, and/or by introducing defects that act as nucleation sites for the hydride to metal-phase-transition. This is the first work [2] dedicated to the study of the role of vacancy-like defects in H sorption kinetics. The detection of vacancy-like defects was made possible thanks the use of the in-depth sensitive Positron Annihilation Lifetime Spectroscopy (PALS).

Experiments at NEPOMUC using PLEPS

Mg samples were produced using radio frequency magnetron sputtering in the form of thick films (~ 10 µm) on graphite wafers. Scanning electron microscopy images show that Mg grows with columnar structure in which the lateral dimension of the columns is about 0.5 µm, their height being comparable to the film thickness (fig. 1). X-ray diffraction analysis indicates that Mg is nano-crystalline with a grain size of ~ 100 nm, and that the Mg layers grow in the (0002) orientation. To prevent surface oxidation and catalyze the H_2 dissociation and recombination, Mg films were coated with a 10 nm thick Pd capping layer. Samples peeled off from the substrate were activated using an annealing treatment at 573 K in H_2 atmosphere at 0.8 MPa and then submitted to H_2 sorption cycles at 623 K consisting of: i) an exposition to 1.5 MPa H_2 for 20 h to induce the

H_2 absorption (absorption step), and ii) the evacuation of the sample chamber to induce the H_2 desorption (desorption step). In the as-prepared sample and in samples after being submitted to 1, 2, 4, 8 sorption cycles, the presence of vacancy-like defects was measured by PALS using the apparatus PLEPS (Pulsed Low Energy Positron System) [3] at the high intensity positron source NEPOMUC (Neutron induced POsitron source MUniCh) [4]. The reported results were obtained at a depth between 1.5 and 2.4 μm, i.e. the bulk of the Mg film.

Use of the positron diffusion trapping model

Positron lifetime spectra were decomposed into three lifetime components (τ_1, τ_2, τ_3) with the corresponding intensities (I_1, I_2, I_3). Their behaviour, as a function of the sorption cycles, is shown in the inset of figure 1. Lifetime τ_1 comes from positrons annihilating into Mg bulk, while τ_2 and τ_3 are related to positron annihilation in vacancy-like defects. From ab initio Density Functional Theory calculations, the τ_2 experimental value (240 - 260 ps) was attributed to positron annihilation in a trap formed by mono- and di- vacancies and τ_3 = 380 ps to positron annihilation in vacancy clusters of a size equivalent to at least eight vacancies. The intensities I_2, I_3 are related to the defect concentration. The use of the positron diffusion trapping model allowed the concentration of vacancy (C_v) and vacancy clusters (C_c) to be obtained, and to support the inferred location of the defects: vacancies mainly at intragranular sites and clusters at grain boundaries. The C_v value of 1.2 x 10^{-5} at^{-1}, estimated for the as-prepared samples, decreases to 3.5 x 10^{-6} at^{-1} and 3 x 10^{-6} at^{-1} after the 1st and 2nd cycle respectively. Vacancies disappear after the 4th cycle. Simultaneously, positron trapping at the grain boundaries increases and the cluster concentration attains a lower limit value of C_c = 2 x 10^{-6} at^{-1}. By evaluating the area under the H_2 desorption curves for the 1st and 2nd cycle reported in figure 2, it is found that the H_2 desorbed amount is much lower than the nominal capacity of Mg, as long as intragranular vacancies are present. For the 4th and the 8th cycles

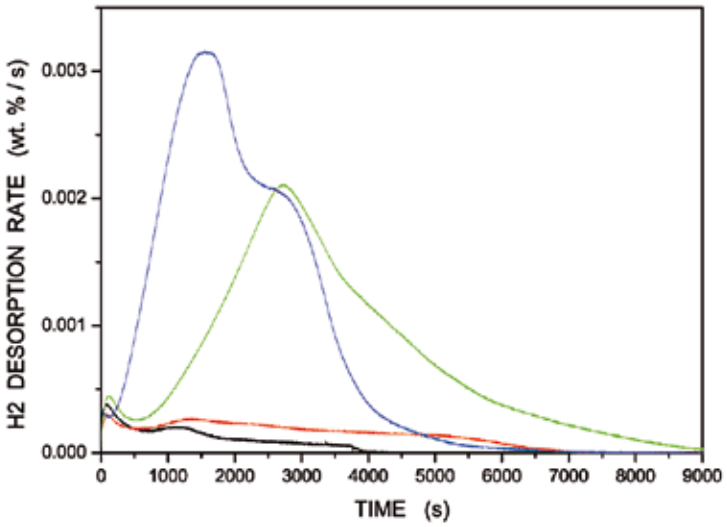

Figure 2: H_2 desorption spectra after the 1st (black), 2nd (red), 4th (green) and 8th (blue) sorption cycle.

there is a progressive increase in the desorption velocity and in the H_2 desorbed amount. After the 8th cycle it is close to the 7.6 wt%. The acceleration of the kinetics is evidenced by the shift to shorter times of the desorption peak in figure 2. Analysis of H_2 desorption curves using the Johnson-Mehl-Avrami (JMA) equation strongly suggests that the process is controlled by a nucleation and growth mechanism.

Vacancy clusters at grain boundaries accelerate the H_2 desorption process

Our experimental data suggested that vacancy clusters at grain boundaries lead to a change in the structure of the sites where the nucleation of the Mg phase occurs, causing an acceleration of the desorption kinetics. This is the first work showing the role of vacancies and vacancy clusters in assisting the kinetics of hydride to metal phase transition.

[1] J. Huot et al., Appl. Phys. A: Mat. Sci. Process., 72 (2), 187 (2001).

[2] R. Checchetto et al., Phys. Rev. B, 84 (5), 054115 (2011).

[3] W. Egger, Physics with Many Positrons; Eds: R.S. Brusa et al., IOS Press: Amsterdam, 419 (2010).

[4] C. Hugenschmidt, Physics with Many Positrons; Eds: R.S. Brusa et al., IOS Press: Amsterdam, 399 (2010).

Positron annihilation in Au, Cr and Cu layers and positron quantum confinement in Au clusters

P. Pikart[1,2], M. Reiner[1,2], Ch. Hugenschmidt[1,2], M. Horisberger[3], Y. Matsukawa[4], M. Hatakeyama[4], T. Toyama[4], Y. Nagai[4]

[1]Technische Universität München, Physics Department E 21, Garching, Germany

[2]Technische Universität München, Forschungs-Neutronenquelle Heinz Maier-Leibnitz (FRM II), Garching, Germany

[3]Paul Scherrer Institute, Laboratory for Developments and Methods, Villingen, Switzerland

[3] Tohoku University, Institute for Materials Research, IMR, Oarai, Japan

Ultra thin chrome, copper and gold layers embedded in aluminium were studied using coincident Doppler broadening spectroscopy (CDBS) with a monoenergetic positron beam. This technique makes it possible to find and identify nanometer-scale agglomerations in bulk materials. A high sensitivity was achieved at an embedded Au layer of only 2 nm thickness below a surface of 200 nm aluminium, which was attributed to the efficient positron trapping in Au agglomerations. A positron implantation and diffusion model is applied to describe the observed high sensitivity for positron trapping layers. In addition, a quantum-well model for the positron wave function limits the trapping to gold clusters of a radius larger than 0.23 nm. This result was confirmed experimentally and validated with complementary TEM measurements. [1]

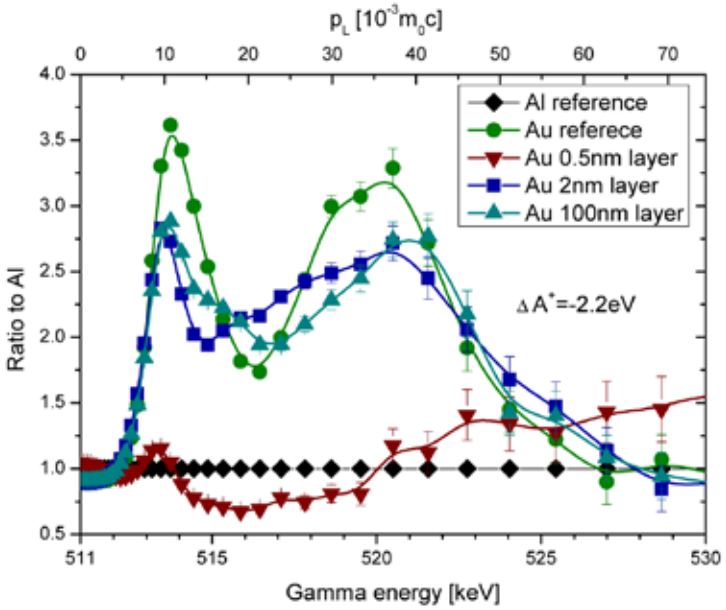

Figure 1: The CDBS results for three gold layers of different thickness embedded in aluminium.

A series of CDBS measurements was performed on samples with embedded layers of different positron affinities and various thickness. This systematic investigation revealed a very distinct CDBS response to different types of embedded layers.

Firstly, vacancy-like defects were able to be analyzed at embedded layers with equal or repulsive positron affinity (Cr and Cu in Al) and at a very thin attractive layer (Au in Al). Vacancies are formed at the interface, especially if the lattice mismatch is high and leads to positron trapping.

Positron attracting clusters

Secondly, due to the difference in the element-dependent positron affinity, an attractive potential step is formed at the interface that enhances the positron annihilation with electrons of the elements having higher positron affinity. The CDBS reflects the momentum distribution of the electrons at its annihilation site, which is an indicator of the chemical environment. Hence, the 2 nm Au layer embedded under 200 nm of aluminium could be detected with 83 % of the CDBS signal of a pure gold reference measurement (fig. 1).

This is a consequence of positron attracting clusters, which exceed the critical size of a three dimensional quantum well to form a bound state and, therefore stable trapping of the positron in the gold cluster. The implantation of the positron beam was calculated using the Makhov-approximation and the diffusion of the implanted positrons was simulated by a random walk.

The results of the simulation (fig. 2) confirm that a majority of the positrons is trapped at the layer

in a depth of 200 nm. The trapping clusters could be detected by complementary TEM measurements (fig. 3).

Sensitivity to small variations

Moreover, the results obtained for the 0.5 nm and the 2 nm Au layers embedded in Al differ widely. This demonstrates the extremely high sensitivity to small variations of the elemental concentration in the sample. The theoretically calculated positron affinity was proved to be a sound basis for the understanding of a quantum confinement based model of the positron trapping in Au clusters with a minimum diameter of 0.46 nm surrounded by Al.

Positron trapping at metallic agglomerations

We succeeded in determining experimentally the conditions and parameters for effective positron trapping at metallic agglomerations. Since positron trapping can not be predicted reliably by calculations, these results show the great importance of measurements on layered metallic model systems for further applications of CDBS. For example, in material research CDBS can be applied to characterize age hardenable alloys, which can be hardened by precipitation growth. Since CDBS measurements can be performed non-destructively and *in situ* during the heat treatment, this technique is expected to be predestined for the analysis the early stages of precipitation growth.

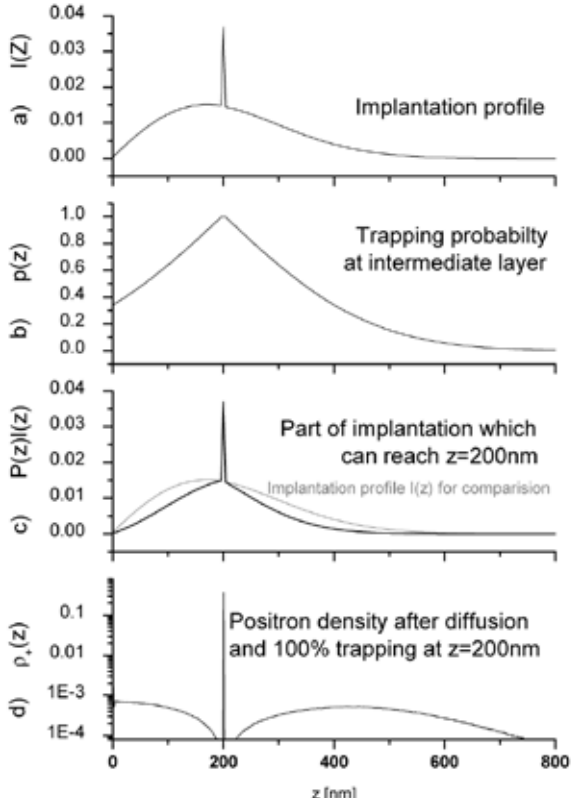

Figure 2: The simulated positron density before (a) and after the trapping process (d)

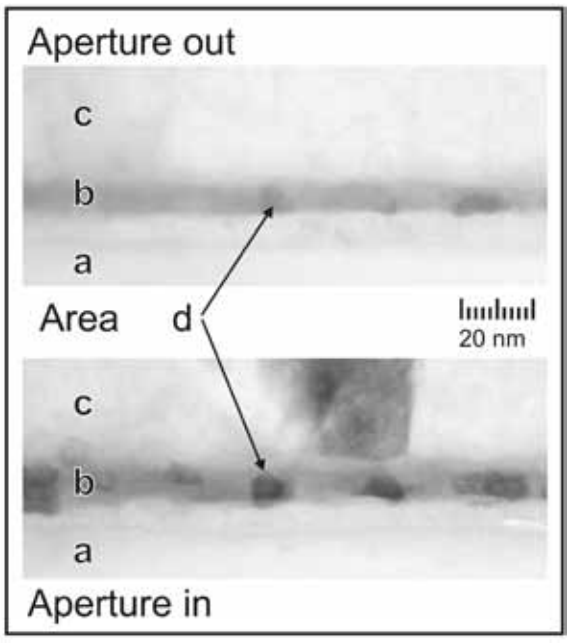

Figure 3: TEM picture of the embedded particles. “Aperture out” designates the bright field image which shows the density distribution, while “Aperture in” designates the picture mapping crystallographic orientations.

[1] P. Pikart et al., Phys. Rev. B, 84, 014106 (2011).

The whole range of hydrogen bonds in one crystal structure

M.-D. Şerb[1], R. Wang[2], M. Meven[3], U. Englert[2]

[1]University Politehnica of Bucharest, Bucharest, Romania

[2]Rheinisch-Westfälische Technische Hochschule Aachen, Aachen, Germany

[3]Technische Universität München, Forschungs-Neutronenquelle Heinz Maier-Leibnitz (FRM II), Garching, Germany

Neutron and high resolution X-ray diffraction experiments at 100 K have been used to derive the precise geometry and the electron density of a wide range of X–H···O interactions in the organic salt *N,N*-dimethyl-biguanidinium-bis(hydrogensquarate). The shortest O–H···O bond does not follow the trend of the remaining hydrogen bonds: It is significantly more symmetric, and electron density criteria support the concept of an interaction with intermediate character between covalent and closed-shell.

Hydrogen bonding represents an interaction of paramount importance in structural biology. Proton transfer along hydrogen bonds is an important reaction step for a variety of chemical systems. Hydrogen bonds of all flavours are used as interactions in crystal engineering. Not only the structural consequences, but also the very nature of hydrogen bonds has stimulated discussion: Shorter and presumably stronger interactions are associated with more covalent, longer with predominantly electrostatic character, but the experimental basis is still limited. Ideally, neutron diffraction should provide the precise location of the proton in short hydrogen bonds while charge density studies, followed by topological analysis of the electron density [1], should characterize bonds as more or less covalent. In this contribution, we report the result of such an experiment. In the title compound *N,N*-dimetyl-biguanidinium-bis(hydrogensquarate), referred to as *(1)*, hydrogen bonds of very different length and strength occur next by next in the same crystal structure - a perfect situation to establish subtle trends. We will show that very short hydrogen bonds can at least in part be regarded as covalent.

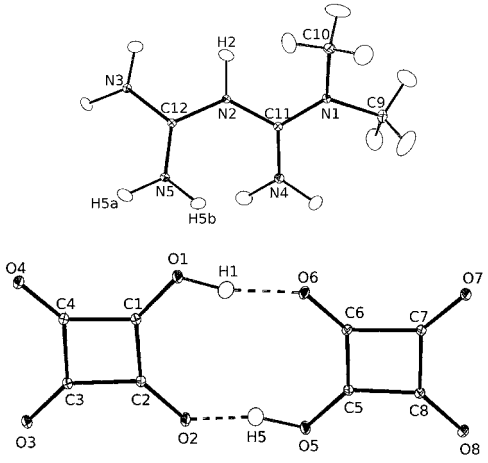

Figure 1: Displacement ellipsoid plot (30 % probability) of a dication and a dianion in the organic salt *N,N*-dimetyl-biguanidinium-bis(hydrogensquarate), referred to as *(1)*. Two hydrogen monosquarate anions interact via the shortest hydrogen bonds in this crystal structure with donor···acceptor distances of 2.447(3) Å and 2.568(3) Å.

Neutron diffraction at HEiDi

Details about synthesis, X-ray diffraction and structure solution/refinement of *(1)* are given in the full paper [2].

Neutron diffraction was performed at FRM II on the single crystal diffractometer (SCD) HEiDi (λ = 0.868 Å) at 100 K. An 0.5 mm Er-foil was used to suppress $\lambda/2$ contamination. The Bragg data were collected in rocking–scan mode. The program used for data reduction was PRON2010.

Discussion of hydrogen bonds

In the solid state, the organic salt *(1)* consists of dications and pairs of monoanions (fig. 1). Shorter H···A interactions are associated with stronger bonds; the concomitant effect of significantly elongated D-H distances is only observed for short interactions. The two O–H···O interactions differ with respect to their donor···acceptor distances, and the shorter hydrogen bond O1–H1···O6 is more symmetric than O5–H5···O2. On the one hand, O1–H1 is remarkably elongated and not only longer than O5–H5 but also than all N–H bonds. On the other hand, O6···H1 represents by far the shortest among all X···H interactions in this structure.

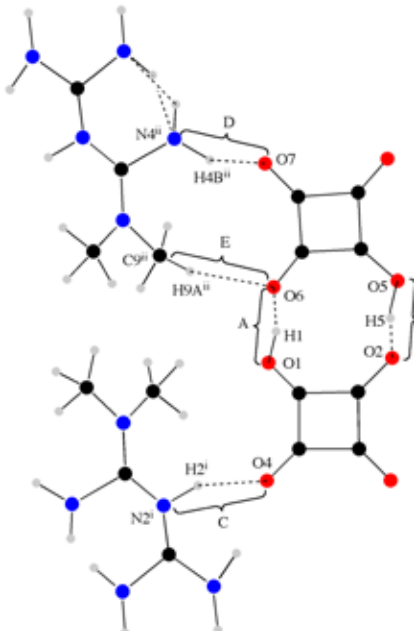

Scheme 1: Selected hydrogen bonds of different strength in *(1)*. Symmetry operators: i = 1+x, 1+y, z; ii = 2-x, 1-y, 1-z.

Electron density as a criterion for the strength of hydrogen bonds relies on high resolution X-ray diffraction and benefits from neutron diffraction data to deconvolute vibrational and electronic effects on the experimental charge density. For the classical hydrogen bonds, (3, -1) critical points are detected in the hydrogen···acceptor part of the interactions. The electron density ρ_{bcp} in these bond critical points represents an intuitive criterion for characterising the H bonds; it amounts to 0.64(2) e/Å^3 for the shortest interaction and decreases for longer H···A distances. The Laplacian $\nabla^2\rho_{bcp}$ of the electron density represents a sensitive tool for establishing the closed-shell or shared character of an interaction. Our experimental data indicate a clear discrepancy from linear behaviour: For the hydrogen bonds E - C in Scheme 1 with donor···acceptor distances

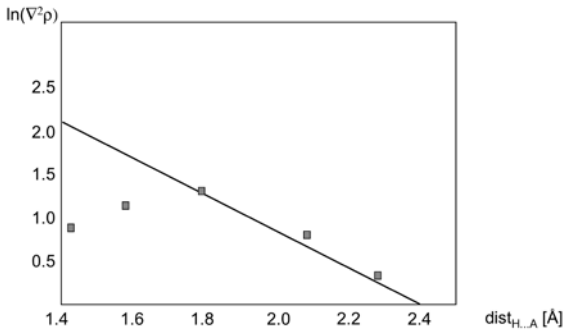

Figure 2: Experimental data points $\ln\nabla^2\rho_{bcp}$, dist(H···A) for the hydrogen bonds in Table 1 and linear relationship $\ln\nabla^2\rho_{bcp}$ = 5.1 - 2.14·dist(H···A) (straight line; [3]).

Properties of the hydrogen bonds represented in Scheme 1

no. in Scheme 1	A	B	C	D	E
D D···A (Å)	2.447(3)	2.568(3)	2.742(2)	3.008(2)	3.211(3)
D D-H (Å)	1.048(4)	1.022(4)	1.034(4)	1.010(4)	1.070(7)
D H···A (Å)	1.421(4)	1.569(4)	1.779(4)	2.068(5)	2.265(7)
< D- H···A (°)	164.6(4)	164.5(4)	153.2(3)	154.1(4)	146.3(5)
ρ (e/Å^3)	0.64(2)	0.37(2)	0.24(2)	0.090(9)	0.072(4)
$\nabla^2\rho$ (e/Å^5)	2.43(5)	3.14(4)	3.69(3)	2.21(2)	1.391(2)

longer than 2.5 Å, $\nabla^2\rho$ in the bond critical point assumes the expected small positive values. For the shortest contacts B and, in particular, A, the numerical trend is inverted: Figure 2 shows that for the O-H···O interactions smaller positive values of the Laplacian are found than expected from the logarithmic relationship derived by Mata et al. [3].

Variety of hydrogen interactions

The title compound enabled us to directly compare very different hydrogen bonds. Neutron diffraction allowed to classify the shortest interaction as more symmetric than usual, with a significantly elongated donor-hydrogen bond and a rather short hydrogen···acceptor contact. Direct comparison has been made to strong and moderately strong classical and to weak non-classical X–H···O interactions. The Laplacian of the electron density reveals that the shortest hydrogen bond does not simply follow the trend of the longer contacts but rather represents a borderline case in-between a covalent and a closed-shell interaction.

Acknowledgements

DFG, priority program 1178; DAAD for fellowship to M.-D. S.

[1] Bader, R. F. W., Atoms in Molecules: A Quantum Theory, Clarendon Press, Oxford, UK (1990).

[2] Şerb, M.-D. et al., Acta Crystallogr., Sect. B, 67 (6), 552 (2011).

[3] Mata, I. et al., Chem. Eur. J., 16 (8), 2442 (2010).

Antiferroelectric and ferroelectric mixed crystal: $Rb_{0.51}Tl_{0.49}H_2PO_4$

I. H. Oh[1], M. Meven[2], G. Heger[3] and K. S. Lee[4]

[1]Korea Atomic Energy Research Institute, Neutron Science Division, Daejeon, Korea

[2]Technische Universität München, Forschungs-Neutronenquelle Heinz Maier-Leibnitz (FRM II), Garching, Germany

[3]Rheinisch-Westfälische Technische Hochschule Aachen, Institut für Kristallographie, Aachen, Germany

[4]Inje University, Center for Nano Manufacturing, Department of Nano System Engineering, Gimhae, Korea

Crystal structure analysis on a mixed crystal $Rb_{0.51}Tl_{0.49}H_2PO_4$ was carried out at room temperature using neutron diffraction. RbH_2PO_4 (RDP) clearly exhibits a different crystal structure, although Rb^+ and Tl^+ have almost the same ionic radii. The crystal structure of the title compound is isotype to TlH_2PO_4 (TDP), having partially disordered H atoms in strong symmetric O—H—O hydrogen bonds. Lone-pair electrons of the Tl^+ ions stabilize the two-dimensional network of hydrogen bonded PO_4-groups.

Due to the ordering phenomenon of the H, D atoms in short and strong O—(H,D)—O hydrogen bonds of about 2.5 Å, the $A(H,D)_2PO_4$-type (A = K^+, Li^+, Rb^+, Cs^+, Tl^+, etc.) crystals exhibit very well known ferric properties and divergent structural phase transitions. The characteristic of the crystal structure of RbH_2PO_4 (RDP) is a three-dimensional network of PO_4 groups linked by hydrogen bonds. Contrary to RDP, TlH_2PO_4 (TDP) features two-dimensional networks composed of double layers of hydrogen-bonded PO_4 groups. Although Tl^+ and Rb^+ ions have the same ionic radii (about 1.47 Å), the crystal structures of RDP and TDP are clearly different [1-2]. The aim of the investigation is to discuss the role of H-disorder in the hydrogen bonds, the effects of the Tl to Rb ratios and the lone-pair electrons of Tl^+ ions on the crystal structure of $Rb_{(1-x)}Tl_xH_2PO_4$ mixed crystals.

Figure 1. Photograph of mixed crystals. A single crystal of good shape (located center) was selected using a polarized microscope and used for neutron diffraction experiments.

Single crystals of $Rb_{0.51}Tl_{0.49}H_2PO_4$ ($R_{0.51}$TDP) were grown from aqueous solution using the evaporation method at room temperature according to the following chemical reaction

$$(Tl_2CO_3)_{0.49} + (Rb_2CO_3)_{0.51} + 2H_3PO_4 \rightarrow 2Rb_{0.51}Tl_{0.49}H_2PO_4 + CO_2\uparrow + H_2O.$$

A crystal of 2 x 2 x 1 mm^3 was used for single crystal neutron diffraction (fig. 1). The measurements at room temperature were performed on the four-circle single diffractometer HEIDI (λ = 0.868 Å). A careful exploration of reflection conditions revealed the monoclinic space group $P12_1/a1$ with lattice parameters a = 14.4281(1) Å, b = 4.543(5) Å, c = 6.400(9) Å, and β = 91.77(9)°. For the crystal structure obtained see figure 2.

To determine the real ratio of Rb to Tl, the effective neutron scattering length b_{eff} = 7.915(9) fm was refined and the Tl content x calculated according to

$$b_{eff} = xb_{Tl} + (1 - x)b_{Rb}$$

and

$$x = (b_{eff} - b_{Rb}) / (b_{Tl} - b_{Rb}).$$

With b_{Rb} = 7.09(2) fm and b_{Tl} = 8.776(5) fm, the result x = 0.49(1) corresponds to a composition of $Rb_{0.51}Tl_{0.49}H_2PO_4$.

Crystal structure

The crystal structure of $R_{0.51}$TDP at room temperature is characterized by the existence of three crystallographically different hydrogen atoms. H1 and H2, are disordered in strong and short symmetric O—H—O hydrogen bonds whereas H3 is ordered in an ordinary asymmetric H-bond. H1 and H2, occupying inversion centers -1 (special positions), exhibit large amplitudes along the O—O bond directions, which is evidence for their

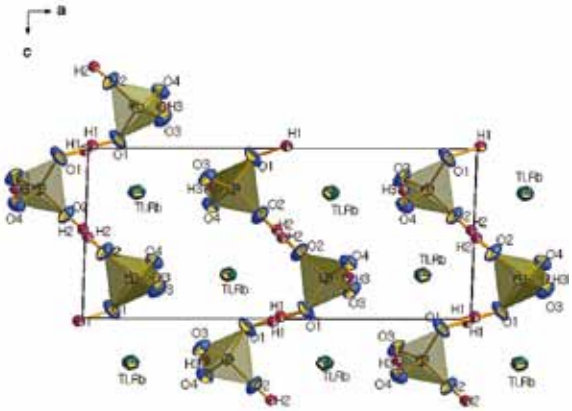

Figure 2: Crystal structure of mixed crystal at room temperature along the b-axis.

disordered character. In contrast, the ordered H3 is situated in a general position. Through H1 and H2, the PO_4 tetrahedra are linked by hydrogen bonds and as a result PO_4-H-PO_4-H-PO_4 zig-zag chains are formed along the c-axis. These chains are connected by O3-H3—O4 hydrogen bonds in the b direction, leading to a layer structure parallel to the b, c plane. Adjacent two-dimensional hydrogen bond networks are cross-linked by Coulomb interactions with Tl^+/Rb^+ ions.

In comparison to previous studies [1, 2], only the O1-H1-O1 hydrogen bond angles of the split atom refinement are substantially changed in the case of the mixed crystals. The reason why only O1-H1-O1 out of two disordered bonds shows a dependency on the Rb^+ ion content is unclear. According to Rios et al. [3], it seems that only the O1-H1-O1 hydrogen bond plays a significant role in the structural phase transitions, and it is supposed that H2 attached to oxygen atoms moves just behind the motion of the PO_4 groups. The O—H—O hydrogen bond angles become flatter from TDP to the mixed crystal 172.6° (averaged value for TDP at 295 K/240 K) to 175.8° in $R_{0.46}$TDP and 176.5° in $R_{0.51}$TDP for O1—H—O1 and from 175.6° (averaged value for TDP at 295 K/240 K) to 176.5° in $R_{0.46}$TDP and 176.1° in $R_{0.51}$TDP for O2—H—O2. Due to the inert pair effect, the metal ions such as Tl^+, Pb^{2+} or Bi^{3+} exhibit structurally distorted polyhedra [4]. To avoid the unfavourable interaction between $Tl6s^2$ and $O2p^6$, the lone pair distortion about Tl^+ ions is caused. In the crystal structure of RDP, the distances between the Rb^+ ions and the O atoms are more or less isotropic, ranging from 2.943 Å to 3.027 Å (average 2.985 Å) at room temperature. Compared to RDP, the Tl^+(Tl^+/Rb^+)-O nearest neighbour distances range from 2.811(3) Å to 3.182(2) Å for $R_{0.51}$TDP (fig. 3). There may be some tendency for the average Tl(Tl/Rb)–O distance to be reduced with increasing Rb content from 3.003(5) Å for TDP to 3.005(7) Å for $R_{0.46}$TDP and 2.991(2) Å for $R_{0.51}$TDP. The corresponding mean Rb–O distance in RDP is 2.985 Å. The mean square displacement of O1 involved in the shortest Tl(Tl/Rb)–O bond length is systematically larger compared to the other oxygen atoms. This phenomenon might be explained by

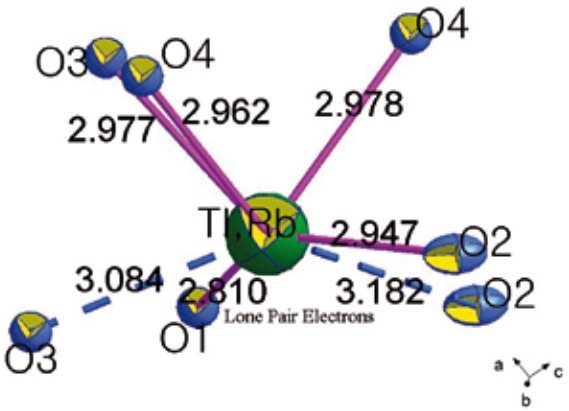

Figure 3: Tl-O coordination and bond distances (Å) in mixed crystal at room temperature. The position of the Tl^+ $6s^2$ lone-pair electrons is indicated.

the orientation of the lone-pair electrons of Tl^+. This tendency can also be seen in other lone-pair bearing compounds with e.g. Pb-O polyhedra. The short Tl-O bond distance is directly related to the stereochemical activity of the lone pair electrons of Tl^+ ions. It is assumed that adding more Rb^+ ions into the crystal structure makes the lone pair electrons of the Tl^+ ions move to the other side and that this causes the rotation of the PO_4 tetrahedra.

[1] I. H. Oh et al., Acta Crystallogr. B, 62, 719 (2006).
[2] I. H. Oh et al., J. Phys. Soc. Jpn., 77, 094602 (2008).
[3] S. Rios et al., Acta Crystallogr. B, 54, 790 (1998).
[4] P. B. Moore et al., Am. Mineral., 74, 1186 (1989).

Disorder of $(NH_4)_3H(SO_4)_2$ in the high-temperature phase: single-crystal neutron diffraction studies

Y. J. Sohn[1], K. M. Sparta[1], M. Meven[2], G. Heger[1]

[1]Rheinisch-Westfälische Technische Hochschule Aachen, Institut für Kristallographie, Aachen, Germany

[2]Technische Universität München, Forschungs-Neutronenquelle Heinz Maier-Leibnitz (FRM II), Garching, Germany

The crystal structure of $(NH_4)_3H(SO_4)_2$ in the high-temperature phase was studied with respect to H-disorder using single-crystal neutron diffraction. According to the disordering of the O atom in the SO_4-H-SO_4 hydrogen bond, a pseudo-hexagonal network is formed in the (001) plane. The disordered H atoms in these hydrogen bonds, as well in the ammonium groups, are refined using a split-atom model. Finally, a possible supplementary proton migration between the ammonium protons and those of the hydrogen bonds is considered and shown.

The high-temperature phase of $(NH_4)_3H(SO_4)_2$ (TAHS) above 413 K crystallizes in the rhombohedral space group R-3m [1] and is well known for its superprotonic conductivity [2,3]. This high protonic conductivity in the (001) plane is due to the disordered hydrogen-bond networks [4]. While isolated hydrogen-bonded $(SO_4)H(SO_4)$ dimers are characteristic of the crystal structure

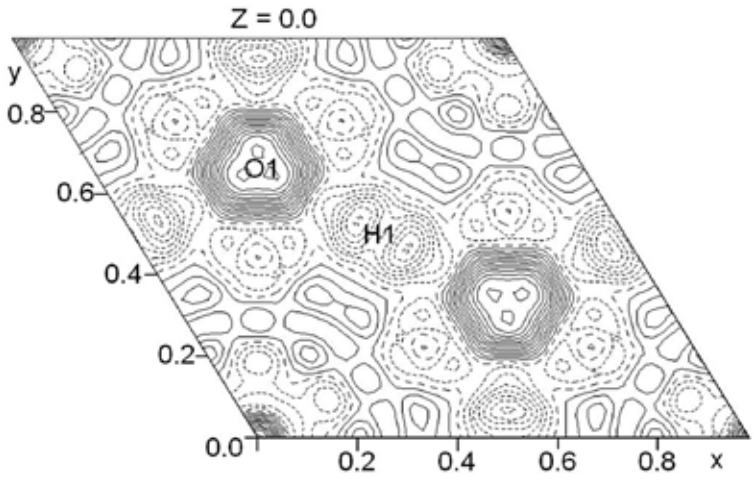

Figure 1: Difference-Fourier map for the O and H atoms. Positive (solid line) and negative (dotted line) contours are drawn in steps of 0.2 nsl Å^{-3} (nsl = neutron scattering lengths). The negative H density is due to the negative neutron scattering length of the proton.

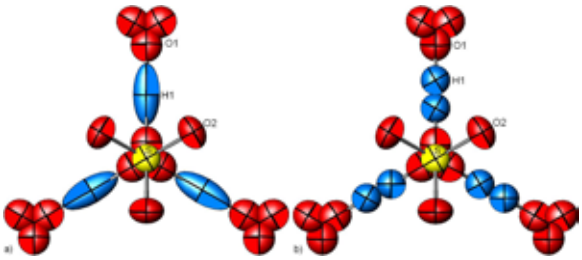

Figure 2: O-H-O hydrogen bond network in the (001) plane (view along [001]). (a) Conventional model, (b) split-atom model. Displacement ellipsoids are drawn at the 50 % probability level.

of the room-temperature phase of TAHS, a two-dimensional pseudo-hexagonal network of hydrogen bonds between the SO_4 groups is formed during the high-temperature phase. The H atom positions of the hydrogen bond are not fully occupied, thus allowing the H atoms to move almost freely between energetically equivalent positions.

In order to understand the highly disordered crystal structure of TAHS in the high-temperature phase, especially in respect to the proton distribution, we carried out single-crystal neutron diffraction studies. A possible pathway for superprotonic conductivity is discussed according to the results of the crystal structure analysis.

Single TAHS crystals of optical quality were grown from aqueous solution by means of slow evaporation. Samples of typically 3 x 3 x 3 mm^3 were used for single-crystal neutron diffraction experiments. A complete dataset of Bragg reflection intensities was collected up to $(\sin\theta/\lambda)_{max}$ = 0.9 Å^{-1} on the four-circle diffractometer HEiDi at the FRM II with a wavelength of λ = 0.555 Å [Cu(420) monochromator] at 413(2) K.

A difference-Fourier map suggests further split-

ting of the H atoms in the SO_4-H-SO_4 hydrogen bonds in addition to the O atom (fig. 1). The O-H-O hydrogen-bond network obtained from conventional and split-atom models is shown in figure 2. The ammonium groups are also refined using a split-atom model due to the large anisotropic displacements of ammonium protons. As a result, six possible tetrahedral orientations were found for each group (fig. 3), indicating a fast reorientational motion.

Finally, possible pathways for proton conduction are considered with respect to the crystal structure. A supplementary proton exchange, as reported by NMR studies [5], was also supported by our single-crystal neutron diffraction studies and illustrated in figure 4. The nuclear density maps show a clear correlation between displacements of the protons in the hydrogen

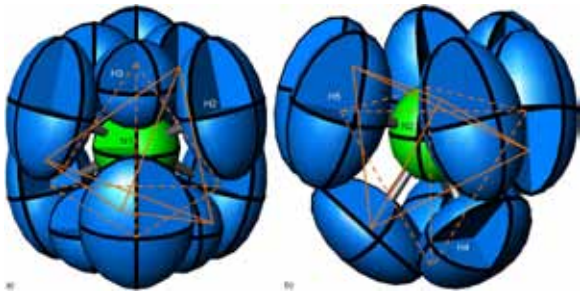

Figure 3: Building principle of one of six possible NH_4^+ tetrahedra. (a) $N1H_4^+$ tetrahedron. (b) $N2H_4^+$ tetrahedron. Dashed lines indicate the NH_4^+ tetrahedral orientations for a conventional model and solid lines are examples for NH_4^+ orientations in the split-atom model. Displacement ellipsoids are drawn at the 50 % probability level.

bonds and of the ammonium protons.
Using single-crystal neutron diffraction, a more detailed crystal structure analysis of the high-temperature phase of TAHS, with special emphasis on the proton distribution is performed. With respect to the crystal structure, possible pathways for superprotonic conductivity are illustrated.

Moreover, the short distance of H atom positions between SO_4-H-SO_4 hydrogen bonds and the adjacent ammonium group supports the idea of a supplementary proton exchange, as reported earlier [5]. Regarding the strongly enlarged anisotropic displacements of the ammonium protons, a split-atom model is applied that assumes a fast reorientational motion of the ammonium groups.

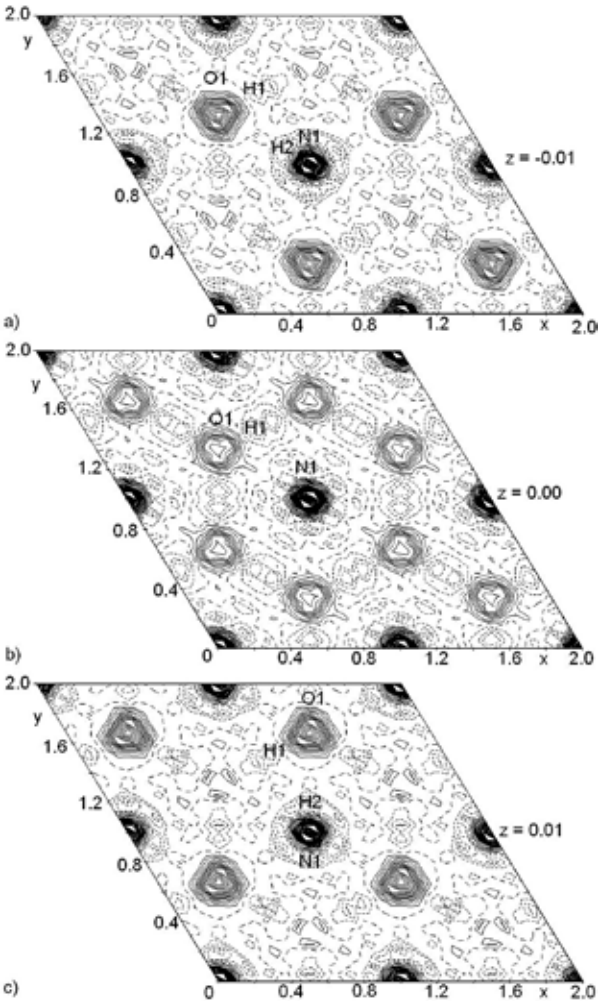

Figure 4: Nuclear density map F_{obs} of hydrogen bonds in the (001) plane. (a) z = -0.01; (b) z = 0.00; (c) z = 0.01. Positive (solid line) and negative (dotted line) contours are drawn in steps of 0.5 nsl $Å^{-3}$.

[1] K. Friese, et al., J. Solid State Chem., 165, 136 (2002).
[2] L. Schwalowsky et al., J. Phys. Condens. Matter, 10, 3019 (1998).
[3] R. H. Chen et al., J. Phys. Chem. Solids, 61, 1399 (2000).
[4] A. I. Baranov, Crystallogr. Rep., 48, 1012 (2003).
[5] M. Fechtelkord et al., Solid State Nucl. Magn. Reson. 17, 76 (2000).

Prompt gamma activation analysis on orange coloured zinc oxide samples

S. Soellradl[1,2,3,4], M. Greiwe[3], V. J. Bukas[3], L. Canella[4], A. Senyshyn[4], P. Kudejova[4], Zs. Revay[4], T. Nilges[3], A. Türler[1,2], R. Niewa[5]

[1]University of Bern, Department of Chemistry and Biochemistry, Bern, Switzerland

[2]Paul Scherrer Institute, Villigen, Switzerland

[3]Technische Universität München, Fakultät für Chemie, Garching, Germany

[4]Technische Universität München, Forschungs-Neutronenquelle Heinz Maier-Leibnitz (FRM II), Garching, Germany

[5]University of Stuttgart, Institute of Anorganic Chemistry, Stuttgart, Germany

Zinc oxide is a direct, wide band gap semiconductor. It is expected to exhibit promising properties for applications in, for example, optoelectronic devices, once sufficient doping can be achieved. Different molar ratios of Urea to $Zn(NO_3)_2 \cdot 6\ H_2O$ are used to prepare orange coloured ZnO samples using the method of solution combustion synthesis. The samples were characterised by means of powder x-ray diffraction, elemental analysis for H, C, N, Raman spectroscopy and qualitatively by energy dispersive x-ray spectroscopy and prompt gamma activation analysis. Since nitrogen has a characteristic high-energy prompt gamma line at 10.829 MeV, PGAA is a non-destructive technique for nitrogen measurements in almost any chemical matrix with minor sample preparation. An additional phase was found in samples prepared using a molar ratio of 2.3 : 1, containing significant concentrations of hydrogen, carbon and nitrogen.

PGAA advantageous in analysis of light elements

Pure ZnO crystals are transparent in the visible part of the spectrum, while powder is colourless.

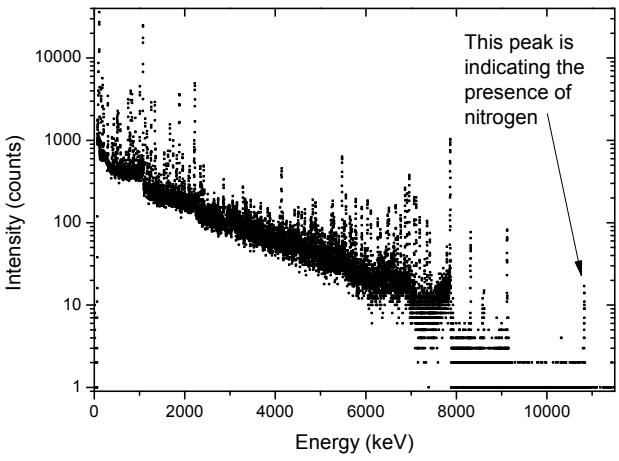

Figure 1: PGAA spectrum of the orange coloured product of a sample, prepared using a molar ratio of Urea to $Zn(NO_3)_2 \cdot 6\ H_2O$ of 2.3 : 1.

The samples for the quantification of nitrogen using prompt gamma activation analysis (PGAA) are prepared as described in [1] to measure the detection limits of nitrogen within a ZnO matrix. PGAA proved to be advantageous in the analysis of light elements. Nitrogen has a relatively low cross section, but its highest energy line is still relatively strong in the spectrum. This characteristic peak normally appears without any background at the very end of the spectrum (fig. 1). Based on this characteristic peak, nitrogen can be detected even when only a few counts are detected. The PGAA spectrum of the material studied is shown in figure 1.

Strong orange colour

The synthesis of ZnO was performed as described in [1]. Mixtures with different molar ratios of Urea to $Zn(NO_3)_2 \cdot 6\ H_2O$ were dissolved in deionised water, and then heated in a muffle furnace at 500 °C for 10 minutes. When the water had evaporated, the reaction started with an intense flame. The colour of the product is highly dependent on the molar ratio of Urea : $Zn(NO_3)_2 \cdot 6H_2O$, a strong orange colour can be observed at the ratio of 1 : 1, which fades towards the ratio of 5 : 1.

The samples were analysed using PGAA, Raman spectroscopy, powder x-ray diffraction (PXRD), and qualitatively, with energy-dispersive x-ray spectroscopy (EDX). The results have been compared to results published in [1]. In the Raman spectrum, in addition to pure ZnO, bands appear at 277, 509, 580 and 1046 cm^{-1}. These bands have been taken in the literature to indicate nitrogen doping [1,2]. Our measurements show that two more bands appear at 748 cm^{-1} and 1043 cm^{-1}, signifying the presence of another phase.

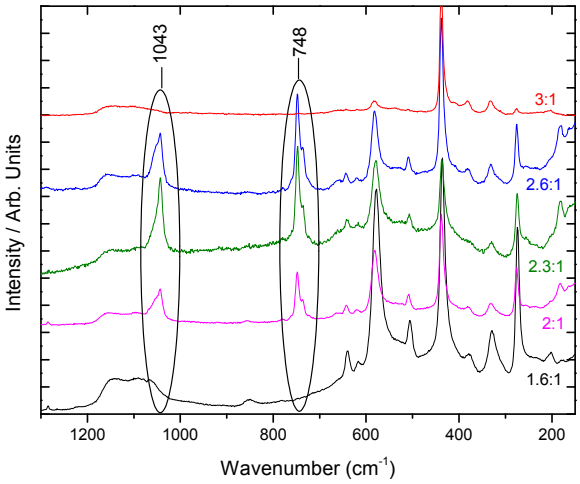

Figure 2: Raman spectra of samples prepared using different molar ratios. The maximum intensity for the λ = 632.8 nm band (excited with a HeNe laser) was observed for the sample from 2.3 : 1 ratio.

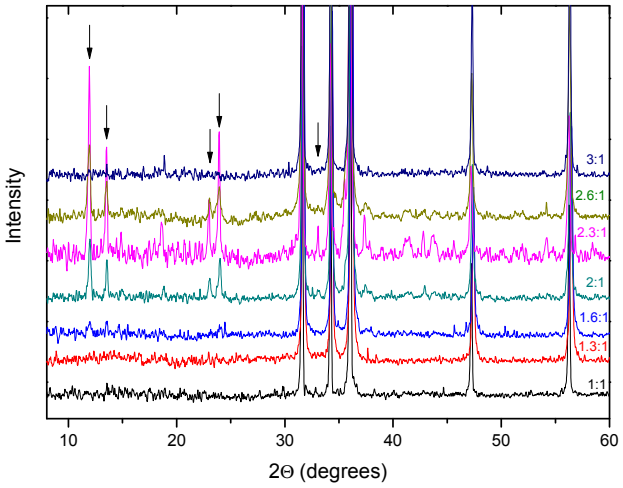

Figure 3: X-ray diffraction patterns (Cu Kα$_1$, λ = 1.5405 Å) of samples prepared using different molar ratios are shown. Additional reflections indicate the maximum amount of the additional phase for a ratio of 2.3 : 1.

For the samples with these additional Raman bands (fig. 2), the presence of additional reflections is also observed in the diffraction pattern (fig. 3).

PGAA measurements were performed on the orange-coloured sample, prepared using molar ratios of 1 : 1 and 2.3 : 1.

It is possible to dissolve the synthesis product in 20 % HCl at 70 °C. Upon cooling, white crystals form at the surface of the HCl solution at a temperature of approximately 65 °C, proving the presence of an additional phase. Qualitative EDX measurements revealed only the presence of H, C, N, and O. Zn or Cl could not be detected in the EDX spectrum of the white crystals. Hence, an elemental analysis on H, C, N was also performed on the white crystals. The results of the PGAA measurement of the orange coloured ZnO crystals as compared to those of this analysis of the white crystals are shown in table 1.

Due to the low neutron capture cross section of O (0.19 mbarn [3]), its concentration cannot be determined with reasonable accuracy using PGAA. Besides Zn, significant amounts of H, C, and N were also detected in the sample, synthesised using a molar ratio of 2.3 : 1. Due to the low neutron capture cross section of C (3.5 mbarn [3]) compared to Zn (1.3 barn [4]), the uncertainty of the carbon concentration is greater than is the case for the other elements.

Elements	2.3 : 1 [$\%_{atom}$]	H, C, N analysis of white crystals [$\%_{atom}$]
H	16 ± 5%	32.5 ± 0.6%
C	23 ± 25%	32.3 ± 0.6%
N	16 ± 6%	35.1 ± 0.6%
Zn	44 ± 5%	not measured

Table 1: Comparison of the PGAA measurement of the orange ZnO sample using a molar ratio of 2.3 : 1 and the HCN measurement of the white crystals precipitated during the cooling of the HCl.

Additional organic phase

PGAA, EDX and elemental analysis of H, C, and N all show an organic component in the sample prepared using a molar ratio of 2.3 : 1. The concentrations of H, C, and N determined by these two methods are in acceptable agreement. PGAA is capable of measuring the fraction of the additional elements in the orange ZnO matrix, while for the elemental analysis the precipitated white crystals were used. It is expected that an additional organic phase with similar fractions of H, C, N forms during the harsh reaction conditions of the flame synthesis and is resistant to the high temperatures. A possible compound may be $C_3H_3N_3O_3$, although oxygen could not be quantified. The properties of the additional phase, as well as the origin of the orange colour have not yet been completely solved.

[1] M. Mapa and C. S. Gopinath, Chem. Mater., 21, 351 (2009).

[2] A. Kaschner et al., Appl. Phys. Lett., 80, 1909 (2002).

[3] G. Pfennig et al., Karlsruhe Nuclide Chart, 7th ed. (2006).

[4] G.L. Molnár, Handbook of Prompt Gamma Activation Analysis with Neutron Beams, Kluwer Academic Publishers, (2004).

Highly anisotropic dispersion anomaly of the buckling mode in $YBa_2Cu_3O_7$

M. Raichle[1], D. Reznik[2], D. Lamago[3,4], R. Heid[3], Y. Li[1], M. Bakr[1], C. Ulrich[1], V. Hinkov[1], K. Hradil[5], C.T. Lin[1], B. Keimer[1]

[1]Max Planck Institute for Solid State Research, Stuttgart, Germany

[2]University of Colorado-Boulder, Physics Department, Boulder, USA

[3]Karlsruhe Institute of Technology, Institute for Solid State Physics, Karlsruhe, Germany

[4]Laboratoire Léon Brillouin, CEA-CNRS, CEA-Saclay, Gif-sur-Yvette, France

[5]University of Göttingen, Institute for Physical Chemistry, Göttingen, Germany

Motivated by predictions of a substantial contribution of the "buckling" vibration of the CuO_2 layers to d-wave superconductivity in the cuprates, we performed an inelastic neutron scattering study of this phonon in an array of untwinned crystals of $YBa_2Cu_3O_7$. The data reveal a pronounced softening of the phonon at the in-plane wave vector q = (0, 0.3) connecting nested segments of the Fermi surface upon cooling below ~ 105 K, but no corresponding anomaly at q = (0.3, 0). Based on the observed in-plane anisotropy, we argue that the electron-phonon interaction responsible for this anomaly supports an electronic instability associated with an uniaxial charge-density modulation and does not mediate d-wave superconductivity.

Research on the mechanism of high-temperature superconductivity in the cuprates has recently made substantial progress based on a quantitative analysis of possible Cooper pairing interactions, which include coupling to spin fluctuations and phonons. The spin-fluctuation-mediated pairing interaction favours the experimentally observed d-wave pairing state, but its strength relative to phonon-mediated pairing interactions remains a matter of intense debate. Whereas density functional theory (DFT) indicates a small or negligible contribution of the electron-phonon interaction to d-wave superconductivity, it has been argued that electron correlations can greatly enhance the coupling strength such that it yields a substantial, or even dominant, contribution to the pairing interaction. In this context, we focused on phonons that modulate the Cu-O bonds in the CuO_2 layers, which are generic to all cuprate superconductors. Most model calculations indicate that the electron-phonon interaction of high-energy stretching vibrations of these bonds is either detrimental or indifferent to d-wave pairing. However, several theories indicate that coupling to the lower-energy "buckling" vibration that modulates the Cu-O-Cu bond angle is attractive in the d-wave channel.

Inelastic neutron scattering at PUMA

We used inelastic nuclear neutron scattering to determine the in-plane anisotropy of the self-energy of the buckling mode in a nearly stoichiometric ($\delta \leq 0.05$) and slightly overdoped untwinned specimen of $YBa_2Cu_3O_7$. Our sample consists of 185 individually detwinned single crystals with a total mass of 2.63 g and T_c = 90.0 ± 0.5 K. The measurements were performed on PUMA (FRM II) and 1T (ORPHEE).

The profiles of the buckling mode (E = 40 - 42 meV) exhibit a highly unusual behavior. At 120 K, the profile shows a single peak with a weak shoulder at low energy. Upon cooling, the shoulder grows continuously and draws intensity from the main peak, resulting in a two-wing profile at low temperatures. To parametrize its temperature evolution, we fitted the data as two Gaussians with fixed energies and widths. The fits yield a good description of the data over the entire temperature range (although they do not correctly capture the physics; see below). The temperature dependence of the resulting peak intensities indicates a well-defined onset of the lineshape anomaly at T = 105 ± 15 K [1]. This unusual behaviour is confined to in-plane wave vectors in the range q = (0,0.2) → (0,0.4). The profiles for wave vectors outside this range along the same direction, and for the entire range along the perpendicular direction, q = (0,0) → (0.5,0), are well described by a single, undistorted peak.

Since the E-q range of the anomalous low-temperature dispersion of the buckling mode is comparable to the dimensions of the resolution ellipsoid of the spectrometer, we performed a careful resolution calculation based on the dispersion relation shown in figure 1, which is flat along the a-direction at all temperatures (fig. 1a) and along b for T = 120 K (red line in fig. 1b), but develops a sharp dispersion anomaly along b at lower temperatures (black line in fig. 1b). The profiles calculated yield a good description of the data and provide a simple explanation of the two-wing profile discussed above. The low-energy wing results from the bottom of the dispersion anomaly at the nominal spectrometer setting. However, the instrumental resolution ellipsoid also encompasses a wide segment of the almost flat dispersion surface away from the anomaly, especially in the direction perpendicular to the scattering plane where the q-resolution is poor. This explains the high-energy wing of the profile. A highly anisotropic dispersion anomaly of the buckling mode that is strongly enhanced upon cooling below ~ 105 K thus provides an adequate explanation of all aspects of the data [1].
Although the anomaly is consistent with a sharp onset or enhancement at T_c, its momentum-space structure speaks against a direct relation to the superconducting state. Since 2Δ significantly exceeds the phonon energy along both a- and b-axes, the onset of superconductivity is expected to affect the phonon lineshapes in both directions similarly. Phonon softening along b*, but not along a*, implies that electron-phonon coupling could be strong along b* only. Such uniaxial interaction cannot be responsible for the superconducting gap that is roughly similar along a* and b* [2], and the buckling mode does not contribute in mediating superconductivity beyond q = 0, which translates into a small dimensionless coupling constant ~ 0.02, in agreement with DFT calculations. We conclude that coupling to this mode does not significantly enhance d-wave pairing. It is possible, however, that it contributes to the observed sub-dominant s-wave admixture to the pairing state.
Based on these considerations, an instability other than superconductivity must be directly responsible for the T-dependent anomaly of the buckling mode. The strong in-plane anisotropy of the anomaly indicates that it has a one-dimensional structure, which may arise from an uniaxial charge density wave (CDW) instability. The evidence for a CDW originating in the CuO chains in the $YBa_2Cu_3O_7$ crystal structure, and the wave vector of the phonon anomaly is similar to that of the CDW recently reported by x-ray diffraction. The temperature onset of the phonon anomaly is also near the onset of a pronounced in-plane anisotropy of the Nernst effect in $YBa_2Cu_3O_7$, which has been interpreted as evidence of a stripe or Pomeranchuk instability originating in the CuO_2 planes.
In summary, the highly anisotropic dispersion anomaly of the buckling mode provides evidence of a substantial electron-phonon interaction in $YBa_2Cu_3O_7$, which may contribute to the anomalous band dispersions revealed by ARPES experiments. Rather than contributing to d-wave superconductivity, however, this interaction appears to drive a different instability, presumably associated with a uniaxial charge-density modulation [1].

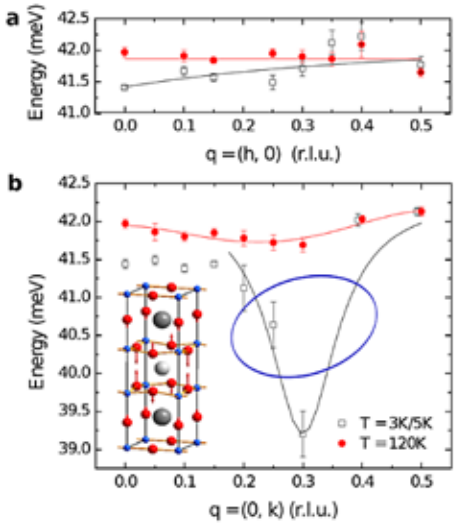

Figure 1: Dispersion of the buckling mode along the a- and b-axes (black line: dispersion used for the resolution calculation). A projection of the four-dimensional resolution ellipsoid is shown for comparison. The inset shows the eigenvector of the buckling mode at q = (0, 0.3). The elongations of the apical oxygen atoms and of the in-plane oxygen atoms along b were enlarged by a factor four for clarity.

[1] M. Raichle et al., Phys. Rev. Lett. 107, 177004 (2011).
[2] M. Bakr et al., Phys. Rev. B, 80, 064505 (2009).

The structural properties of $Sc_{1.1}Fe_{3.9}Al_8$ alloy

K. Rećko[1], L. Dobrzyński[1,2], A. Senyshyn[3], H. Fuess[3]

[1]University of Bialystok, Faculty of Physics, Bialystok, Poland

[2]National Center for Nuclear Research, Otwock-Swierk, Poland

[3]Technische Universität Darmstadt, Institute of Materials Science, Darmstadt, Germany

The nature of the $Sc_{1+\delta}Fe_{4-\delta}Al_8$ intermetallic having a small Sc excess δ = 0.1 was investigated using a neutron powder diffraction technique. The sample crystallizes in a tetragonal $ThMn_{12}$-type structure. The excess of Sc atoms substitutes Fe at the (*8f*) positions and has a pronounced effect on the magnetic properties. The magnetic structure of the alloy forms a double cycloid with magnetic moments rotating according to the incommensurate in-plane wave vector.

Determination of the magnetic properties of the title compound

It is well-known that the intermetallic alloys of actinides or lanthanides with manganese in a ratio 1:12 exhibit, most frequently, $ThMn_{12}$ structure. Moreover, replacement of atoms of manganese by iron and aluminium atoms, whose total atomic concentrations add up to 12, does not change this type of structure. Of all known ternary compounds with the general formula $MFe_{4-\delta}Al_{8+\delta}$ the polycrystalline samples [1-3], as well as the single crystals [4-7] with composition $\delta \approx 0$, have attracted most attention. A number of alloys with $\delta \in (-2; 0.5)$ and M = U, Th, Sc, Y were also studied [8-11].

Description of rather complex magnetic structures of lanthanide and actinide compounds with $ThMn_{12}$-type structure requires the use of two wave vectors and more than one magnetic sublattice. In the well-known compounds MFe_4Al_8 with M = La or Ce [1] and Th [11], despite empty 4f- or 5f-shells in lanthanide and actinide ions, respectively, double cone or double spiral structures were discovered. In the case of double cone systems as in $LaFe_4Al_8$ the magnetic structure is described by the set of two modulation vectors, having $\vec{q}_0 = (0, 0, 0)$ and $\vec{q}_z = (0, 0, -q_{II})$, while in $CeFe_4Al_8$ the presence of vectors $\vec{q}_0$ and $\vec{q}$ with $\vec{q} = (q_\perp, q_\perp, 0)$ is observed. The double spiral described by the set of $\vec{q}$ and $\vec{q}_z$ is also observed in the $ThFe_4Al_8$ alloy. The magnetic structure of YFe_4Al_8 and $ScFe_4Al_8$ is described by a single vector $\vec{q}$, while in the case of UFe_4Al_8 the modulation vector is simply $\vec{q}_0$ [4, 10].

The aim of this experiment was to determine the magnetic properties of the title compound, especially the spin ordering disclosed by neutron diffraction techniques.

Ge monochromator at SPODI used

The neutron powder diffractometer SPODI (fig. 1) was used for magnetic structure determination. The experiment was performed using the (331) reflection of Ge monochromator, with wavelength λ = 2.536 Å, up to 2θ = 151° and step size of 0.05°. The neutron beam used in this experiment contains a small (about 0.5 %) contamination of third order harmonic, λ/3. This contribution was included in the refinement.

The $Sc_{1.1}Fe_{3.9}Al_8$ sample, weighing ~4 g, was obtained by melting the high purity starting elements according to the method described in detail in previous papers [6-9]. The melting itself was carried out in a high purity argon atmosphere. The ingot obtained was next homogenized at 600 °C for 500 hours. After crushing the sample into a powder, prolonged annealing at 550 °C for 2 weeks took place in a protective argon atmosphere.

Magnetic properties dominated by iron moments

In general, the iron atoms occupy (*8f*) positions of the I 4/mmm space group within the $ThMn_{12}$-type structure (see fig. 2). Moreover, in $MFe_{4-\delta}Al_{8+\delta}$ (M = lanthanides and actinides) with $\delta < 0$, the excess Fe atoms locate preferentially

at (*8j*) site. It turns out that similar ordering of iron atoms is observed in isostructural compounds with M = the elements of the III B group of the Periodic Table, namely in yttrium and in scandium alloys [1,3,6-9].
Interpretation of the LT neutron diffraction relies on a simple – single sublattice – magnetic structure. The magnetic properties of the $Sc_{1.1}Fe_{3.9}Al_8$ compound are dominated by the antiferromagnetically oriented iron moments, while scandium represents a non-magnetic component.

Two magnetic transition temperatures

In spite of insignificant precipitates of foreign phases, the sample exhibits well-ordered $ThMn_{12}$ type structure, where Fe atoms occupy solely the (*8f*) site. Excess of Sc atoms occupy the (*8f*) site. The double cycloid system discloses the dominant antiferromagnetic character of Fe-Fe coupling in the basal plane of the tetragonal cell. The canting angle α = 27(3)° at 4 K exists below ~120 K, and the presence of a ferromagnetic component coincides with the irreversibility observed in magnetization processes. In the temperature range up to around 230 K, the magnetic structure is a double cycloid with propagation wave vector $\vec{q} = (q_\perp, q_\perp, 0)$ and $q_\perp$ equal to 0.131(2) for temperatures between 0 and ~160 K. The magnetic moment of iron is of the order of 0.9 μB at 4 K. The Presence of two magnetic transition temperatures, each disappearing at different temperatures, was discovered.

Acknowledgements

This work was partly sponsored by the State Committee of Scientific Research NN 202172335.

Figure 1: Experiments at the structure powder diffractometer SPODI.

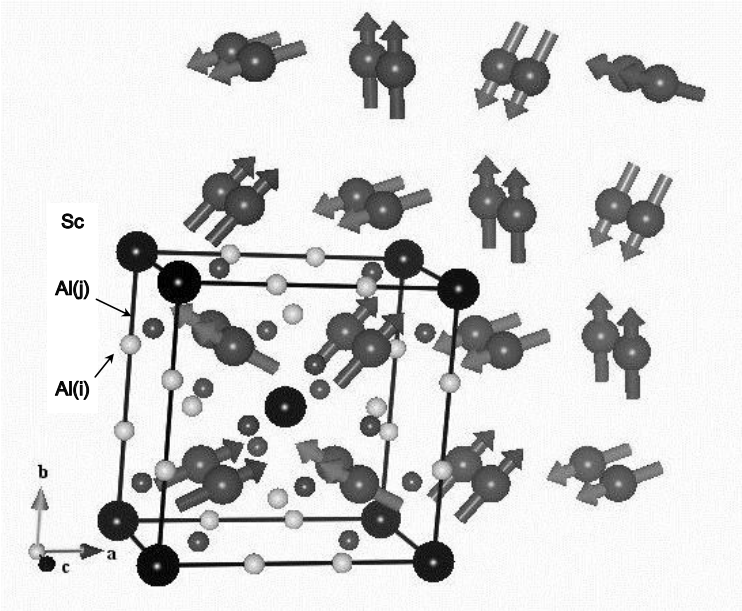

I 4/mmm
Sc – (2a) – (0, 0, 0)
Fe – (8f) – (¼,¼,¼) – magnetic site
Al – (8i) – (x_1, 0, 0), $x_1 \approx 0.34$
Al – (8j) – (x_2, ½, 0), $x_2 \approx 0.28$

Figure 2: Body centred tetragonal unit cell of $Sc_{1+\delta}Fe_{4-\delta}Al_8$ with the lattice parameters equal to a = 8.630(2) Å and c = 5.004(2) Å at 4 K. The symmetry containing four non-equivalent lattice sites in Wyckoff notation of space group no. 139. Long range magnetic order leads to double cycloid structure with incommensurate modulation wave vector $\vec{q} = (q_\perp, q_\perp, 0)$.

[1] P. Schobinger-Papamantellos et al, J. Magn. Magn. Mater., 186, 21 (1998).
[2] P. Schobinger-Papamantellos et al., J. Magn. Magn. Mater., 202, 410 (1999).
[3] G.M. Kalvius et al., Hyp. Interact., 151-152, 195 and references therein (2003).
[4] J.A. Paixão et al., Phys. Rev. B, 55, 14370 (1997).
[5] J.A. Paixão et al., Phys. Rev. B, 63, 054410 and references therein (2001).
[6] H. Misiorek et al., J. Alloys Compd., 363, 81 (2004).
[7] V.M. Dmitriev et al., Phys. Stat. Sol. (c), 1, 1824 (2004).
[8] A.M. Gurevich et al., Low Temp. Phys., 27, 967 (2001).
[9] K. Rećko et al., Phase Transit., 80, 575 and references therein (2007).
[10] K. Szymański et al., J. Phys.: Cond. Matter, 11, 6451 (1999).
[11] K. Rećko et al., Phys. Stat. Sol. (a), 196, 344 (2003).

Phase transition and structure analysis of the polycrystalline Dy_2CuIn_3

I. M. Siouris[1], R. K. Kremer[2], M. Hoelzel[3]

[1]Democritus University of Thrace, Production and Management Engineering Department, Materials Laboratory, Xanthi, Greece

[2]Max-Planck-Institut für Festkörperforschung, Stuttgart, Germany

[3]Technische Universität München, Forschungs-Neutronenquelle Heinz Maier-Leibnitz (FRM II), Garching, Germany

The nuclear and magnetic structure of Dy_2CuIn_3 was investigated using neutron diffraction. Susceptibility measurements indicate an onset of antiferromagnetic ordering at 19.5 K and a divergence below 9 K; however, ferromagnetic correlations are present below 35 K. Neutron diffraction confirms the antiferromagnetic transition at 19.5 K. The magnetic ordering can be described by a propagation vector k = (0.25,0.25,0) with a magnetic moment $\mu = 2.63\ \mu_B$ parallel to the c-axis. No additional magnetic phase transition was observed around 9 K, suggesting a spin glass state in coexistence with the antiferromagnetic mode as a result of frustration and antagonism between ferromagnetic and antiferromagnetic interactions.

Magnetic properties of R_2CuIn_3 compositions

The crystallization of ternary intermetallic compounds, synthesised from a rare earth (R) transition metal and an element of the IIIA group of the periodic table into the hexagonal 'binary-type' structures of AlB_2 and its variants, often leads to a state of structural disorder, which is imposed by the statistical occupation of the network by two different non-magnetic atoms, known as non-magnetic atom disorder (NMAD). The magnetic properties of these compounds are assumed to be dominated by frustration originating from competing ferro- and antiferromagnetic exchange which is related to the triangular topology of the R ions as well as to the specific disorder.

The hexagonal R_2CuIn_3 compositions have served as test beds to study the effect of NMAD on the exchange mechanism by probing the magnetic properties, both macroscopically for R = (Ce, Nd, Pr, Gd, Dy, Tb, Ho, Er) and microscopically for R = (Tb, Ho, Er). Although the magnetization measurements indicate a complex antiferromagnetic behaviour, this has, so far, been confirmed by neutron diffraction only for the Tb_2CuIn_3, which is a collinear antiferromagnet with $T_N = 33$ K [1-4] in coexistence with a spin-glass-like state. The macroscopically measured magnetic behaviour of the Dy_2CuIn_3 compound is that of an antiferomagnet with $T_N = 20\ (\pm 1)$ K. Upon lowering the temperature, different spin states emerge from 9 to 6 K, which are dominated by ferromagnetic correlations. Furthermore, susceptibility measurements showed a clear frequency dependent susceptibility which indicates that a glassy state forms below this temperature. The aim of the present investigation was to a) determine the structural parameters of the compound at room temperature (RT), b) establish the ordering temperature and c) probe the magnetic structure at low temperatures down to 4 K.

Experimental details and method of analysis

Several polycrystalline Dy_2CuIn_3 samples of total weight ~7 g were prepared by arc melting a stoichiometric mixture of high purity starting elements in titanium-gettered Ar atmosphere. To ensure homogeneity, each of the prepared buttons was flipped over and re-melted several times. The ingots were wrapped in titanium foil, sealed in an evacuated quartz glass ampoule and annealed at 750 °C for 30 days. The weight losses of both compounds did not exceed 1 wt.%. Neutron diffraction experiments were performed at the high-resolution powder diffractometer SPODI at an incident neutron wavelength $\lambda = 2.396$ Å. The pulverized Dy_2CuIn_3 sample (~7 g) was filled into a vanadium container of 7.6 mm diameter and inserted into a closed–cycle helium refrigerator

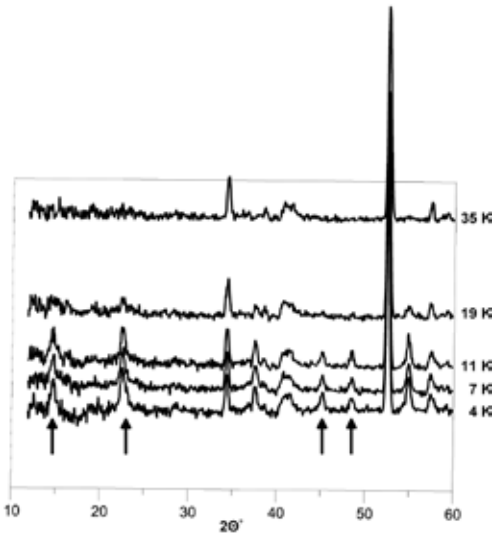

Figure 1: Low angle regions of diffraction patterns measured at various temperatures, showing the development of weak magnetic reflections below 19 K.

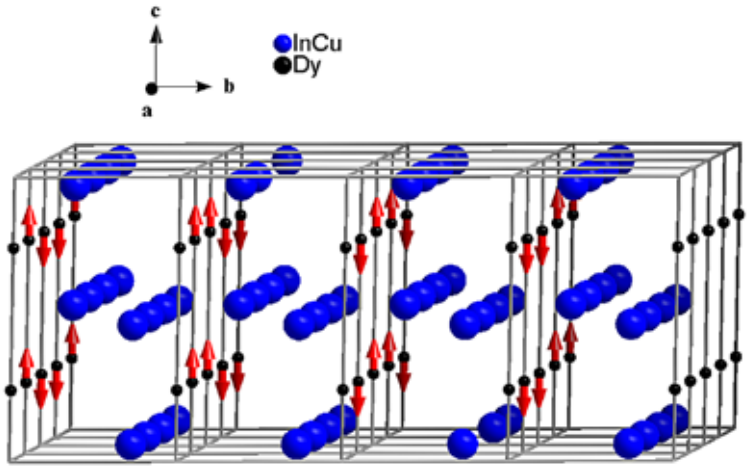

Figure 2: The magnetic unit cell of Dy_2CuIn_3 at 4 K.

cryostat. Neutron diffraction patterns were recorded at RT and 4 K for 13 h each. In addition, diffraction data were collected at various temperatures between 4 K and 35 K, for 10 h each. The experimental data analysis was performed by incorporating both full pattern Rietveld refinements using the program FULLPROF and integrated intensity refinements with the least squares programme AMPHOREA which is designed to reveal reasonable standard deviations of the refined structure parameters.

Structure and magnetic order of Dy_2CuIn_3

The neutron diffraction patterns collected at RT and 25 K show neither variations in intensity of the Bragg peaks nor any extra reflection of magnetic origin. Thus, the ordering temperature should be lower than 25 K. The crystal structure of the compound has been refined from the RT diffraction pattern. All nuclear peaks in the diagram could be indexed within the hexagonal $CaIn_2$-type structure model of space group $P6_3/mmc$. The final refinement calculations for the Dy_2CuIn_3 crystal structure were based on 21 Bragg peaks. The free atomic positional parameters were refined to: Dy atoms at 2b site (0,0,0.25) and the Cu/In atoms statistically distributed over the 4f site (0.33333, 0.6667, 0.04011(4)). The lattice parameters are a = 4.6919(2) Å and c = 7.2743(2) Å. The unit cell contains one formula unit and the reliability factor was determined to be R_{Bragg} = 6.7 %. By following the integrated intensities of various magnetic peaks as a function of temperature, the Neél temperature T_N = 19 ± 1 K is confirmed (fig. 1). The magnetic order can be described by a propagation vector k = (0.25,0.25,0) with the μ = 2.63 μ_B/Dy^{3+} at 4 K aligned parallel to the c-axis (fig. 2). The overall R-value of the refinement is 8.8 %.

Spin glass and antiferromagnetic states coexist

During this investigation, the structural parameters of the compound were refined, the antiferromagnetic structure at lower temperatures was resolved and the ordering temperature determined. However, no additional phase transitions were observed, in contrast to the magnetisation measurements. These results assume that a geometrical frustration causes the formation of coexisting spin glass and antiferromagnetic states.

[1] I.M. Siouris et al., J. Alloys Compd., 297 (1-2), 26 (2000).
[2] I.M. Siouris et al., J. Alloys Compd., 314 (1-2), 1 (2001).
[3] I.M. Siouris et al., J. Magn. Magn. Mater., 226-230 (Part 2), 1128 (2001).
[4] A. Szytuła et al., Solid State Commun., 147 (1-2), 61 (2008).

Vertical correlation of domains due to non-collinear and out-of-plane exchange coupling

A. Paul[1] and S. Mattauch[2]

[1]Technische Universität München, Physik Department E21, Garching, Germany

[2]Forschungszentrum Jülich GmbH, Jülich Centre for Neutron Science at FRM II, Garching, Germany

Conventionally, magnetization is probed along the plane of the exchange biased direction in exchange coupled ferromagnet-antiferromagnetic systems. Here we opt for out-of-plane biasing on a system with strong in-plane anisotropy and measure its magnetization along the film-plane using neutron scattering. We show that competing anisotropic directions, thereby induced, not only can change the magnetization behavior in our system but also can effectively bring in magnetic correlation of domains (in-plane and out-of-plane). It should be noted that these domains were vertically uncorrelated for a conventional (in-plane unidirectional anisotropic) case.

Exchange bias and non-collinearity

In conventional exchange coupled antiferromagnet (AF) -ferromagnet (FM) systems, the cooling field is applied in the film plane along a certain direction and this direction normally (almost) coincides with the AF anisotropy axis as well [1]. Apart from the conventional case, there have been reports of a possibility that the easy axis of the FM and that of the AF are not parallel, i.e. they may remain non-collinear.

In the case of polycrystalline layers, one can assume randomly oriented grains (e.g. CoO) with uniaxial anisotropy. An out-of-plane field cooling, below the ordering temperature, can orient the local anisotropy axis out of plane. The aim of this work is therefore to explore (unconventionally) the option of realizing out-of-plane exchange coupling in a system with in-plane anisotropy.

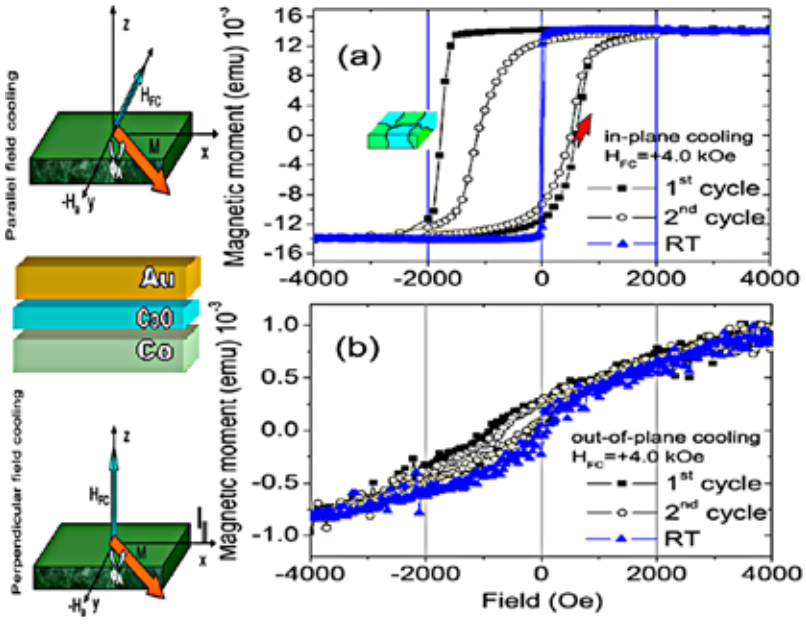

Figure 1: SQUID hysteresis loops of [Co/CoO/Au] multilayer during the 1st and 2nd field cycles for field cooling a) along the sample plane and b) perpendicular to the sample plane.

Neutron scattering experiments at TREFF

We have investigated multilayers of the composition SiO_2/[Co(11.0 nm)/CoO(5.0 nm)/Au(22.5 nm)] x 16. The uncompensated AF spins are frozen-in by the exchange field of the FM moments as large enough fields align the FM moments along a direction perpendicular to the film plane. This establishes or induces the exchange bias direction. The AF spins, on the other hand, deviate from the initial cooling field direction toward their closest in-plane easy axis (cubic anisotropy) once AF order sets in and remain so also during measurements along an in-plane direction. The neutron scattering experiments were performed at the polarized neutron reflectometer with polarization analysis TREFF at the FRM II for a wavelength of 4.73 Å. All measurements were done (in-plane) after the sample had been cooled to 10 K from room temperature by a continuous flow cryostat in the presence of a cooling field (perpendicular to the sample plane) provided by an electromagnet.

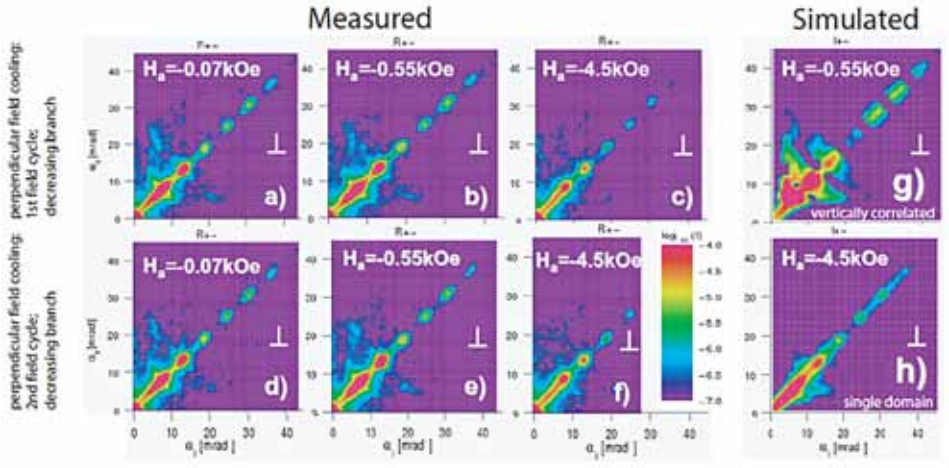

Figure 2: SF intensity maps [R– +] from [Co/CoO/Au] multilayer measured at perpendicular field cooling and measured along (a–c) the first half of the first field cycle or the decreasing branch and along (d–f) the first half of the second field cycle. The corresponding simulated intensity maps are shown alongside (g, h) . The colour bar encodes the scattered intensity on a logarithmic scale.

Unconventional biasing direction

We present in figure 1(a) the hysteresis loops for an in-plane cooling field representing the conventional case of in-plane longitudinal (along the applied magnetic field) magnetization measurements. Similar measurements for out-of-plane cooling are presented in figure 1(b). Unlike the in-plane case, the loops corresponding to the first and second field cycles for the out-of-plane case are similar. This indicates a similar symmetric magnetization reversal mechanism. The exchange bias field along the cooling field axis for such an out-of-field cooling is estimated to be around –500 Oe as compared to –600 Oe for in-plane cooling.

Next we show the intensity maps (off-specular and specular SF scattering signals) in figure 2(a) - (f) for perpendicular field cooling (along the decreasing branch of the hysteresis loop corresponding to the 1st and 2nd field cycles). The intensity along the diagonal $\alpha_i = \alpha_f$ is the specular reflection along the perpendicular momentum transfer vector Q. These maps are also simulated within the distorted wave Born approximation DWBA [2].

The most interesting feature is perhaps the fact that there has been a vertical correlation of FM domains (lateral sizes are ~ 10 microns at remanence and around the reversal point) plausibly induced by the perpendicular field cooling. Typical signatures of vertically correlated domains can be seen as diffuse streaks along the Q parallel, at the positions of the Bragg peaks in figures 2(a, b, d, e). It should be noted that these diffuse streaks in the SF channels disappear at higher fields (–4.5 kOe). This clearly indicates that they are exclusively of magnetic origin and thus the magnetic correlation is established. It should be noted that these vertical correlations are clearly different from the domains that we generally observe after parallel field cooling [3]. For parallel field cooling, they remain vertically uncorrelated.

Correlations due to non-collinear coupling

Demagnetization results from the formation and motion of domain walls in the soft layer. In exchange biased spin valves, repeated cycling results in the loss of magnetic memory. Thus, in order to achieve stability in the device structure, it is necessary to get rid of the non-uniform reversal (associated with the so-called asymmetry in magnetization reversal) ensuring reversal via coherent rotation. We have shown that symmetric coherent rotation without any microscopic training can be achieved. This can be realized by inducing an exchange bias by coupling the uncompensated AF moments either with a remanent state of the FM magnetization [1] (in the case of in-plane biased structures) or with the FM moments along a direction perpendicular to the AF axis (in the case of out-of-plane biased structure) [2]. The realization of perpendicular exchange bias and perpendicular anisotropic nano-structures with magnetic correlations has far-reaching implications for ultrahigh density perpendicular recording media development.

[1] A. Paul and S. Mattauch, Appl. Phys. Lett., 95 (9), 092502 (2009).

[2] A. Paul et al., New Journ. Phys., 13 (6), 063008 (2011).

[3] A. Paul, Appl. Phys. Lett., 97 (3), 032505 (2010).

View into the reactor pool
while removing the fuel element at the end of a cycle.

Reactor & Industry

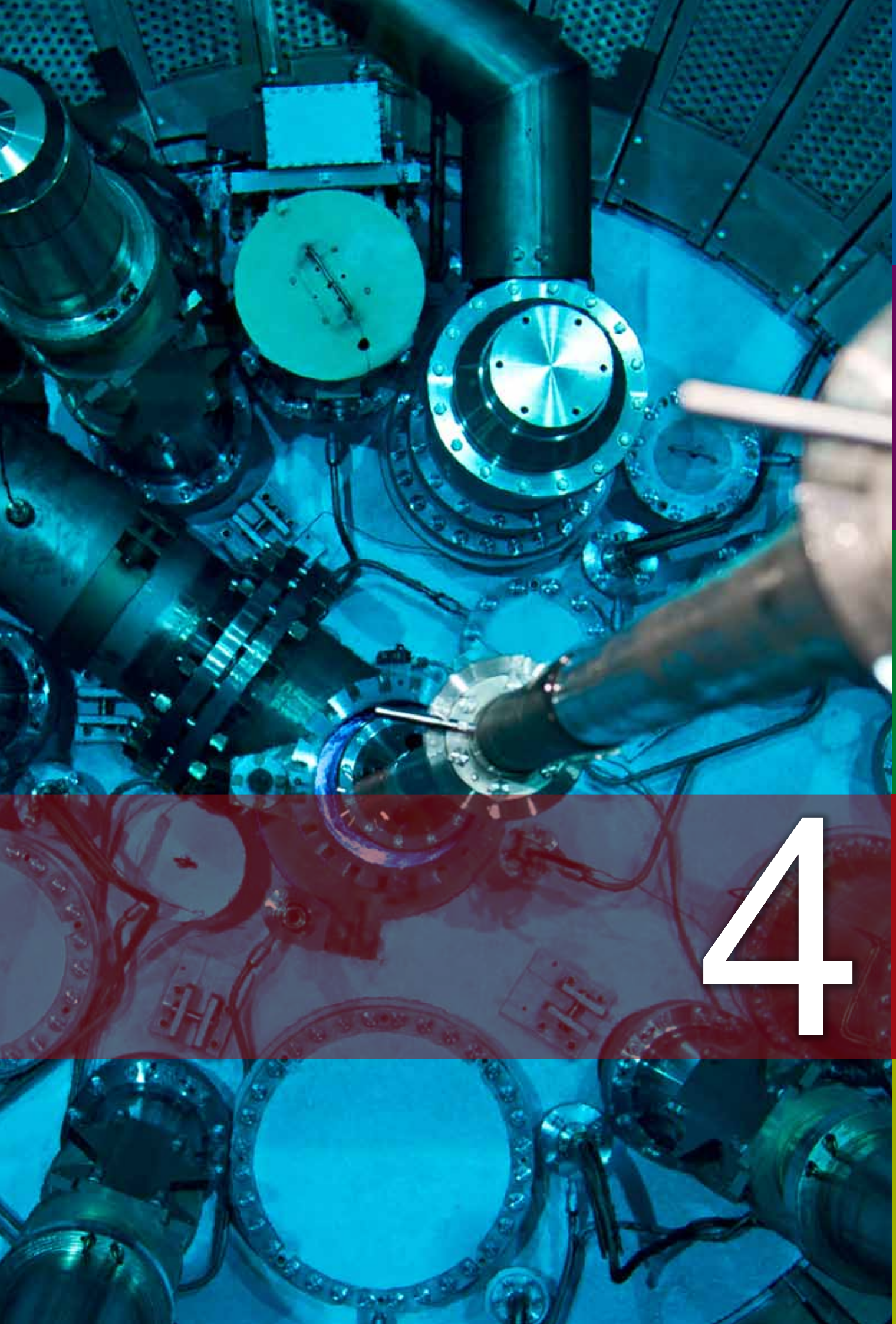

4

The operation of the neutron source in 2011

A. Kastenmüller

Technische Universität München, Forschungs-Neutronenquelle Heinz Maier-Leibnitz (FRM II), Garching, Germany

In 2011 the operation of the FRM II was governed by an extensive maintenance break. This shutdown period, that was intended to facilitate the replacement of the beam tube SR11 of the positron source NEPOMUC, also made it possible to install the new thimble for the future production facility of molybdenum-99 and other maintenance activities. The catastrophic earthquake in Japan and the nuclear accident in Fukushima also lead to extensive safety assessments and inspections of German nuclear facilities, including the FRM II. On completion of all maintenance work, the reactor was prepared for the start-up which took place in the beginning of October 2011. The temperature level in the experimental tube of the new positron source exceeded the tolerable value for continuous operation causing an additional interruption in the reactor operation. After dismounting the inner parts of the positron source, the start-up procedures to the nominal power of 20 MW were completed successfully. Therefore, in 2011, one reactor cycle with a total of 60 days was performed and the fuel element used to its maximum licensed burnup of 1200 MWd.

Figure 1: Shearing of the old NEPOMUC experimental tube in the hot cell facility.

Long maintenance break

The first nine months of the year 2011 were characterized by the major maintenance break that had started in October 2010. Besides extensive maintenance activities, the moderator tank was completely drained and dried for the first time since the nuclear start-up of the FRM II in 2004. This was necessary prior to opening the tank in order to replace the beam tube SR11, including the experimental tube of the positron source NEPOMUC (fig. 1), and to install the new thimble for the production facility of molybdenum-99. The latter is the parent radioisotope of the short-lived gamma-emitting radioisotope technetium-99m, the most important isotope for medical diagnosis and treatments.

Fukushima and its consequences for the FRM II

Due to the severe earthquake in Japan and the accident in the Fukushima Daiichi nuclear power plant in March 2011, international inquiries regarding the safety of nuclear power plants were carried out. In Germany too, there were extensive safety assessments and special inspections of nuclear facilities. Although the high-flux neutron source FRM II is in many ways not comparable to a nuclear power plant, the Bavarian regulatory body performed a special inspection program shortly after the events in Japan. Additionally, the German reactor safety commission (RSK) developed a questionnaire for safety assessments not only of all German power plants, but also of German neutron sources such as the FRM II. Furthermore, special checkups were performed on-site. As the FRM II is a very new facility, all questions and requests for documentation were able to be answered on time. The requested file of more than 600 pages was submitted to the authority at the end of October 2011. The as-

sessment is still ongoing, however the analysis of the extensive questioning already revealed that the FRM II, as newest and most modern German neutron source, has a robust safety concept and meets all the safety requirements.

Successful operation of cycle no. 26

After completion of the manifold replacement, e.g. of heat exchangers between the secondary and tertiary cooling circuits (fig. 2), servicing and maintenance work (fig. 3), in September 2011, the moderator tank was refilled with heavy water in order to commence the operation of the neutron source again. Due to the new mounted components, some nuclear commissioning steps had to be performed. The start-up of the neutron source was planned for the beginning of October. However, the step-wise increase in the reactor power was only possible up to 10 MW. Then, the reactor had to be shut down as an inner part of the positron source in the beam tube SR11 reached a temperature level that did not permit a permanent continued operation at 10 MW nor a further increase in thermal power. The experimental tube was pulled out from the beam tube which was then closed with a black flange. For radiological reasons, this measure required the unloading of the fuel element.

Finally, on October 28, after remounting the shielding blocks at SR11 and the loading of the fuel element, the reactor start-up was performed again. From October 29 2011 until the scheduled end of cycle on December 27 2011 the reactor was operated at nominal power of 20 MW. The operating cycle No. 26 in 2011 was executed safely with a total of 60 days of operation up to a fuel burnup of 1200 MWd.

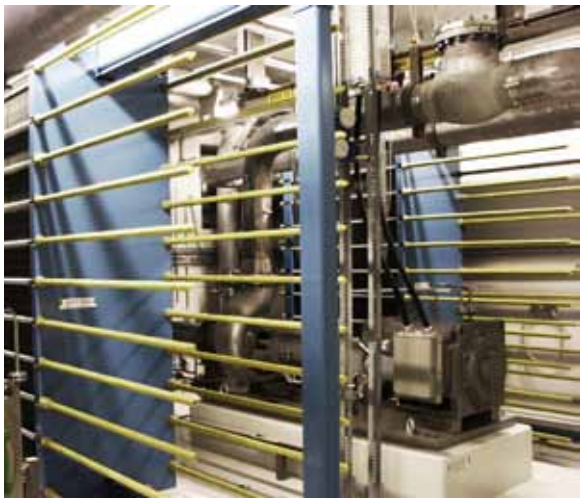

Figure 2: New heat exchangers between the secondary and tertiary cooling circuits.

Figure 3: Maintenance work in the primary cooling circuit room.

Meeting highest safety standards at the FRM II

In 2011, a total of 1804 recurring checkups, service inspections by independent experts from the regulatory body covering 18 different areas and 66 documented modifications were performed in order to guarantee or to improve the high safety- and facility-related standards of the FRM II.

There was one reportable incident. During a planned routine check of two valves in the heavy water system, signs of corrosion were detected on bushings in these fittings. The bushings were replaced by improved parts made of a corrosion resistant alloy. This incident was in the lowest category N (= normal) in February 2011, which was reported to the authority, the State Ministry for Environment and Health. At the INES (International Nuclear Event Scale) this incident was rated at the level 0, i.e. below-scale events. There was no effect on the safety of the neutron source, the staff or the environment. No radioactivity was released.

Heavy ion irradiation of UMo/Al samples with protective Si and ZrN layers

R. Jungwirth[1], T. Zweifel[1], H.-Y. Chiang[1], W. Petry[1], S. Van den Berghe[2], A. Leenaers[2]

[1]Technische Universität München, Forschungs-Neutronenquelle Heinz Maier-Leibnitz (FRM II), Garching, Germany

[2]Studiecentrum voor Kernenergie, Nuclear Materials Science Institute, Mol, Belgium

Disperse UMo/Al samples produced with UMo powder coated with Si and ZrN have been examined before and after irradiation with iodine at 80 MeV. During heavy ion irradiation no UMo/Al interdiffusion occurred at spots that were protected by a sufficiently thick Si layer or a dense ZrN layer. In contrast, a conventional UMo/Al interdiffusion layer (IDL) occurred at spots where the UMo has not been protected by a Si layer or where the ZrN layer was broken.

UMo/Al-based fuels for reasearch reactors

The development of new UMo based disperse high-density fuels for research and test reactors worldwide has been retarded by unforeseeable high swelling of test fuel plates during in-pile irradiation. The main cause for the swelling is the build-up of an interaction layer at the interface between the UMo and the Al.

It is known that the addition of some wt% Si to the Al matrix results in the formation of a silicon rich layer (SiRL) at the interface between the UMo and the Al. This SiRL forms during annealing in the course of fuel plate production [1]. It retards the conventional UMo/Al interdiffusion during irradiation and therefore enhances the in-pile performance [2]. However, a conventional UMo/Al interaction layer occurs as soon as the SiRL has been completely consumed [3]. Since not all the Si added to the Al matrix is used to form the protective SiRL it has been suggested to apply the silicon directly where it is needed: at the interface between the UMo and the Al, thereby maximizing the availability of Si in the diffusion process [4]. Another possibility to reduce the UMo/Al interaction is the application of a ZrN diffusion barrier [5]. Both coatings were applied by sputter deposition [6].

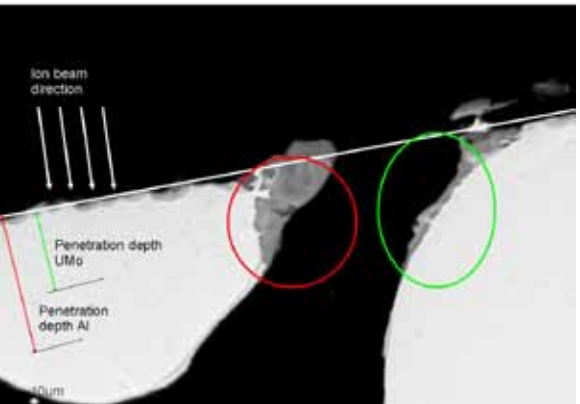

Figure 1: Cross section through the irradiated surface of the sample with 300 nm Si coating. In case of a sufficiently thick coating (green) no UMo/Al interaction occurs. Otherwise (red), a conventional IDL forms during irradiation.

Irradiation of disperse UMo/Al samples

Disperse UMo/Al samples prepared with the coated powder have been irradiated out-of-pile using iodine at 80 MeV until an integral fluency of 1 x 10^{17} ions/cm² has been reached. Such irradiation conditions create similar effects inside the samples like considerable in-pile burn-up [6]. After irradiation the samples were sectioned through the irradiated area and SEM/EDX analyses have been carried out on the cross section.

Sample state before and after irradiation

In the case of 300 nm and 600 nm Si deposited on the UMo grains a SiRL containing also some U and Al developed around the UMo particles during plate production. In case of 300 nm Si, the SiRL layer is very thin (< 1 µm) and the Si agglomerated, i.e. the UMo particles are often not entirely protected.

In case of 600 nm Si sputtered on the UMo the SiRL is present around every UMo particle at any position, i.e. almost all UMo particles are covered with a dense SiRL. Its thickness is in general 1 - 2 µm. The ZrN layer is present at almost every position around the UMo particles. Its thickness is ~1 µm, in accordance with the production parameters. No reaction between the ZrN and the UMo or the Al occurred during the plate production process. The ZrN layer frequently reveals cracks with a diameter below ~100 nm that have not been found on the coated powder before plate processing.

A cross section through the 300 nm Si sample after irradiation is shown in figure 1. In case the UMo particle was not protected by a SiRL or the SiRL was too thin a conventional UMo/Al diffusion occurred. In this case, no Si has been detected inside the IDL by EDX analysis. In case the SiRL was sufficiently thick, the formation of an UMo/Al interdiffusion layer has been completely suppressed. Instead the SiRL has been attacked by diffusion as can be seen from the change in gray contrast. Thereby, the Si content inside the SiRL has been decreased from 20 at% to < 10 at%. At most spots the SiRL was not sufficiently thick to prevent the formation of an IDL during sample irradiation.

Figure 2 shows a cross section through the 600 nm Si sample after irradiation. Since most positions were protected by a SiRL, no UMo/Al diffusion occurred during the irradiation. However, the SiRL itself is affected by diffusion as can be seen by the gray contrast. The Si content inside the layer is reduced from ~40 at% before irradiation to ~ 20 at% after irradiation.

The behavior of the 1000 nm ZrN sample after irradiation is shown in figure 3. In case a non-cracked ZrN layer is present around the UMo, the formation of an IDL is completely suppressed. Furthermore, the ZrN layer is not affected by any diffusion. Figure 3b shows the case where the ZrN layer was cracked. A huge UMo/Al diffusion occurred that even dislocated parts of the ZrN layer. In contrast, the UMo/Al diffusion has been completely suppressed at positions where the ZrN layer was dense. Since the ZrN layer was cracked at most positions, figure 3b is representative for the general behavior of the sample during ion irradiation.

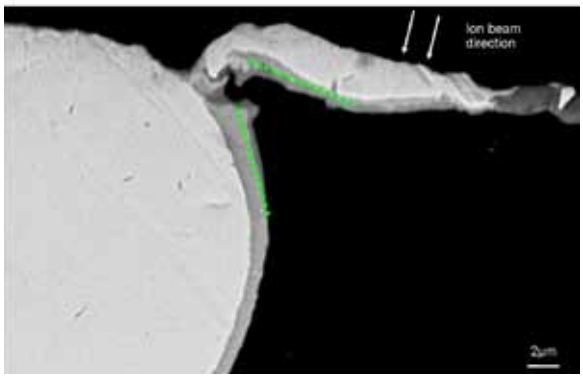

Figure 2: Cross section through the irradiated surface of the sample with 600 nm Si coating. The SiRL is in general sufficiently thick to prevent any UMo/Al interaction. However, the SiRL is attacked during irradiation by Al diffusion, which can be seen by differing gray values (green dotted line).

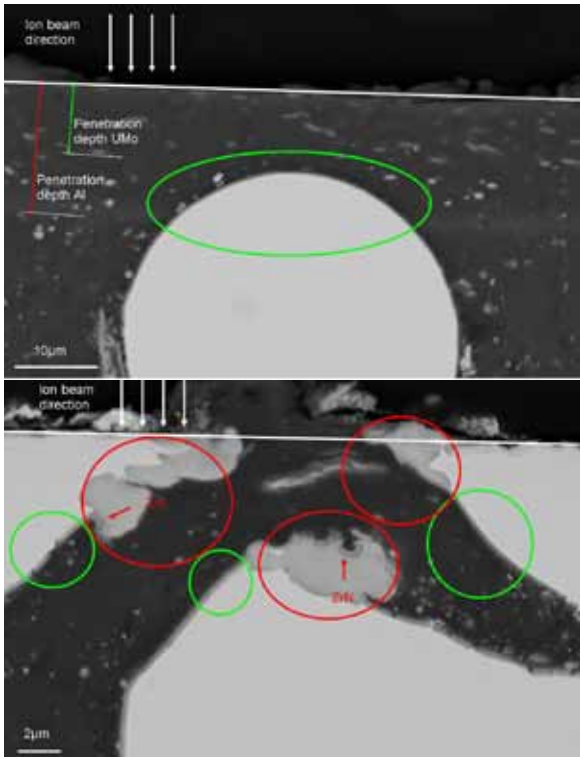

Figure 3: UMo particles covered with 1000 nm ZrN after irradiation. In case of a dense ZrN layer (green circles) the UMo/Al diffusion has been completely suppressed. In case of a cracked ZrN layer a huge IDL has grown along the cracks.

Suppression of IDL formation

Samples from plates prepared with UMo powder coated with 300 nm Si, 600 nm Si and 1000 nm ZrN have been examined before and after irradiation with heavy ions.

In case of Si covered UMo, the Si layer has been transformed into a SiRL during plate processing. For ZrN, almost all UMo particles are covered by a ZrN layer. However, the layer usually reveals cracks that have been introduced during plate fabrication.

A sufficiently thick SiRL – what is the case for 600 nm Si – or a dense ZrN layer around the UMo completely suppressed the formation of an IDL during irradiation. However, the presence of cracks inside the ZrN layer is still a clear drawback.

[1] X. Iltis et al., RERTR 2010, Lisbon (2010).
[2] D.D. Keiser, et al., J. Nucl. Mater, 393 (1), 311 (2009).
[3] R. Jungwirth et al., RERTR 2009, Bejing (2009).
[4] A.L. Izhutov et al., RERTR 2010, Lisbon (2010).
[5] N. Wieschalla et al., J. Nucl. Mater, 357 (1-3), 191 (2006).
[6] S. Van den Berghe et al., RRFM 2011, Rome (2011).

Boron concentration measurements in small organic samples using the PGAA facility

T. Schmitz[1], P. Kudejova[2], C. Schütz[1], J.V. Kratz[1], P. Langguth[3], G. Otto[4], G. Hampel[1]

[1]University of Mainz, Institute for Nuclear Chemistry, Mainz, Germany

[2]Technische Universität München, Forschungs-Neutronenquelle Heinz Maier-Leibnitz (FRM II), Garching, Germany

[3]University of Mainz, Department of Pharmacy and Toxicology, Mainz, Germany

[4]University of Mainz, Department of Hepatobiliary, Pancreatic and Transplantation Surgery, Mainz, Germany

Organic specimens, obtained from patients in clinical trials or from *in vivo* experiments, are usually limited to weights below 100 mg. In a project at the University of Mainz, boron concentrations below 30 ppm had to be determined using such small samples. Tissue samples were measured at the Prompt Gamma Activation Analysis facility (PGAA) at the FRM II and the concentration of boron was determined. In interpreting the results, the peak area obtained was determined using an internal standard method, while a deconvolution of overlaying peaks with the boron peak was necessary. The concentrations determined are in good agreement with the results of other techniques.

At the University of Mainz, the possibilities of Boron Neutron Capture Therapy (BNCT) are investigated in basic research projects in various topics [1,2]. BNCT is based on enrichment of the boron isotope ^{10}B in tumor cells and the neutron capture reaction of this isotope. The subsequent disintegration of the boron nucleus leads to an alpha particle and a lithium ion. These particles slow down at a pace comparable to a cell dimension so that their energy is able to kill the tumour cells.

Currently, BNCT is applied in phase I and II clinical trials in Finland, Japan and Taiwan, mainly to patients with glioblastoma multiforme, head and neck cancer and malignant melanoma. In 2001 and 2003, two attempts to cure liver cancer using auto-transplantation were also made by a group at the University of Pavia, Italy. In the wake of their experiences, one aim of the group in Mainz is to apply the treatment of liver metastasis in the TRIGA Mark II research reactor of the University of Mainz.

In an on-going preclinical trial at the University Hospital Mainz on colorectal carcinoma patients with liver metastases [2], the boron uptake behaviour is investigated. To protect patients from toxicity effects, in the first stage only low concentrations of boron are used, which are sufficient for pharmacokinetic studies.

Prompt gamma activation analysis has been used successfully in boron detection for a long time. The present contribution describes the measurement of small tissue samples using the PGAA facility at the FRM II, which is well established in trace element analysis [3].

Liver tissue collected after boron infusion

The measured tissue samples were collected in a preclinical trial: Patients undergo a partial liver resection because of liver metastases resulting from colorectal carcinoma. The only difference from normal course of surgery is a two hour infusion of boronphenylalanine (BPA) prior to resection. 200 mg/kg bodyweight of the drug are administered during infusion. After the resection surgery continues normally.

Samples of the resected part of the liver are taken before and after perfusion of the liver lobe, using preservation solution. This perfusion would be mandatory in a possible treatment and is therefore an adequate simulation. The samples are taken to investigate washout effects. In general, tissue is taken from malignant and non-malignant parts of the liver. Tumour tissue is very heterogeneous and, in order to differentiate between necrosis, tumour, fibrosis and tumour-free areas, an analytical technique with spatial resolution and additional histological information is needed. Therefore, via PGAA only the homogeneous tumour-free tissue is analysed. In total, 17 samples of four different patients were

measured. Their weight was between 44 mg and 315 mg, with an average of 161 mg.

A detailed description of the PGAA facility is given in [3]. For the measurements described here the neutron flux at the sample position has been adjusted to $8.3 \cdot 10^8$ n cm^{-2} s^{-1}. The irradiation of each specimen took two hours. For the purpose of analysis, the peak areas of the Doppler broadened 478 keV boron peak and the 2223 keV hydrogen peak were determined via Hypemet-PC. For concentrations below 10 ppm a fitting function according to [4] was used. Tissue contains reasonable amounts of sodium. Sodium is also activated by neutrons and leads to a signal at 472 keV, which overlies the broad boron peak. Therefore, a precise deconvolution by fitting the boron-peak region was necessary. Since the total mass of the sample irradiated by the neutrons was not known, the hydrogen peak area in the spectrum was used as an "internal standard" to determine the boron concentration. The necessary hydrogen concentration information was taken from [5] and verified via combustion analysis. Given this information, the boron concentration was derived from a simple comparison of the amount of hydrogen and boron in the sample.

Metabolic cell activities influence concentration

Table 1 shows the measured boron concentration in each sample. The uncertainty has been determined to be about 5 %, using the combined uncertainty of the spectra and the calibration curve. The table also gives the average value for each patient, the corresponding standard deviation, and information about the time of sampling. The measured tissue concentrations are between 14.7 ppm and 7.4 ppm.

The difference in the concentrations between the patients is possibly a result of different metabolic cell activities, due to, for example, a fatty liver disease. The values measured have been verified at the PGAA facility at the High Flux Reactor of the European Commission in Petten, the Netherlands, as reported in [6], and via quantitative neutron capture radiography [2].

Patient No.	Tissue Sample No.	Time of sampling*	Boron concentration	Average concentration**	St. dev.**
1	1	b.p.	12.5 ppm	9.0	0.1
	2	a.p.	9.1 ppm		
	3	a.p.	8.9 ppm		
2	4	a.p.	14.7 ppm	12.0	2.4
	5	a.p.	10.9 ppm		
	6	a.p.	10.4 ppm		
3	7	a.p.	10.4 ppm	9.8	2.5
	8	a.p.	8.5 ppm		
	9	a.p.	12.4 ppm		
	10	a.p.	10.4 ppm		
	11	a.p.	7.4 ppm		
4	12	b.p.	11.1 ppm	8.4	0.4
	13	a.p.	8.7 ppm		
	14	a.p.	9.0 ppm		
	15	a.p.	8.1 ppm		
	16	a.p.	8.3 ppm		
	17	a.p.	8.3 ppm		

Table 1: Measured boron concentration in each sample.
* b.p. – before perfusion; a.p. – after perfusion
** excluding the samples taken before perfusion

In vivo experiments planned

The advantage of the PGAA method described here is the good reproducibility, high analysis speed and reliability. No sample preparation is needed and the sample can be used in other analysis techniques subsequently. The PGAA facility at the FRM II is capable of precise measurements of low boron concentration in samples around and below 100 mg weight.

In future the facility will therefore also be used in the measurement of specimens from *in vivo* experiments. The organs obtained from nude mice, for example, do not often exceed a weight of 100 mg. Therefore, the PGAA facility also promises to be a viable method for these samples.

[1] T. Schmitz et al., Acta Oncol., 50, 817 (2011).
[2] C. Schütz et al., Radiat. Res., 176, 388 (2011).
[3] L. Canella et al., Nucl. Instrum. Meth. A, 636, 108 (2011).
[4] M. Magara and C.Yonezawa, Nucl. Instrum. Meth. A, 411, 130 (1998).
[5] International Commission on Radiation Units and Measurements, Photon, Electron, Proton and Neutron Interaction Data for Body Tissues. ICRU Report, 46 (1992).
[6] T. Schmitz et al., Appl. Radiat. Isot., 69, 936 (2011).

GMP-production of ^{177}Lu n.c.a. for Targeted Tumour Therapy

S. Marx, M. Harfensteller, J. Küfner, E. Adli, R. Henkelmann

ITG Isotope Technologies Garching GmbH, Garching, Germany

In recent years, ^{177}Lu, which has a half-life of 6,64 d, has emerged as a very promising radionuclide for therapeutic applications. In the clinical use of radionuclides, it is important to achieve a high specific activity and a reliable supply in pharmaceutical quality. Therefore, in the surroundings of the FRM II, the world's only professional production facility for carrier free ^{177}Lu (^{177}Lu n.c.a.) was established in the laboratories of ITG Isotope Technologies Garching GmbH in order to produce sufficient amounts of the radionuclide with the highest specific activity in GMP (Good Manufacturing Practice) quality.

Figure 1: GMP production of ^{177}Lu n.c.a. in the cleanroom of ITG Isotope Technologies Garching GmbH.

Due to its chemical and physical properties, the ß-emitting radionuclide ^{177}Lu shows a great potential for application in nuclear medicine. As a result, the demand for this radionuclide has risen continuously in the last years. It is mainly used for the therapy of neuroendocrine tumours, in the so-called Peptide Receptor Radionuclide Therapy (PRRT). Used in combination with the diagnostic radionuclide ^{68}Ga, it is a big step in the direction of Personalized Medicine: The ^{68}Ga can be tagged to the same biomolecules as ^{177}Lu. This makes it feasible to analyze the prosperity of the treatment in advance, which is rarely possible in cancer therapy.

No limitation for the clinical application

Several suppliers currently provide carrier added ^{177}Lu (^{177}Lu c.a.). This material has two drawbacks, a limited specific activity of less than 1000 GBq/mg and a contamination with a long-lived isomer of the ^{177}Lu that cannot be avoided due to the direct production route for the ^{177}Lu c.a. through the irradiation of inactive ^{176}Lu with thermal neutrons. The latter is the metastable isomer ^{177m}Lu with a half life of 160 d. Due to the fact that this ^{177m}Lu is applied together with the therapeutically effective ^{177}Lu, it is excreted by the patients. Besides injecting an undesirable isomer into the patients, this fact reduces the usability of Lu-177 c.a. Due to waste water regulations, the maximum level of long-lived radionuclides in the waste water systems of the hospitals limits the number of possible treatments.

Non carrier added ^{177}Lu (^{177}Lu n.c.a.) is produced via an indirect route. Instead of "cold" ^{176}Lu, ^{176}Yb is irradiated in the reactor. Due to the low cross capture section of the ^{176}Yb of only 3.1 barn, this route is only feasible in high flux reactors such as the FRM II. The advantage of this pro-

duction route is the possibility of separating the target material from the produced ^{177}Lu. Therefore, practically all atoms of the product are radioactive – a radionuclide in “non carrier added” quality is obtained. As a result, Lu-177 n.c.a. shows a very high specific activity of more than 3700 GBq/mg, more than 3 times higher than that is technically achievable for the carrier added ^{177}Lu c.a. This makes it possible to reduce the number of biomolecules that is needed for the Targeted Tumour Therapy. In addition, the ^{177}Lu n.c.a. contains practically no long-lived ^{177m}Lu. Thus, none of the limitations of the ^{177}Lu c.a. regarding the clinical application apply.

For the use of Lu-177 n.c.a. in medicine, the daily availability of this radionuclide needs to be guaranteed at a consistently high quality level and pharmaceutical grade. Therefore, the aim was to establish a reliable supply with sufficient amounts of ^{177}Lu n.c.a. for the needs of nuclear medicine.

Fulfillment of pharmaceutical criteria

To realize these production capabilities, a scale-up of the capacity from experimental to industrial scale was performed. For that reason, a special separation technique had to be established. To secure consistent supply with ^{177}Lu n.c.a., the capsule irradiation facility KBA of the FRM II was transformed to enable the irradiation of multiple sources at the same time in a cyclic process that offers the possibility of taking out one selected source at a certain point during the irradiations. In addition, a network of high flux reactors was installed to cover the maintenance stops of the FRM II. The production process had to be designed to fulfill pharmaceutical criteria. Therefore, clean room laboratories were installed at the IAZ (Industrial Application Centre of the FRM II). Due to the need to guarantee a consistent level of high quality, quality control procedures had to be established to observe impurities and the specific activity of the radionuclide, as well as sterility and the endotoxin content. In the last quarter of 2011, ITG received the manufacturing authorization for ^{177}Lu n.c.a.

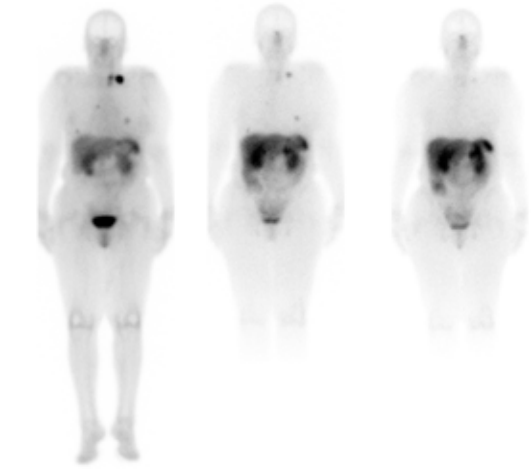

Figure 2: Scans of a patient treated with Lu-177 labelled peptide.

Extremely high purity

In the last two years, the routine production of ^{177}Lu n.c.a. was successfully established. It became possible to increase the capacity continuously up to a level that is sufficient to supply Europe and other countries all over the world 52 weeks a year. The high quality and specific activity could be verified by the use of several analytical techniques, as well as the low endotoxin content and the sterility of the product. It was shown that ^{177}Lu n.c.a. is superior in its use in nuclear medicine due to its extremely high specific activity and radionuclidic purity. The achieved manufacturing authorization for this high quality product enables ITG to apply for the market authorization for approved ^{177}Lu n.c.a.

Details of an electric control cabinet
in the neutron guide hall west

Facts & Figures

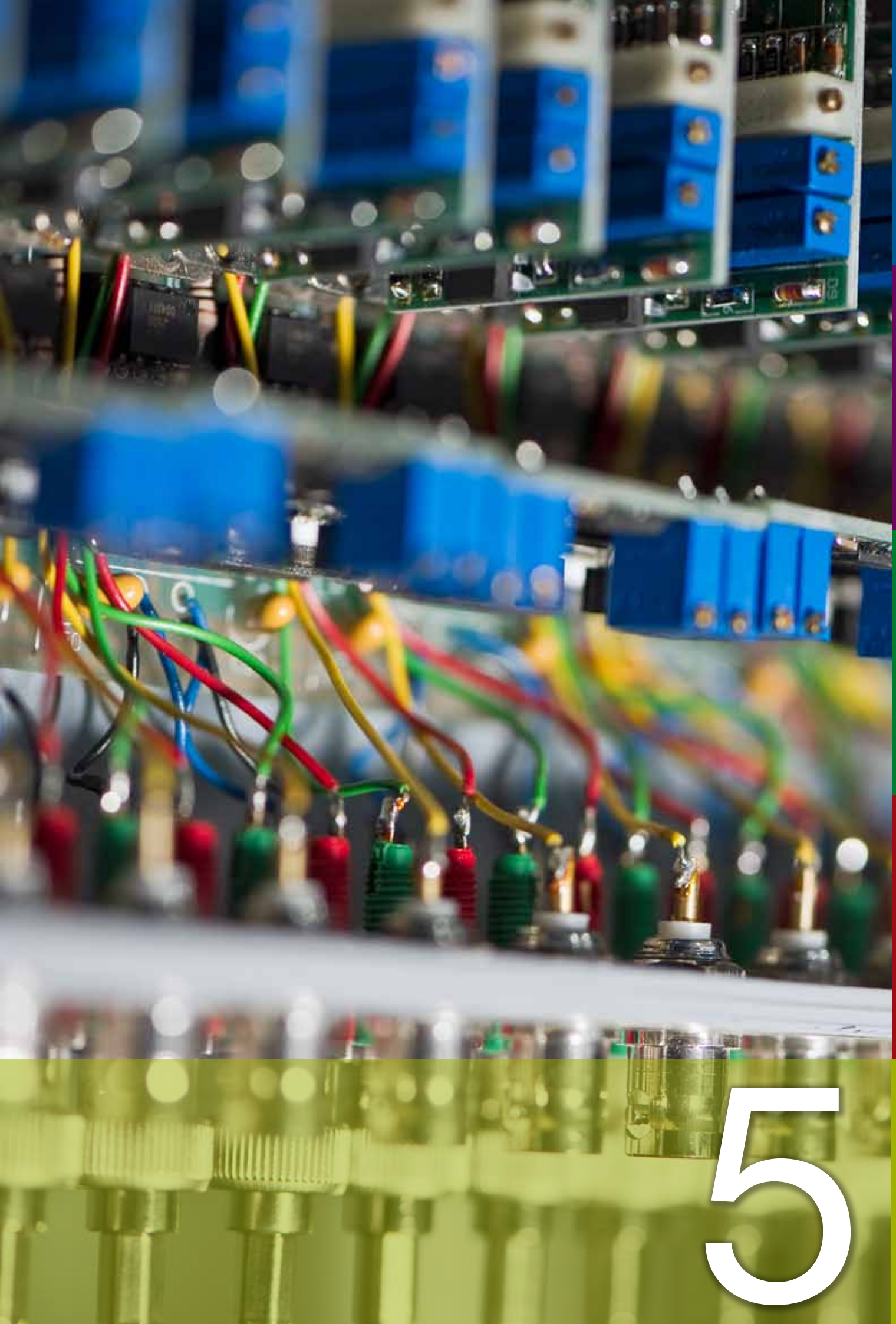

5

Events 2011: Workshops, colloquia, students' courses and open day

I. Lommatzsch[1], R. Gernhäuser[2], R. Zorn[3], M. Meven[1], A. Schneidewind[1,4], A. Voit[1]

[1]Technische Universität München, Forschungs-Neutronenquelle Heinz Maier-Leibnitz (FRM II), Garching, Germany

[2]Technische Universität München, Physik Department E12, Garching, Germany

[3]Forschungszentrum Jülich GmbH, Jülich, Germany

[4]Helmholtz-Zentrum Berlin für Materialien und Energie, Gemeinsame Forschergruppe HZB - TU Dresden, Berlin, Germany

Tutorial at DPG Meeting

During the Spring Meeting of the Deutsche Physikalische Gesellschaft (DPG), tutorials are organized to give insight into special fields and the methods of the organizing divisions. For the 2011 meeting in March, Prof. Dr. Christine Papadakis (TUM physics department) arranged a tutorial on neutron scattering methods for chemical and polymer physics. Three speakers outlined a neutron scattering method on Sunday afternoon, prior to the welcome-party. Surprisingly, the 90-seat lecture room was too small to house all the, predominantly young, audience.

Prof. Dr. Stephan Förster of the Universität Bayreuth explained the application of small angle scattering to the relationship between polymer architecture and self-assembly. The principles and applications of neutron reflectometry and grazing incidence small angle neutron scattering were presented by Dr. Roland Steitz, Helmholtz-Zentrum Berlin für Materialien und Energie (HZB). The last talk, by Dr. Astrid Schneidewind (HZB - TU Dresden, FRM II), gave an introduction to spectroscopic measurements using neutrons. Three-axis spectroscopy and the main time-of-flight techniques were compared and their complementary use was demonstrated on examples.

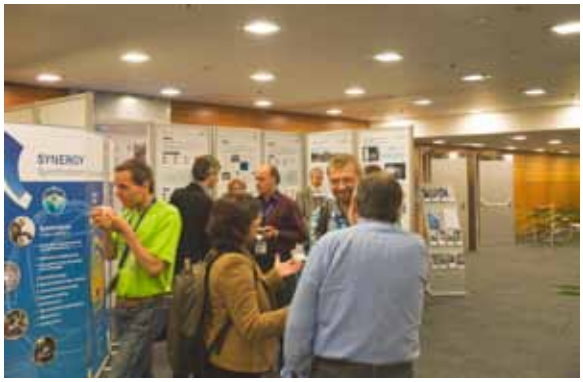

Figure 1: The jointly organized booth at the European Conference of Neutron Scattering in Prague by the scientific cooperation of TUM, JCNS, HZB and HZG.

Heinz Maier-Leibnitz' 100th birthday

Heinz Maier-Leibnitz would have turned 100 on March 28th, 2011. To celebrate his birthday, the two scientific institutes of the Technische Universität München (TUM) that bear the name of Maier-Leibnitz, the neutron source Heinz Maier-Leibnitz and the accelerator Maier-Leibnitz, sent out invitations to a colloquium. Heinz Maier-Leibnitz is known as the father of the so-called Atomic Egg in Garching and the physics department of the TUM. He died in December 2000.

At the colloquium for his 100th birthday, speakers representing all aspects of his scientific and political career were invited (fig. 3). Prof. Dr. Winfried Petry and Prof. Dr. Stephan Paul welcomed the 350 guests. The Bavarian Minister for Science, Dr. Wolfgang Heubisch, opened the proceedings with a speech praising the far-reaching scientific excellence of Maier-Leibnitz' achievement. Speaking as a successor of Maier-Leibnitz, the current President of the German Research Foundation, Prof. Dr. Matthias Kleiner, gave an insight in the present funding of science. The scientific work of Maier-Leibnitz was acknowledged by the President of the TUM, Prof. Dr. Dr. h.c. mult. Wolfgang A. Herrmann. A personal view of the researcher Maier-Leibnitz was given by Prof.

Figure 2: Prof. Peter Müller-Buschbaum (r.) presented a photograph of staff members to Prof. Winfried Petry, to celebrate his 60th birthday.

Dr. Paul Kienle in his review. Prof. Dr. Colin Carlile, Director of the planned European Spallation Source in Sweden, gave an outline of future neutron science. Then, Prof. Dr. Stephan Paul of the TUM excellence cluster “Universe” explained, how neutrons can be used to explore the origin of the universe. And finally, the Heinz Maier-Leibnitz’ prize laureate 2010, Dr. Ansgar Reiners, talked about the freedom of research.

The talks of Matthias Kleiner, Paul Kienle and Ansgar Reiners (in German) can be downloaded at http://www.frm2.tum.de/en/aktuelles/events/archive/100-geburtstag-maier-leibnitz/index.html.

Colloquium for Professor Winfried Petry

The FRM II and the E13 chair of the physics department at the Technische Universität München celebrated Prof. Dr. Winfried Petry’s 60th birthday on June 16th with a colloquium (see fig. 2). Welcoming words to the 320 guests were spoken by the director of the Bavarian ministry for research, Dr. Adalbert Weiß, on behalf of Minister Dr. Wolfgang Heubisch.
The president of the Technische Universität München, Prof. Dr. Dr. h.c. mult. Wolfgang A. Herrmann, paid tribute to the scientific director of the FRM II as a science communicator and the dean of the physics department, Prof. Dr. Martin Stutzmann, highlighted the “dynamics” of Winfried Petry, both in his research and every-day life. The invited talks also dealt with dynamics in Winfried Petry’s research, for example, in the liquid-glass transition and soft matter dynamics. They were given by Winfried Petry’s Ph.D. supervisor Prof. Dr. Gero Vogl (Universität Wien), his colleague Prof. Dr. Richard Wagner (Institut Laue-Langevin Grenoble) and his former Ph.D. student Prof. Dr. Andreas Meyer (Deutsches Zentrum für Luft- und Raumfahrt).

Prof. Dr. Peter Müller-Buschbaum of the physics department E13 had organized a special issue of the Journal of Physics - Condensed Matter (vol. 23, No. 25, http://iopscience.iop.org/0953-8984/23/25).

Figure 3: 350 guests honoured Heinz Maier-Leibnitz in a colloquium at the physics department of the TUM. Among them the chancellor of the TUM, Albert Berger, the Bavarian Minister for Science, Dr. Wolfgang Heubisch, the president of the German research foundation, Prof. Dr. Matthias Kleiner and FRM II director Prof. Dr. Winfried Petry.

5th European Conference on Neutron Scattering

The FRM II and its cooperation partners JCNS, HZB and HZG participated with a joint booth at the 5th European Conference on Neutron Scattering (ECNS) in Prague (fig. 1). They sponsored the ECNS 2011 as a platinum partner and stocked the largest booth of all neutron facilities. Between the talks and poster sessions, the booth was crowded. Scientists wanted to know the experimental facilities available at the FRM II and at the HZB and how to apply for beam time there. The staff of the FRM II and the Helmholtz centres Jülich (FZJ), Berlin (HZB) and Geesthacht (HZG) presented their scientific results in a total of more than 50 contributions at the ECNS: 20 talks and approximately 30 posters.

4th Advanced Summer School SSRDM 2011

The 4th international Advanced Summer School in Radiation Detection and Measurements (SSRDM 2011) took place in Munich. The school is jointly organised by the University of California Berkeley, the University of Tokyo, the Technische Universität München and the Max Planck Institute (MPI) for Physics. This summer, 60 students had the opportunity to become familiar with modern concepts of detectors in nuclear and particle physics, neutron research, and their applications

in medicine and astrophysics. The special highlight of the visits in between the lectures was to the neutron source on July 26th and 27th. Dr. Karl Zeitelhack, head of the detector and electronics group at the FRM II, who had co-organised the school, accompanied the students on a tour of the detectors and scientific instruments (fig. 4).

Fortgeschrittenen-Praktikum

60 students of physics of the Technische Universität München were able to practice neutron scattering with hands-on experiments in June and December 2011. Whereas the practical course for undergraduate students in June was performed in 'dry runs' due to lack of neutrons, the December course was able to use neutrons at the instruments STRESS-SPEC, PUMA, SPODI, RESI (fig. 5), HEiDi, J-NSE, TOFTOF, KWS-2, RESEDA and PGAA in the first cycle after the maintenance break.

15th JCNS LabCourse

In September, the Jülich Centre for Neutron Science (JCNS) organised its annual Laboratory Course Neutron Scattering. As in previous years, the lab course was held at two locations: at Forschungszentrum Jülich for the lecture element and at the neutron source FRM II in Garching for the experiments. Funding was provided by Forschungszentrum Jülich with support from NMI3 (EU framework programme 7), and the European Network of Excellence SoftComp.
54 students out of 155 applicants were accepted. Many instruments at the FRM II were made available for student training: PUMA, SPODI, HEiDi, TOFTOF, RESEDA, TREFF, KWS-1, KWS-2 (fig. 6), KWS-3, DNS. J-NSE, SPHERES. This year's course was influenced by the long maintenance break. For this reason, the experiments could only be performed as 'dry runs'. The students had to use data stored from previous experiments. In most cases, this did not interfere too much with the didactical objectives. The advantage: The absence of radiation allowed the students to see parts of the instruments which, during normal operation, have to be shielded, such as neutron guides or monochromators. The next JCNS laboratory course will take place on September 3rd to 14th, 2012. In spring 2012, more details will be posted at www.neutronlab.de.

Neutron Scattering for Crystallographers

On the occasion of the combined annual meeting of the DGK (Deutsche Gesellschaft für Kristallographie), DGM and ÖMG (Deutsche resp. Österreichische Mineralogische Gesellschaft) in autum in Salzburg the DGK's workgroup „Neutron Scattering" and its speaker Dr. Martin Meven organized a satellite a workshop from September 19th to 20th. The aim of the workshop, which focused on students and scientists from different natural and materials sciences backgrounds, was to present the basics and various methods of neutron scattering, as well as the variety of its applications.

Figure 4: The advanced summer school SSRDM during their visit to the FRM II with Dr. Karl Zeitelhack (front row, right).

Figure 5: Fascinating neutron science for students at the Fortgeschrittenen-Praktikum of the TU München at the RESI single crystal diffractometer.

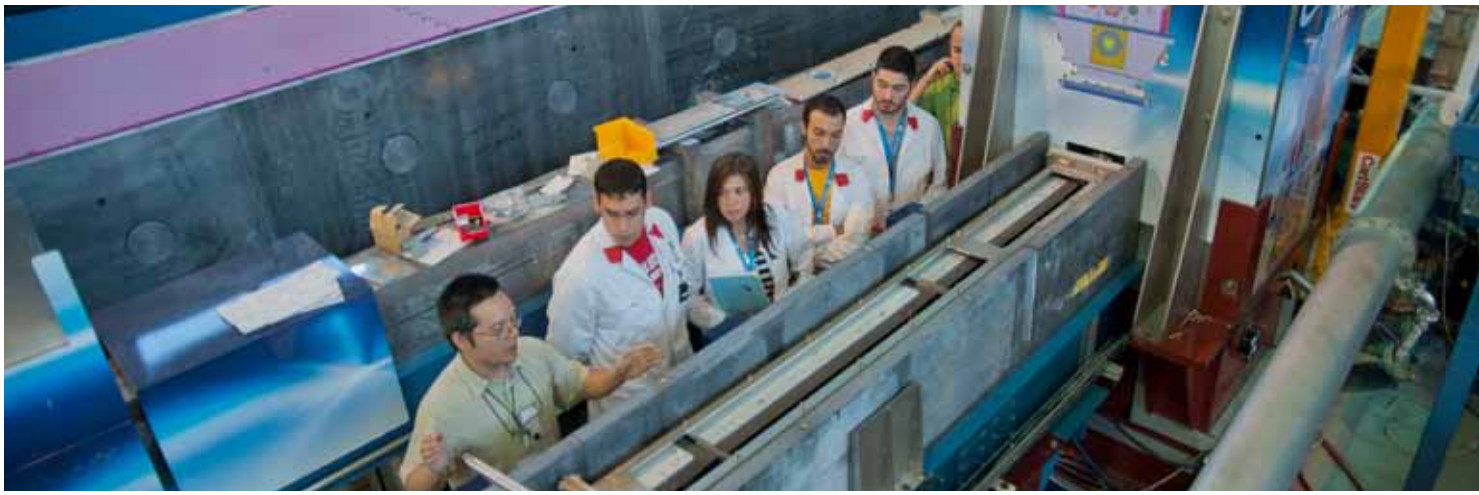

Figure 6: Students at the JCNS small angle instrument KWS-2 during the lab course.

On the first day, a total of 15 participants from ten different universities attended lectures held by Prof. Dr. Markus Braden (Universität zu Köln), Prof. Dr. Friedrich Frey (LMU), Dr. Ralph Gilles (TUM), Dr. Martin Meven (TUM), Dr. Astrid Schneidewind (HZB) and Prof. Dr. Regine Willumeit (HZG). The range of the presented methods covered powder and single crystal diffraction, magnetism, spectroscopy and small-angle scattering. On the next day the instruments associated with the different methods were shown to the participants during a guided tour of the neutron source Heinz Maier-Leibnitz.
Both the broad spectrum of participants, from graduate students to university professors, and the numerous questions and discussions following the lectures and even during the guided tour testify the high level of the large interest in the topics presented.

500 Happy People at the FRM II Open Day

More than 500 people patiently waited in the long line-up for registration at the FRM II booth on the open day October 15th (fig. 7). Together with 27 other institutes at the research campus in Garching, the FRM II opened its doors to the public, offering tours from 10:00 to 18:00. In the early afternoon, all 29 tours were fully booked. 496 people in total were conducted by FRM II staff through the experimental hall, the neutron guide hall, and had a look at the reactor pool.
Those who arrived too late to register were able to visit the talks offered by the neutron source in the physics department. They learned more about research using anti-particles at the positron source from Dr. habil. Christoph Hugenschmidt, tumour treatment using fission neutrons from Dr. Birgit Loeper-Kabasakal, existing and planned radioisotope production from Dr. Heiko Gerstenberg, and industrial applications from Dr. Ralph Gilles. The scientific director of the neutron source, Prof. Dr. Winfried Petry, gave an insight into research using neutrons, and the technical director Dr. Anton Kastenmüller explained the safety features to an interested audience. Films about the FRM II shown in a lecture hall also attracted visitors. The booth of the radiation protection group was well attended. People were surprised to see the natural sources of radiation presented by those responsible for radiation protection, Dr. Helmut Zeising and Marcel Kaleve, as well as Franz Michael Wagner.

Figure 7: Long line-up for the registration at the FRM II booth on the open day.

2011: A User Office without users ...

T. Gutberlet[1], R. Bruchhaus[2], J. Neuhaus[3], F. Carsughi[2], I. Lommatzsch[3], B. Tonin-Schebesta[3], U. Kurz[3]

[1]Helmholtz-Zentrum Berlin für Materialien und Energie, Berlin, Germany

[2]Forschungszentrum Jülich GmbH, Jülich Centre for Neutron Science at FRM II, Garching, Germany

[3]Technische Universität München, Forschungs-Neutronenquelle Heinz Maier-Leibnitz (FRM II), Garching, Germany

Normally, the joint User Office deals with around 1000 scientists who visit the FRM II in the course of their experiments. It organises the proposal rounds, invites users to scheduled experiments, caters for their stay at the FRM II, etc. But: 2011 was the year of the long maintenance break and that was really an unusual situation for the User Office. After the research neutron source resumed operation on October 29th, 2011, the first external users began carrying out experiments on STRESS-SPEC on November 7th, 2011. So, what did the User Office do for ten months in 2011?

Staff turnover

First of all, the head of the User Office, Thomas Gutberlet of JCNS, left in January and took up a new challenge as Head of User Coordination Neutrons at the Helmholtz-Zentrum Berlin. We would like to take this opportunity to thank him for his work and wish him all the very best in his future endeavours.

Rainer Bruchhaus became JCNS user officer as a stand-in for the period April to August. Finally, in August, Flavio Carsughi took up his post at the User Office in Garching.

Proposals despite lack of neutrons

May saw the only proposal round in 2011, with a review in June. A total of 285 proposals were submitted to the 24 instruments hosted at the FRM II and operated by JCNS, HZB, HZG, TUM, MPG and German universities. Looking at the history of proposal submission, this was not an unusual number - as depicted on the diagram (next page).

The planned second proposal round was then moved to January 2012 so that the regular dates of the proposal rounds in January and July could be established once more.

Booth at the ECNS

The User Office was also in charge of the organisation of the joint booth of the cooperation partners TUM, FZJ, HZB and HZG at the ECNS in Prague in July. The partners sponsored the conference as a platinum partner and stocked the largest booth of all neutron facilities. It was a resounding success and prepared the comeback of the FRM II as a facility for the user community. The user officers at the booth advertised, answered all questions and were happy to arrange conversations with the responsible instrument

Thomas Gutberlet

Rainer Bruchhaus

Flavio Carsughi

Left: Staff members of FRM II, HZB, HZG and JCNS at the ECNS in front of a common booth.

scientists. For the first time the cooperation becomes visible through this joint booth! A booklet summarizing the German Neutron facilities was presented to the conference participants.

Right: Booklet of German neutron centres.

FRM II news - now printed copies

It was also a great opportunity to distribute the first printed FRM II newsletter. Established in 2008, with the first issue in December, it grew from a pdf file that could be downloaded to an interesting magazine. All users of the FRM II can ask for the newsletter to be delivered within their personal account settings of the digital user office system. You are no user? No problem - just write an email to the User Office (userinfo@frm2.tum.de) and order it!

On October 29th, the first neutrons became available and the FRM II was back in business. The User Office celebrated this with a special issue of the newsletter.

Finally, users again!

During the 60 beam days in 2011, 122 external users visited the FRM II to carry out experiments once more - and the User Office was more than happy to welcome them again!

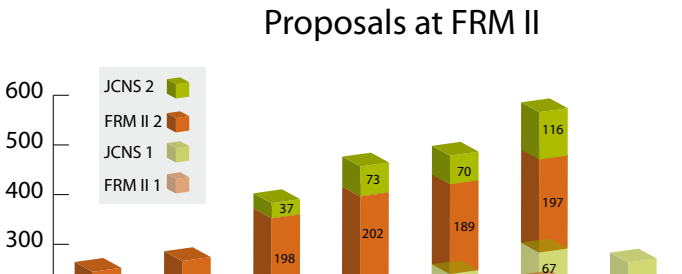

Serving visitors and journalists: Visitors' service and public relations

A. Voit[1], U. Kurz[1], B. Tonin-Schebesta[1]

[1]Technische Universität München, Forschungs-Neutronenquelle Heinz Maier-Leibnitz (FRM II), Garching, Germany

The year 2011 has held many challenges for the FRM II, especially in the wake of the nuclear accident in Fukushima. The long maintenance break and minor technical problems, as a corroded safety flap, coincided with the disaster in Japan. This confined questions of public relations almost completely to safety issues. However, on the other hand, provided the opportunity to promote the safe and modern concept of the research neutron source. Again, almost 3000 visitors were welcomed in the course of the year.

Safety issues have high priority for media

As a consequence of the Fukushima accident, numerous talks and open discussion panels were hosted by the FRM II scientific and technical directors on the topics of nuclear safety and the Fukushima accident (see table 1). More than 3000 people attended these events. Intense media interest with several film teams visiting the FRM II, was satisfied by the public relations office (fig. 1). In the first two weeks after the reactor accident in Japan, 28 calls, visits or inquiries from journalists were dealt with. Several press releases concerning the safety of the FRM II were sent out, while frequently asked questions on safety issues were immediately posted on the website www.frm2.tum.de. Out of 138 media clippings on the FRM II in 2011, 53 were purely positive, covering for example on scientific or medical aspects of the neutron source.

In order to enhance competence in cooperating with the media, the scientific and technical directors, as well as the press officer of the FRM II, held a two day camera and media training course in April. In July, a delegation from the Korean Atomic Energy Research Institute (KAERI) and a journalist visited the FRM II to seek information about public relations policies (fig. 2).

Almost 3000 visitors welcomed

Despite the long maintenance break and the reduced accessibility of certain areas - the experimental hall was partly closed for visitors - almost 3000 visitors came to see the FRM II (fig 3). FRM II as well as JCNS staff members and student trainees guided them.

Figure 1: The Bayerische Rundfunk interviewing Prof. Winfried Petry for the evening news in the neutron guide hall west about the experimental facilities of the FRM II.

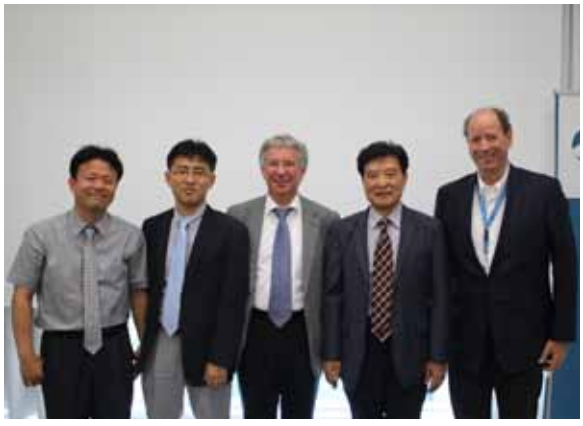

Figure 2: Visit of the KAERI delegation on public relations issues at the FRM II with scientific director, Prof. Winfried Petry (m.), and associate director Dr. Jürgen Neuhaus (r.).

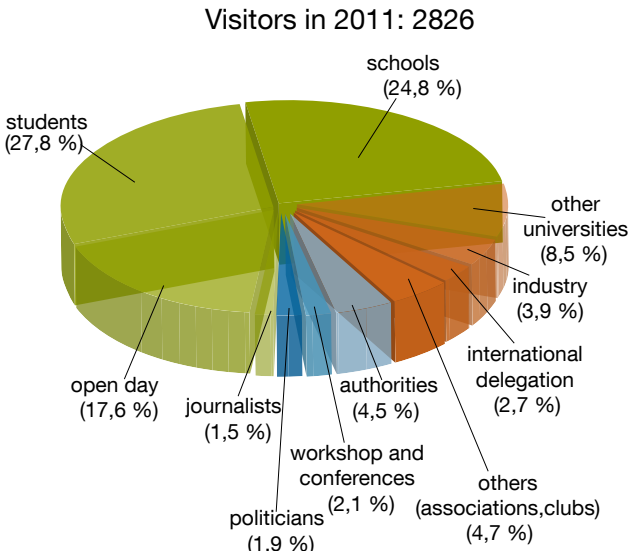

Figure 3: In total, 2826 visitors were guided at the FRM II in 2011.

A course at the Werner Heisenberg Gymnasium in Garching asked 418 visitors for their opinion in order to evaluate the tours: The overall reaction was very positive. Students and older visitors were especially very satisfied with the information they were given both about the neutron source itself and the different instruments and experiments.

The open day was a success once again (see text “Events” in this chapter) with fully booked tours and more than 500 visitors.

A novum at the FRM II was the first official political visit by members of the party Bündnis 90/Die Grünen in November 2011. The city council members of the city of Munich and other party members were accompanied by the three FRM II directors during their tour of the neutron source.

Date	Event	Location	Speaker	Audience
25th March	Lecture at the TUM	Garching	Dr. A. Kastenmüller	700
15th March	Open council	Garching	Dr. A. Kastenmüller	500
18th March	Panel discussion	München	Prof. Dr. W. Petry	500
7th April	Lecture at the TUM	Garching	Dr. A. Kastenmüller	500
18th March	Lecture at the TUM	Garching	Dr. A. Kastenmüller	400
12th July	Lecture at the TUM	Garching	Dr. A. Kastenmüller	300
13th April	Lecture for pupils	München	Dr. R. Georgii	100
10th May	Presentation for scientists	Garching	Dr. A. Kastenmüller	100
24th May	Lecture at panel discussion	München	Prof. Dr. W. Petry	100
12th May	Lecture at panel discussion for physicians	München	Dr. K. Schreckenbach	50
26th May	Panel discussion	München	Prof. Dr. W. Petry	50
26th May	Lecture for open public	Ebersberg	Dr. A. Kastenmüller	50
9th June	Lecture at panel discussion	München	Dr. K. Böning	30
			Total	3380

Table 1: Panel discussions with participation of FRM II staff and lectures given after Fukushima.

“Perspectives of neutron research in Germany”

In 2011, the FRM II press office together with the “Komitee Forschung mit Neutronen” released a new brochure “Perspectives of neutron research in Germany” (fig. 2). It is available online at www.frm2.tum.de/en/aktuelles/info-documents/misc0.

Figure 4: The brochure „Perspectives of neutron research in Germany“ of the „Komitee Forschung mit Neutronen“ was jointly released with the FRM II press office.

Figure 5: Headlines in the newspapers and magazines reporting on the FRM II in the year 2011. In total, there were 138 media clippings on the neutron source.

Committees

Koordinierungsrat (Steering Committee)

Chairman

Prof. Dr. Sebastian Schmidt
Member of the Executive Board of
Forschungszentrum Jülich

Members

Prof. Dr. Wolfgang Kaysser
Member of the Executive Board of
Helmholtz-Zentrum Geesthacht

Dr. Ulrich Breuer
Member of the Executive Board of
Helmholtz-Zentrum Berlin

MinR Stefan Kern
Federal Ministry of Education and Research

MRin Dr. Ulrike Kirste
Bayerisches Staatsministerium für
Wissenschaft, Forschung und Kunst

Prof. Dr. Dr. h.c. mult. Wolfgang A. Herrmann
President
Technische Universität München
represented by Prof. Dr. Thomas Hofmann,
Vice-president
of the Technische Universität München

Albert Berger
Chancellor
of the Technische Universität München

Prof. Dr. Stephan Paul
Physics Department
Technische Universität München

Guests

Prof. Dr. Winfried Petry, Scientific Director of the Scientific Cooperation representing TUM

Prof. Dr. Dieter Richter, Scientific Director of the Scientific Cooperation representing HGF institutions

Dr. Anton Kastenmüller
Technical Director ZWE-FRM II,
Technische Universität München

Dr. Klaus Seebach
Administrative Director ZWE-FRM II,
Technische Universität München

The Koordinierungsrat at its first meeting in June 2011.

Wissenschaftlicher Beirat (Scientific advisory board):

Chairman

Prof. Dr. Peter Fratzl
Max-Planck-Institut für Kolloid- und Grenzflächenforschung, Potsdam

Members

Prof. Dr. Hartmut Abele
Atominstitut der Österreichischen Universitäten
Technische Universität Wien

Prof. Christiane Alba-Simionesco
Laboratoire Léon Brillouin
Centre d'Energie Atomique, Saclay

Prof. Dr. Arantxa Arbe
Unidad de Fisica de Materiales
Facultad de Quimica, San Sebastian

Prof. Dr. Andrew Harrison
Institut Laue Langevin, Grenoble

Prof. Dr. Dirk Johrendt
Department Chemie und Biochemie
Ludwig-Maximilians-Universität, München

Prof. Dr. Bernhard Keimer
Max-Planck-Institut für Festkörperforschung, Stuttgart

Prof. Dr. Joël Mesot
Paul Scherrer Institut, Villigen

Prof. Dr. Joachim O. Rädler
Department für Physik
Ludwig-Maximilians-Universität, München

Prof. Dr. Walter Reimers
Institut für Werkstoffwissenschaften
und -technologien, Technische Universität Berlin

Dr. Jens Rieger
Senior Vice President, Polymer Research
BASF SE, Ludwigshafen

Prof. Dr. Metin Tolan
Leiter Beschleuniger- & Synchrotronlabor
Technische Universität Dortmund

Evaluation of beam time proposals scientific committee FRM II

Dr. Françoise Bourrée
Laboratoire Léon Brillouin
Centre d'Energie Atomique, Saclay

PD Dr. Reiner Dahint
Ruprecht-Karls-Universität Heidelberg
Arbeitsgruppe Biosensorik und Biomaterialien

Prof. Dr. Antonio Deriu
Università degli studi di Parma
Dipartimento di Fisica

Prof. Dr. Helmut Ehrenberg
Karlsruher Institut für Technologie
Institut für Angewandte Materialien – Energiespeichersysteme

Dr. Björn Fak
Centre d'Energie Atomique, Grenoble

Dr. Rashid Gareev
Universität Regensburg
Fakultät für Physik, Institut für Experimentelle und Angewandte Physik

The committee for the evaluation of beam time proposals at its meeting in June 2011.

Prof. Dr. Rupert Gebhard
Archäologische Staatssammlung München
Abteilung Vorgeschichte

Prof. Dr. Christoph Genzel
Helmholtz-Zentrum Berlin
Institut für Werkstoffe/Bereich Funktionale Materialien

Dr. Holger Gibhardt
Georg-August-Universität Göttingen
Institut für Physikalische Chemie

Dr. Klaus Habicht
Helmholtz-Zentrum Berlin

Dr. Thomas C. Hansen
Institut Laue Langevin, Grenoble

Dr. Dmytro Inosov
Max-Planck-Institut für Festkörperforschung, Stuttgart

Dr. Nikolay Kardjilov
HZB für Materialien und Energie
Institut für Angewandte Materialforschung

Dr. Thomas Krist
Helmholtz-Zentrum Berlin

Dr. Kim Lefmann
Kobenhavns Universitet
Niels Bohr Institute, Nanofysik

Dr. Dieter Lott
Helmholtz-Zentrum Geesthacht

Dr. Emmanuel Kentzinger
Forschungszentrum Jülich

Dr. Eberhard Lehmann
Paul Scherrer Institut, Villigen

Dr. Bernd Leiss
Geowissenschaftliches Zentrum Universität Göttingen

Prof. Dr. Martin Müller
Helmholtz-Zentrum Geesthacht
Institut für Werkstoffforschung

Prof. Dr. Oskar Paris
Montanuniversität Leoben

Prof. Dr. Juan-Manuel Pérez-Mato
Universidad del País Vasco
Departamento de Física de la Materia Condensada y Física Aplicada II

Dr. Wim Pyckhout-Hintzen
Forschungszentrum Jülich
Institut für Festkörperforschung

Prof. Dr. Klaus Rätzke
Christian-Albrechts-Universität zu Kiel
Institut für Materialwissenschaft und -verbunde

Dr. Juerg Schefer
ETH Zürich und Paul Scherrer Institut, Villigen
Laboratory for Neutron Scattering

Dr. Henk Schut
TU Delft
Technische Natuurwetenschappen

Dr. Ivan Sidis
Laboratoire Léon Brillouin
Centre d'Energie Atomique, Saclay

Referees evaluating the proposals for beam time.

Scientific committee JCNS

Prof. Dr. Jean-Michel Sprauel
Université de la Méditerranée, France
IUT/Dépt. Génie Mécanique et Productique

Dr. Jochen Stahn
ETH Zürich und Paul Scherrer Institut, Villigen
Laboratory for Neutron Scattering

Dr. Peter Staron
Helmholtz-Zentrum Geesthacht
Institut für Werkstoffforschung

Dr. Paul Steffens
Insitut Laue Langevin, Grenoble

Prof. Dr. Thomas Thurn-Albrecht
Martin-Luther-Universität Halle-Wittenberg
Institut für Physik/Experimentelle Polymerphysik

Prof. Dr. Helena Van Swygenhoven-Moens
Paul Scherrer Institut, Villigen

Dr. Martin Weik
Institut de Biologie Structurale, Grenoble

Dr. Andrew Wildes
Institut Laue Langevin, Grenoble

Dr. Michael Zawisky
Atominstitut der Österreichischen Universitäten

Prof. Dr. Oliver Zimmer
Institut Laue Langevin, Grenoble

Prof. Dr. Peter Böni
Technische Universität München
Physik Department, Arbeitsgebiet “Stark korrelierte Elektronensysteme”

Dr. Bernhard Frick
Institut Laue Langevin, Grenoble

Dr. Arsène Goukassov
Laboratoire Léon Brillouin
Centre d’Energie Atomique, Saclay

Dr. Reidar Lund
Donostia International Physics Center, Spain

Prof. Christine Pappas
TU Delft

Prof. Walter Richtering
Physikalische Chemie II
Rheinisch-Westfälische Technische Hochschule Aachen

Dr. Oliver Stockert
Max-Planck-Institut für Chemische Physik fester Stoffe, Dresden

Prof. Kristiaan Temst
Katholieke Universiteit Leuven

Prof. Tobias Unruh
Lehrstuhl für Kristallographie und Strukturphysik
Friedrich-Alexander-Universität Erlangen-Nürnberg

Prof. Regine Willumeit
Helmholtz-Zentrum Geesthacht

Staff

Scientific Cooperation

The scientific cooperation between the Technische Universität München (TUM) and the three Helmholtz centres (HGF institutions) at Jülich, Geesthacht and Berlin include the Instrument Operation, Instrument Service, Project Coordination, Executive Assistance, Office, User Office and Public Relations (see organisational chart of the scientific cooperation below). The Administration, Reactor and Science Division, comprising the Reactor Physics group, belong to the Integrative Research Center FRM II (ZWE-FRM II) operated by the TUM.

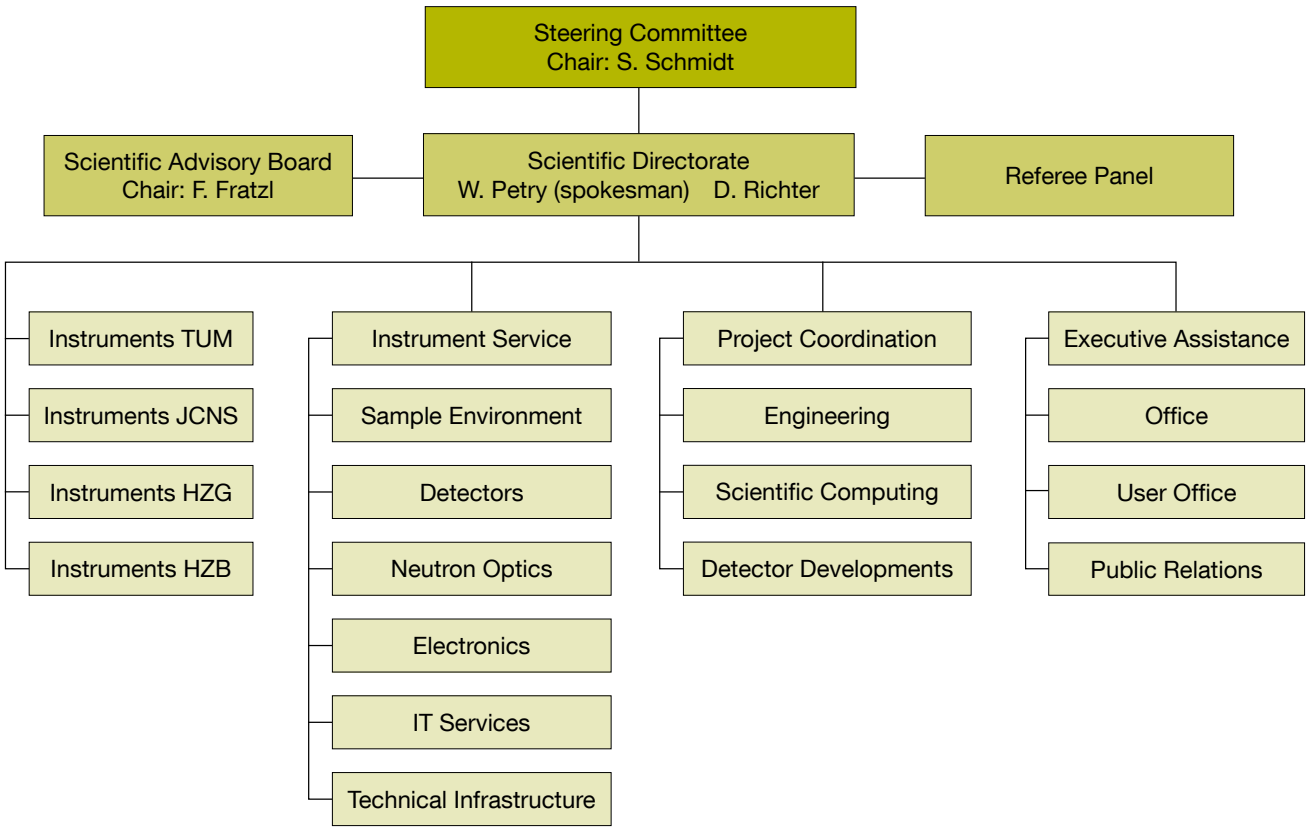

Scientific Director TUM
Prof. Dr. Winfried Petry, spokesman

Deputy
Dr. Jürgen Neuhaus

Scientific Director HGF institutions
Prof. Dr. Dieter Richter

Executive Assistance
Dr. Rainer Bruchhaus
Dr. Connie Hesse

Office
Elisabeth Jörg-Müller
Franziska Michel
Silvia Valentin-Hantschel

User Office
Dr. Flavio Carsughi
Dr. Ina Lommatzsch

Public Relations
Andrea Voit
Ramona Bucher
Oliver Kreischer (NMI3)
Juliette Savin (NMI3)

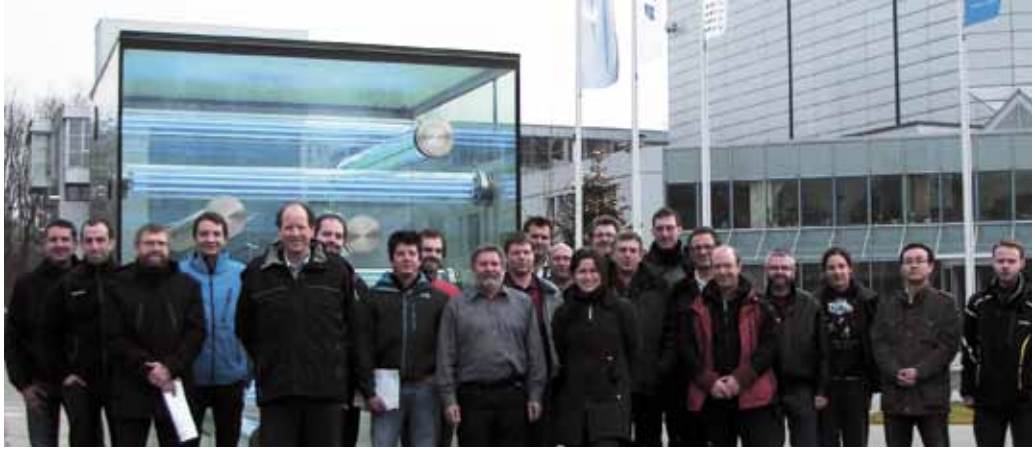

Staff members of the scientific cooperation.

Instruments TUM

Dr. Jürgen Neuhaus
Alhamdany Nowal[1]
Rainer Bierbaum
Prof. Dr. Peter Böni[2]
Georg Brandl
Kathrin Buchner[3]
Dr. Thomas Bücherl[4]
Sebastian Busch
Elbio Calzada
Dr. Lea Canella
Fernando Cristiano
Oleksandr Dolotko[5]
Dr. Andreas Frei
Fabian Fuchs
Dr. Robert Georgii
Stefan Giemsa[6]
Dr. Ralph Gilles
Dr. Alexander Grünwald[6]
Dr. Wolfgang Häußler
Tobias Heller
Dr. Michael Hofmann
Dr. Markus Hölzel
Dr. Christoph Hugenschmidt
Dr. Vladimir Hutanu[7]
Norbert Jünke
Dr. Thomas Keller[3]
Dr. Yury Khaydukov[3]
Karin Kleinstück (Erasmus Mundus)
Dr. Jens Klenke
Dr. Petra Kudejova
Elisabeth Lachner
Kathrin Lehmann
Dr. Michael Leitner
Dr. Peter Link
Dr. Birgit Loeper-Kabasakal
Dr. Wiebke Lohstroh
Wolfgang Luberstetter
Andreas Mantwill[2]
Dr. Martin Meven
Humphrey Morhenn[8]
Dr. Christoph Morkel
Martin Mühlbauer[5]
Nathalie Munnikes[3]
Dr. Andreas Ostermann
Dr. Bjørn Pedersen
Josef Pfanzelt
Philip Pikart
Dr. Christian Piochacz
Dr. Joana Rebelo-Kornmeier[2]
Markus Reiner
Dr. Julia Repper
Dr. Zsolt Révay
Jandal Ringe
Heiko Saul
Dr. Burkhard Schillinger
Philipp Schmakat
Martin Schmiele
Prof. Dr. Klaus Schreckenbach[2]
Dr. Michael Schulz
Reinhard Schwikowski
Dr. Anatoliy Senyshyn
Günther Seidl
Svatopluk Semecky
Luca Silvi
Dr. Giovanna Simeoni
Stefan Söllradl[9]
Dr. Oleg Sobolev[10]
Dr. Olaf Soltwedel[3]
Martin Stadlbauer
Rainer Stöpler[2]
Dr. Anke Teichert[10]
Pablo Torrico
Dr. Tobias Unruh
Sebastian Vohburger
Franz-Michael Wagner
Josef-Andreas Weber
Andreas Wilhelm
Alexander Wolf

[1]Clausthal University of Technology
[2]Physics Department, TUM
[3]Max-Planck-Institute for Solid State Research, Stuttgart
[4]Department for Radiochemistry, TUM
[5]Technische Universität Darmstadt
[6]Universität zu Köln
[7]RWTH Aachen
[8]Friedrich-Alexander-Universität Erlangen-Nürnberg
[9]Universität Bern
[10]Georg-August-Universität Göttingen

JCNS staff members in Garching.

Instruments JCNS

Prof. Dr. Dieter Richter (Director JCNS)
Dr. Alexander Ioffe (Head of Outstation at FRM II)

Dr. Marie-Sousai Appavou
Dr. Earl Babcock
Dr. Wouter Borghols
Dr. Zhenyu Di
Christian Felder
Dr. Artem Feoktystov
Dr. Henrich Frielinghaus
Alexandra Fuxman
Christine Gerstl
Thomas Glomann
Marco Gödel
Dennis Gurzi
Dr. Olaf Holderer
Dr. Andreas Houben[11]
Michael Kerscher
Robert Klopp
Thomas Kohnke
Dr. Denis Korolkov
Harald Kusche
Frederik Lipfert
Dr. Stefan Mattauch
Andreas Nebel
Dr. Kirill Nemkovski
Klaus Nusser
Vladimir Ossovyi
Dr. Vitaliy Pipich
Stephen Price
Dr. Sabine Pütter
Dr. Aurel Radulescu
Alfred Richter
Dr. Zahir Salhi
Harald Schneider
Florian Schneider
Dr. Gerald J. Schneider
Dr. Tobias Schrader
Simon Staringer
Dr. Yixi Su
Dr. Noemi Szekely
Dr. Jörg Voigt
Daniel Vujevic
Nico Walte[12]
Dr. Michaela Zamponi

Instruments HZB

Dr. Astrid Schneidewind
Dr. Enrico Faulhaber

Instruments HZG

Dr. Weiman Gan
Martin Haese-Seiller
Dr. André Heinemann
Dr. Jean-François Moulin
Matthias Pomm
Christian Randau

Sample environment

Dr. Jürgen Peters
Michael Beywl
Peter Biber
Andreas Buchner
Michael-Marc Fiedler
Markus Göhr
Heinrich Kolb
Herbert Weiß
Jank Wenzlaff

Detectors and electronics

Dr. Karl Zeitelhack
Yasin Abdullahi
Ilario Defendi
Christian Hesse
Dr. Martin Jurkovic
Max Panradl
Peter Wind
Dr. Irina Stefanescu

The FRM II neutron optics group with its head Dr. Peter Link (front row, 2nd from the left).

Neutron optics
Prof. Dr. Gunther Borchert
Dr. Peter Link
Christian Breunig
Eberhard Kahle
Armin Kriele
Dr. Sergey Masalovich
Andreas Ofner
Tony Reichel
Roxana Valicu[13]
Josef Weber

IT Services
Jens Krüger
Jörg Pulz
Harald Wenninger
Josef Ertl
Joao-Paulo Innocente
Nataliya Ivanova
Georg Kaspar
Babette Oberholz
Jörg Stoll
Hermann Westermayer

Apprentices at the IT Services
Andreas Erb
Simon König
Christoph Kick
Alexander Lenz
Christian Worf

Technical infrastructure
Dr. Peter Link (temporary)
Uwe Reinecke
Elbio Calzada

Scientific computing
Dr. Joachim Wuttke
Christian Felder
Dr. Walter Van Herck
Dr. Gennady Pospelov

Integrative Research Center FRM II (ZWE-FRM II)

Board of Directors
Dr. Anton Kastenmüller, Technical Director
Prof. Dr. Winfried Petry, Scientific Director
Dr. Klaus Seebach, Administrative Director

Administration

Head
Dr. Klaus Seebach

Deputy
Reinhard Obermeier

Office
Christine Zeller

Christina Auer
Karl-Heinz Drexler
Brigitte Gallenberger
Bernd Heck
Isabella Heinath
Karin Lüttig
Sabine Osorio
Kerstin Rickert
Günter Wagner

Visitors' service
Ulrike Kurz
Dott. Bianca Tonin-Schebesta

[11]RWTH Aachen
[12]Universität Bayreuth
[13]Physics Department, TUM

Reactor Division

Head of Reactor Division
Dr. Anton Kastenmüller

Office
Sylvia Rubsch
Marita Neuberger

Security
Johann Stephani

Department reactor monitoring and radiation protection
Dr. Helmut Zeising/Dr. Birgit Wierczinski
Johann Aigner
Dubravka Bahmet
Rita Bertsch
Wolfgang Dollrieß
Nihad Hodzic
Harry Hottmann
Florian Jeschke
Marcel Kaleve
Vanessa Kindel
Waldtraud Kluge
Daniela Lewin
Roland Maier
Petra Müller
Bernhard Neugebauer
Klemens Otto
Thomas Ramel
Adelheid Schindler
Michael Schmidt
Johann Schreiner
David Schrulle
Daniela Strobl
Michaela Uhlmann
Hans-Jürgen Werth
Josef Wetzl
Susanne Wolff

Department reactor enhancement
Dr. Andreas Kusterer
Holger Bamberger
Alen Begic
Christoph Berkel
Wilhelm Bünten
Johann Fink
Thomas Fliegner
Bernhard Foth
Andreas Galsterer
Christian Herzog
Andreas Huber
Philipp Jüttner
Martin Kinzler
Manuela Kutschenreuter
Karin Lichtenstein
Ralf Lorenz
Britta Pollom
Andreas Scharl
Robert jun. Schlecht
Michael Schmitt
Uwe Stiegel
Franz-Ludwig Tralmer
Dieter von Plata
Volker Zill

Department reactor operation
Dr. Axel Pichlmaier/Dr. Stefan Baldauf
Attila Bancsov
Rainer Becker
Michaela Benedikt
Albin Benke
Robert Binsch
Oliver Breu
Manfred Danner
Christian Feil
Martin Flieher
Horst Gampfer
Wolfgang Glashauser
Hubert Groß
Friedrich Gründer

Recruting new staff and student trainees: Dr. Joachim Wuttke (right) at the booth of the job fair at the University of Applied Sciences in Munich.

György Guld
Lutz Herdam
Simone Herrmann
Florian Hofstetter
Konrad Höglauer
Thomas Kalk
Georg Kaltenegger
Ulrich Kappenberg
Frank Kewitz
Marc-Guido Krümpelmann
Johann Kund
Adolf Lochinger
Gerd Mauermann
Albert Meilinger
Markus Moser
Klaus Pfaff
Ludwig Rottenkolber
Gerhard Schlittenbauer
Christiane Wickfelder
Michael Wöhner
Christian Ziller
Ismail Zöybek

Department irradiation and sources

Dr. Heiko Gerstenberg
Alexander Draack
Jean-Marie Favoli
Wolfgang Fries
Michael Fuß
Wolfgang Lange
Dr. Xiaosong Li
Volker Loder
Jens Molch
Christian Müller
Dietmar Päthe
Heike Schulz
Benjamin Schneider
Katja Singler
Norbert Wiegner
Andreas Wirtz

Department electric control systems

Roland Schätzlein
Werner Buchner
Andreas Düring
Franz Götz
Robert Krammer
Karl-Heinz Mayr
Thomas Metzger
Steffen Pfaff
Johann Wildgruber

FRM (old)

Günter Aigner
Stefan Förg
Josef Waronitza

Conventional infrastructure

Karola Frey
Andreas Heinath
André Wienholz

Science Division

Reactor physics

Dr. Anton Röhrmoser
Hsin-Yin Chiang
Dr. Harald Breitkreutz
Dr. Rainer Großmann
Tobias Hollmer
Tanja Huber
Dr. Rainer Jungwirth
Jürgen Sarvas
Robert Schenk
Wolfgang Schmid
Tobias Zweifel

Partner institutions

Bayerisches Geoinstitut
Universität Bayreuth
www.bgi.uni-bayreuth.de

Georg-August-Universität Göttingen

- Institut für Physikalische Chemie
  www.uni-pc.gwdg.de/eckold
- Geowissenschaftliches Zentrum
  www.gzg.uni-goettingen.de

German Engineering Materials Science Centre GEMS
Hemholtz-Zentrum Geesthacht GmbH
www.hzg.de

Helmholtz-Zentrum Berlin
für Materialien und Energie GmbH
www.helmholtz-berlin.de

Jülich Centre for Neutron Science JCNS
Forschungszentrum Jülich GmbH
www.jcns.info

Karlsruher Institut für Technologie

- Institut für Angewandte Materialien –
  Energiespeichersysteme (IAM-ESS)
  www.iam.kit.edu

Ludwig-Maximilians-Universität München

- Sektion Kristallographie
  www.lmu.de/kristallographie
- Sektion Physik
  www.softmatter.physik.uni-muenchen.de

Max-Planck-Institut für Festkörperforschung, Stuttgart
www.fkf.mpg.de

RWTH Aachen

- Institut für Kristallographie
  www.xtal.rwth-aachen.de
- Institut für Anorganische Chemie
  www.ac.rwth-aachen.de

Technische Universität Clausthal

- Institut für Werkstoffkunde und Werkstofftechnik
  www.iww.tu-clausthal.de

Technische Universität Darmstadt

- Fachbereich Material- und Geowissenschaften
  www.tu-darmstadt.de/fb/matgeo

Technische Universität Dresden

- Institut für Festkörperphysik
  www.physik.tu-dresden.de/ifp

Technische Universität München

- E13 – Lehrstuhl für Funktionelle Materialien
  www.e13.physik.tu-muenchen.de
- E18 – Lehrstuhl für Experimentalphysik I
  www.e18.ph.tum.de
- E21 – Lehrstuhl für Neutronenstreuung
  www.e21.ph.tum.de
- RCM - Radiochemie München
  www.rcm.tum.de

Universität Augsburg

- Institut für Physik
  www.physik.uni-augsburg.de/cpm

Universität der Bundeswehr München

- Institut für Angewandte Physik und Messtechnik
  www.unibw.de/lrt2

Universität zu Köln

- Institut für Kernphysik
  www.ikp.uni-koeln.de
- II. Physikalisches Institut
  www.ph2.uni-koeln.de

Publications

1. A. Accardo, A. Morisco, E. Gianolino, D. Tesauro, G. Mangiapia, A. Radulescu, A. Brandt and G. Morelli
Nanoparticles containing octreotide peptides and gadolinium complexes for MRI applications
J. Pept. Sci. 17, 154 (2011).

2. K. Achterhold, A. Ostermann, M. Moulin, M. Haertlein, T. Unruh and F. Parak
Dynamical properties of the hydration shell of fully deuterated myoglobin
Phys. Rev. E: Stat., Nonlinear, Soft Matter Phys. 84, 0419301 (2011).

3. T. Adams, S. Mühlbauer, C. Pfleiderer, F. Jonietz, A. Bauer, A. Neubauer, R. Georgii, P. Böni, U. Keiderling and A. Rosch
Long-range nature and particle-like properties of the skyrmion lattice in MnSi
Phys. Rev. Lett. 107, 217206 (2011).

4. J. Adelsberger, A. Meier-Koll, A. M. Bivigou-Koumba, P. Busch, O. Holderer, T. Hellweg, A. Laschewsky, P. Müller-Buschbaum and C. M. Papadakis
The collapse transition and the segmental dynamics in concentrated micellar solutions of P(S-b-NIPAM) diblock copolymers
Colloid Polym. Sci. 289, 711 (2011).

5. J. Altenkirch, J. Gibmeier, A. Kromm, T. Kannengiesser, T. Nitschke-Pagel and M. Hofmann
In situ study of structural integrity of low transformation temperature (LTT)-welds.
Mater. Sci. Eng. A 528, 5566 (2011).

6. J. Angelkort, A. Senyshyn, A. Schönleber and S. van Smaalen
Temperature-dependent neutron diffraction on TiI_3
Z. Kristallogr. 226, 640 (2011).

7. M.-S. Appavou, S. Busch, W. Doster, A. Gaspar and T. Unruh
The influence of 2 kbar pressure on the global and internal dynamics of human hemoglobin observed by quasielastic neutron scattering
Eur. Biophys. J. Biophys. Lett. 40, 705 (2011).

8. N. Arend and W. Häussler
A quantum-mechanical description of Rotating Field Spin Echo
Europhys. Lett. 96, 42001 (2011).

9. E. Babcock and A. Ioffe
Polarized ^{3}He neutron spin filter program at the JCNS
Physica B 406, 2448 (2011).

10. E. Babcock, S. Mattauch and A. Ioffe
High level of ^{3}He polarization maintained in an on-beam 3He spin filter using SEOP
Nucl. Instrum. Methods Phys. Res., Sect. A 625, 43 (2011).

11. J. Bahadur, D. Sen, S. Mazumder, S. Bhattacharya, H. Frielinghaus and G. Goerigk
Origin of Buckling Phenomenon during Drying of Micrometer-Sized Colloidal Droplets
Langmuir 27, 8404 (2011).

12. G. Bator, W. Sawka-Dobrowolska, L. Sobczyk, E. Grech, J. Nowicka-Scheibe, A. Pawlukojc, J. Wuttke, J. Baran and M. Owczarek
4,4'-, 5,5'-, and 6,6'-dimethyl-2,2'-bipyridyls: The structures, phase transitions, vibrations, and methyl group tunneling of their complexes with chloranilic acid
J. Chem. Phys. 135, 044509 (2011).

13. K. Beyer, T. Kannengiesser, A. Griesche and B. Schillinger
Study of hydrogen effusion in austenitic stainless steel by time-resolved in-situ measurements using neutron radiography
Nucl. Instrum. Methods Phys. Res., Sect. A 651, 211 (2011).

14. K. Beyer, T. Kannengiesser, A. Griesche and B. Schillinger
Neutron radiography study of hydrogen desorption in technical iron
J. Mater. Sci. 46, 5171 (2011).

15. R. Biehl, M. Monkenbusch and D. Richter
Exploring internal protein dynamics by neutron spin echo spectroscopy
Soft Matter 7, 1299 (2011).

16. G. Brandl, R. Georgii, W. Häussler, S. Mühlbauer and P. Böni
Large Scales - Long Times: Adding High Energy Resolution to SANS
Nucl. Instrum. Methods Phys. Res., Sect. A 654, 394 (2011).

17. H. Breitkreutz, X. Li, J. Burfeindt, H.-G. Bernhardt, P. Hoffmann, M. Trieloff, W. H. Schwarz, J. Hopp, E. K. Jessberger and H. Hiesinger
What happened to the moon? A lunar history mission using neutrons
*2nd International Conference on Advancements in Nuclear Instrumentation Measurement Methods and their Applications (ANIMMA), IEEE (*2011).

18. H. Breitkreutz and W. Petry
Thermal-hydraulic effects of cladding-meat contact faults
Transactions: RERTR-2011, Oct. 23 - 27, Santiago, Chile (2011).

19. K. Bressel, S. Prevost, M.-S. Appavou, B. Tiersch, J. Koetz and M. Gradzielski
Phase behaviour and structure of zwitanionic mixtures of perfluorocarboxylates and tetradecyldimethylamine oxide—dependence on chain length of the perfluoro surfactant
Soft Matter 7, 11232 (2011).

20. J. Brillo, A. Pommrich and A. Meyer
Relation between Self-Diffusion and Viscosity in Dense Liquids: New Experimental Results from Electrostatic Levitation
Phys. Rev. Lett. 107, 165902 (2011).

21. H.-G. Brokmeier, W. Gan, C. Randau, M. Völler, J. Rebelo-Kornmeier and M. Hofmann
Texture analysis at neutron diffractometer STRESS-SPEC
Nucl. Instrum. Methods Phys. Res., Sect. A 642, 87 (2011).

22. T. Brückel
Applications of Neutron Scattering - an Overview
Schriften des Forschungszentrum Jülich, Schlüsseltechnologien 27 (2011).

23. T. Brückel
Introduction: Neutron Scattering in Contemporary Research
Schriften des Forschungszentrum Jülich, Schlüsseltechnologien 27 (2011).

24. T. Brückel, G. Heger, D. Richter, G. Roth and R. Zorn (Eds.)
Laboratory Course Neutron Scattering (Experimental Manuals)
Schriften des Forschungszentrum Jülich, Schlüsseltechnologien 28 (2011).

25. T. Brückel, G. Heger, D. Richter, G. Roth and R. Zorn (Eds.)
Laboratory Course Neutron Scattering (Lectures)
Schriften des Forschungszentrum Jülich, Schlüsseltechnologien 27 (2011).

26. A. Brás, R. Pasquino, T. Koukoulas, G. Tsolou, O. Holderer, A. Radulescu, J. Allgaier, V. Mavrantzas, W. Pyckhout-Hintzen, A. Wischnewski, D. Vlassopoulos and D. Richter
Structure and dynamics of polymer rings by neutron scattering: breakdown of the Rouse model
Soft Matter 7, 11169 (2011).

27. J. Burghaus, M. Sougrati, A. Möchel, A. Houben, R. Hermann and R. Dronskowski
Local ordering and magnetism in $Ga_{0.9}Fe_{3.1}N$
J. Solid State Chem. 184, 2315 (2011).

28. P. Busch, M. Rauscher, J.-F. Moulin and P. Müller-Buschbaum
Debye-Scherrer rings from block copolymer films with powder-like order
J. Appl. Crystallogr. 44, 370 (2011).

29. S. Busch and T. Unruh
The slow short-time motions of phospholipid molecules with a focus on the influence of multiple scattering and fitting artifacts
J. Phys.: Condens. Matter 23, 254205 (2011).

30. S. Busch and T. Unruh
The Influence of Additives on the Nanoscopic Dynamics of the Phospholipid Dimyristoylphosphatidylcholine
Biochim. Biophys. Acta, Biomembr. 1808, 199 (2011).

31. H. Buschmann, J. Dolle, S. Berendts, A. Kuhn, P. Bottke, M. Wilkening, P. Heitjans, A. Senyshyn, H. Ehrenberg, A. Lotnyk, W. Duppel, L. Kienle and J. Janek
Structure and dynamics of the fast lithium ion conductor "$Li_7La_3Zr_2O_{12}$"
Phys. Chem. Chem. Phys. 13, 19378 (2011).

32. L. Butler, B. Schillinger, K. Ham, T. Dobbins, P. Liu and J. Vajo
Neutron imaging of a commercial Li-ion battery during discharge: Application of monochromatic imaging and polychromatic dynamic tomography
Nucl. Instrum. Methods Phys. Res., Sect. A 651, 320 (2011).

33. P. Böni, B. Roessli and K. Hradil
Inelastic neutron and x-ray scattering from incommensurate magnetic systems
J. Phys.: Condens. Matter 23, 254209 (2011).

34. T. Bücherl and C. Lierse von Gostomski
Real-time radiography at the NECTAR facility
Nucl. Instrum. Methods Phys. Res., Sect. A 651, 175 (2011).

35. T. Bücherl, C. Lierse von Gostomski, H. Breitkreutz, M. Jungwirth and F. Wagner
NECTAR—A fission neutron radiography and tomography facility
Nucl. Instrum. Methods Phys. Res., Sect. A 651, 86 (2011).

36. E. Calzada, F. Grünauer, B. Schillinger and H. Türck
Reusable shielding material for neutron- and gamma-radiation
Nucl. Instrum. Methods Phys. Res., Sect. A 651, 77 (2011).

37. L. Canella, P. Kudejova, R. Schulze, A. Türler and J. Jolie
Characterisation and optimisation of the new Prompt Gamma-ray Activation Analysis facility at FRM II
Nucl. Instrum. Methods Phys. Res., Sect. A 636, 108 (2011).

38. H. Ceeh, S. Gärtner, C. Hugenschmidt, K. Schreckenbach, D. Schwalm and P. Thirolf
Status report on the setup for the decay rate measurement of thenegative positronium ion
J. Phys.: Conf. Ser. 262, 012011 (2011).

39. H. Ceeh, C. Hugenschmidt, K. Schreckenbach, S. Gärtner, P. Thirolf, F. Fleischer and D. Schwalm
Precision measurement of the decay rate of the negative positronium ion Ps^-
Phys. Rev. A: At., Mol., Opt. Phys. 84, 062508 (2011).

40. J. Chang, N. Christensen, C. Niedermayer, K. Lefman, H. Rønnow, D. McMorrow, A. Schneidewind, P. Link, A. Hiess, M. Boehm, R. Mottl, S. Pailhés, N. Monomo, M. Oda, M. Ido and J. Mesot
Magnetic-Field-Induced Soft-Mode Quantum Phase Transition in the High-Temperature Superconductor $La_{1.855}Sr_{0.145}CuO_4$: An Inelastic Neutron-Scattering Study
Phys. Rev. Lett. 102, 177006 (2011).

41. L. Chang, W. Schweika, Y. Kao, Y. Chou, J. Persson, T. Brückel, H. Yang, Y. Chen and J. Gardner
Magnetic correlations in $Ho_xTb_{2-x}Ti_2O_7$
Phys. Rev. B: Condens. Matter Mater. Phys. 83, 144413 (2011).

42. L. Chang, Y. Su, Y.-J. Kao, Y. Chou, K. Kakurai, R. Mittal, H. Schneider, T. Brückel, G. Balakrishnan and M. Lees
The temperature evolution of the magnetic correlations in pure and diluted spin ice $Ho_{2-x}Y_xTi_2O_7$
Physica B 406, 2393 (2011).

43. R. Checchetto, N. Bazzanella, A. Kale, A. Miotello, S. Mariazzi, R. S. Brusa, P. Mengucci, C. Macchi, A. Somoza, W. Egger and L. Ravelli
Enhanced kinetics of hydride-metal phase transition in magnesium by vacancy clustering
Phys. Rev. B: Condens. Matter Mater. Phys. 84, 054115 (2011).

44. H.-Y. Chiang, R. Jungwirth, T. Zweifel, W. Schmid, W. Petry and F. Kraus
Interactions between UMo/Al fuel and diffusion barriers Nb and TiN under heavy ion irradiation
Transactions: RERTR-2011, Oct. 23 - 27, Santiago, Chile (2011).

45. F. Cámara, G. Gatta, M. Meven and D. Pasqual
Thermal expansion and high temperature structure evolution of zoisite by single-crystal X-ray and neutron diffraction
Phys. Chem. Miner. 39, 27 (2011).

46. G. D'Errico, L. Paduano, O. Ortona, G. Mangiapia, L. Coppola and F. Lo Celso
Temperature and concentration effects on supramolecular aggregation and phase behavior for poly(propylene oxide)–b-poly(ethylene oxide)–b-poly(propylene oxide) copolymers of different concentration in aqueous mixtures, 2
J. Colloid Interface Sci. 359, 179 (2011).

47. G. Danilyan, J. Klenke, V. Krakhotin, Y. N. Kopach, V. Novitsky, V. Pavlov and P. Shatalov
T-Odd Angular Correlations in the Emission of Prompt Gamma Rays and Neutrons in Nuclear Fission Induced by Polarized Neutrons
Phys. At. Nucl. 74, 671 (2011).

48. J. Davaasambuu, F. Güthoff, M. Hoelzel, A. Senyshyn, A. Radulescu and G. Eckold
Phase Behaviour of $CoCl_2$-$MnCl_2$ Mixed Crystals
Z. Phys. Chem. 225, 413 (2011).

49. K. Deng, X. Wang, W. Gan, Y. Wu, K. Wu, M. Zheng and H.-G. Brokmeier
Isothermal forging of AZ91 reinforced with 10 vol.% silicon carbon particles
Mater. Sci. Eng. A 528, 1707 (2011).

50. D. Doering, M. Deveaux, M. Domachowski, C. Dritsa, I. Froehlich, M. Koziel, C. Muentz, S. Ottersbach, F. Wagner and J. Stroth
Annealing studies on X-ray and neutron irradiated CMOS Monolithic Active Pixel Sensors
Nucl. Instrum. Methods Phys. Res., Sect. A 656, 133 (2011).

51. T. Doert, A. Schneidewind, M. Hoelzel, O. Stockert, D. Rutzinger and M. Ruck
Neutron scattering study of $CeAgAs_2$
J. Magn. Magn. Mater. 324, 1157 (2011).

52. S. Eijt, H. Leegwater, H. Schut, A. Anastasopol, W. Egger, L. Ravelli, C. Hugenschmidt and B. Dam
Layer-resolved study of the Mg to MgH_2 transformation in Mg–Ti films with

short-range chemical order
J. Alloys Compd. 509, S567 (2011).

53. M. Farajian, T. Nitschke-Pagel, R. C. Wimpory, M. Hofmann and M. Klaus
Residual stress field determination in welds by means of X-ray, synchrotron and neutron diffraction
Mat.-wiss. u. Werkstofftech. 42, 996 (2011).

54. R. Ferragut, A. Dupaquier, S. Brivio, R. Bertacco and W. Egger
Study of defects in an electroresistive Au/$La_{2/3}Sr_{1/3}MnO_3$/$SrTiO_3$(001) heterostructure by positron annihilation
J. Appl. Phys. 110, 053511 (2011).

55. A. Freund, S. Gsell, M. Fischer, M. Schreck, K. Andersen, P. Courtois, G. Borchert and M. Skoulatos
Diamond mosaic crystals for neutron instrumentation: First experimental results
Nucl. Instrum. Methods Phys. Res., Sect. A 634, S28 (2011).

56. S. Garny, V. Mares, H. Roos, F. Wagner and W. Rühm
Measurement of neutron spectra and neutron doses at the munich therapy beam with Bonner spheres
Radiat. Meas. 46, 92 (2011).

57. S. Garny, W. Rühm, M. Zankl, F. M. Wagner and H. G. Paretzke
First steps towards a fast-neutron therapy planning programme
Radiation Oncology 6, 163 (2011).

58. R. Georgii, G. Brandl, N. Arend, W. Häussler, A. Tischendorf, C. Pfleiderer, P. Böni and J. Lal
T**urn-key module for neutron scattering with sub-micro-eV resolution**
Appl. Phys. Lett. 98, 073505 (2011).

59. C. Gerstl, G. Schneider, W. Pyckhout-Hintzen, J. Allgaier, S. Willbold, D. Hofmann, U. Disko, H. Frielinghaus and D. Richter
Chain Conformation of Poly(alkylene oxide)s Studied by Small-Angle Neutron Scattering
Macromolecules 44, 6077 (2011).

60. R. Gilles, M. Hofmann, F. Johnson, Y. Gao, D. Mukherji, C. Hugenschmidt and P. Pikart
Analysis of antiphase domain growth in ternary FeCo alloys after different cooling rates and annealing treatments using neutron diffraction and positron annihilation
J. Alloys Compd. 509, 195 (2011).

61. R. Gilles, D. Mukherji, H. Eckerlebe, P. Strunz and J. Rösler
In situ investigation with neutrons on the evolution of γ′ precipitates at high temperatures in a single crystal Ni-base superalloy
Adv. Mater. Res. 278, 42 (2011).

62. A. Glavic, J. Voigt, J. Persson, Y. Su, J. Schubert, J. de Groot, W. Zande and T. Brückel
High quality $TbMnO_3$ films deposited on $YAlO_3$
J. Alloys Compd. 509, 5061 (2011).

63. G. Goerigk and Z. Varga
Comprehensive upgrade of the high-resolution small-angle neutron scattering instrument KWS-3 at FRM II
J. Appl. Crystallogr. 44, 337 (2011).

64. E. Goremychkin, R. Osborn, C. Wang, M. Lumsden, M. McGuire, A. Sefat, B. Sales, D. Mandrus, H. Rønnow, Y. Su and A. Christianson
Spatial inhomogeneity in $RFeAsO_{1-x}F_x$ (R= Pr, Nd) determined from rare-earth crystal-field excitations
Phys. Rev. B: Condens. Matter Mater. Phys. 83, 212505 (2011).

65. M. Granite, A. Radulescu, W. Pyckhout-Hintzen and Y. Cohen
Interactions between block copolymers and single-walled carbon nanotubes in aqueous solutions: a small-angle neutron scattering study
Langmuir 27, 751 (2011).

66. H. Greuner, B. Schillinger and C. Linsmeier
Neutron tomography as a new method for the three-dimensional structure analysis of CFC as plasma-facing material
Phys. Scr. 2011, 014074 (2011).

67. M. Grosse, M. Van Den Berg, C. Goulet, E. Lehmann and B. Schillinger
In-situ neutron radiography investigations of hydrogen diffusion and absorption in zirconium alloys
Nucl. Instrum. Methods Phys. Res., Sect. A 651, 253 (2011).

68. G. Gröger, W. Meyer-Zaika, C. Böttcher, F. Gröhn, C. Ruthard and C. Schmuck
Switchable Supramolecular Polymers from the Self-Assembly of a Small Monomer with Two Orthogonal Binding Interactions
J. Am. Chem. Soc. 133, 8961 (2011).

69. A. Gruening, M. Lebsanft and B. Scholtes
Residual Stress State in Tools Used for Thermo-mechanical Metal Forming Processes
Engineering Applications of Residual Stress, Conference Proceedings of the Society for Experimental Mechanics Series 8, 39 (2011)

70. J. Guo, T. Bücherl, Y. Zou and Z. Guo
Study on beam geometry and image reconstruction algorithm in fast neutron computerized tomography at NECTAR facility
Nucl. Instrum. Methods Phys. Res., Sect. A 651, 180 (2011).

71. J. Hampel, F. Boldt, H. Gerstenberg, G. Hampel, J. Kratz, S. Reber and N. Wiehl
Fast determination of impurities in metallurgical grade silicon for photovoltaics by instrumental neutron activation analysis
Appl. Radiat. Isot. 69, 1365 (2011).

72. S. Harms, K. Rätzke, C. Pakula, V. Zaporojtchenko, T. Strunskus, W. Egger, P. Sperr and F. Faupel
Free volume changes on optical switching in azobenzene-polymethylmethacrylate blends studied by a pulsed low-energy positron beam
J. Polym. Sci., Part B: Polym. Phys. 49, 404 (2011).

73. S. Harms, K. Rätzke, V. Zaporojtchenko, F. Faupel, W. Egger and L. Ravelli
Free volume distribution at the Teflon AF®/silicon interfaces probed by a slow positron beam
Polymer 52, 509 (2011).

74. L. Harriger, A. Schneidewind, S. Li, J. Zhao, Z. Li, W. Lu, X. Dong, F. Zhou, J. Hu and P. Dai
Transition from Three-Dimensional Anisotropic Spin Excitations to Two-Dimensional Spin Excitations by Electron Doping the FeAs-Based $BaFe_{1.96}Ni_{0.04}As_2$ Superconductor
Phys. Rev. Lett. 103, 087005 (2011).

75. A. Hasenstab, K. Frühwald, K. Osterloh and T. Bücherl
New Methods for NDT Testing of Wood (Ultrasonic Echo Technique, Radiografic Echo, Fast Neutrons)
Proceedings of the 17th International Nondestructive Testing and Evaluation of Wood Symposium, 753 (2011).

76. W. Häussler, P. Böni, M. Klein, C. Schmidt, U. Schmidt, F. Groitl and J. Kindervater
Detection of high frequency intensity oscillations at RESEDA using the CASCADE detector
Rev. Sci. Instrum. 82, 045101 (2011).

77. L. Helfen, F. Xu, B. Schillinger, E. Calzada, I. Zanette, T. Weitkamp and T. Baumbach
Neutron laminography—a novel approach to three-dimensional imaging of flat objects with neutrons
Nucl. Instrum. Methods Phys. Res., Sect. A 651, 135 (2011).

78. J. Herrero-Martín, C. Mazzoli, V. Scagnoli, L. Paolasini, H. Walker, Y. Xiao, T. Brueckel, R. Mittal, N. Kumar, S. Dhar, A. Thamizhavel and Y. Su
$EuFe_2As_2$: Magnetic Structure and Lo-

cal Charge Distribution Anisotropies as Seen by Resonant X-ray Scattering
J. Supercond. Nov. Magn. 24, 705 (2011).

79. K.-U. Hess, A. Flaws, M. Mühlbauer, B. Schillinger, A. Franz, M. Schulz, E. Calzada, D. Dingwell and K. Bente
Advances in high-resolution neutron computed tomography: Adapted to the earth sciences
Geosphere 7, 1294 (2011).

80. M. Hinterstein, M. Hoelzel, H. Kungl, M. Hoffmann, H. Ehrenberg and H. Fuess
***In situ* neutron diffraction study of electric field induced phase transitions in lanthanum doped lead zirconate titanate**
Z. Kristallogr. 226, 155 (2011).

81. O. Holderer, M. Klostermann, M. Monkenbusch, R. Schweins, P. Lindner, R. Strey, D. Richter and T. Sottmann
Soft fluctuating surfactant membranes in supercritical CO_2-microemulsions
Phys. Chem. Chem. Phys. 13, 3022 (2011).

82. C. Hugenschmidt
The status of the positron beam facility at NEPOMUC
J. Phys.: Conf. Ser. 262, 012002 (2011).

83. P. Hungler, L. Bennett, W. Lewis, M. Schulz and B. Schillinger
Neutron imaging inspections of composite honeycomb adhesive bonds
Nucl. Instrum. Methods Phys. Res., Sect. A 651, 250 (2011).

84. V. Hutanu, M. Meven, S. Masalovich, G. Heger and G. Roth
^{3}He spin filters for spherical neutron polarimetry at the hot neutrons single crystal diffractometer POLI-HEiDi
J. Phys.: Conf. Ser. 294, 012012 (2011).

85. V. Hutanu, A. Sazonov, H. Murakawa, Y. Tokura, B. Náfrádi and D. Chernyshov
Symmetry and structure of multiferroic $Ba_2CoGe_2O_7$
Phys. Rev. B: Condens. Matter Mater. Phys. 84, 212101 (2011).

86. W. Häussler, O. Holderer, T. Unruh and J. Wuttke
High-Resolution Neutron Spectroscopy at the FRM II
Neutron News 22, 24 (2011).

87. A. Ioffe, E. Babcock, V. Pipich and A. Radulescu
Wide-angle polarization analysis with ^{3}He for neutron scattering instrumentation at the JCNS
J. Phys.: Conf. Ser. 294, 012013 (2011).

88. N. Iqbal, J. Rolph, R. Moat, D. Hughes, M. Hofmann, J. Kelleher, G. Baxter, P. Withers and M. Preuss
A Comparison of Residual Stress Development in Inertia Friction Welded Fine Grain and Coarse Grain Nickel-Base Superalloy
Metall. Mater. Trans. A 42, 4056 (2011).

89. E. Juarez-Arellano, B. Winkler, S. Vogel, A. Senyshyn, D. Kammler and M. Avalos-Borja
In situ observation of the reaction of scandium and carbon by neutron diffraction
J. Alloys Compd. 509, 1 (2011).

90. R. Jungwirth, W. Petry, H. Breitkreutz, W. Schmid, H. Palancher, A. Bonnin, M. Grasse, C. Jarousse and B. Stepnik
Screening of different UMo/Al samples: protective oxide layers, Ti addition to the matrix and ternary U-Mo-X alloys
Transactions: RRFM-2011, March 20 - 24, Rome, Italy (2011).

91. R. Jungwirth, T. Zweifel, H.-Y. Chiang, W. Petry, S. van den Berghe and A. Leenaers
Heavy ion irradiation of UMo/Al samples with protective Si and ZrN layers (SELENIUM)
Transactions: RERTR-2011, Oct. 23 - 27, Santiago, Chile (2011).

92. F. Kargl, M. Engelhardt, F. Yang, H. Weis, P. Schmakat, B. Schillinger, A. Griesche and A. Meyer
***In situ* studies of mass transport in liquid alloys by means of neutron radiog-**

raphy
J. Phys.: Condens. Matter 23, 254201 (2011).

93. M. Kerscher, P. Busch, S. Mattauch, H. Frielinghaus, D. Richter, M. Belushkin and G. Gompper
Near-surface structure of a bicontinuous microemulsion with a transition region
Phys. Rev. E: Stat., Nonlinear, Soft Matter Phys. 83, 030401 (2011).

94. Y. Khaydukov, V. Aksenov, Y. Nikitenko, K. Zhernenkov, B. Nagy, A. Teichert, R. Steitz, A. Rühm and L. Bottyan
Magnetic Proximity Effects in V/Fe Superconductor/Ferromagnet Single Bilayer Revealed by Waveguide-Enhanced Polarized Neutron Reflectometry
J. Supercond. Nov. Magn. 24, 961 (2011).

95. A. Komarek, P. Böni and M. Braden
Parabolic versus elliptic focusing – Optimization of the focusing design of a cold triple-axis neutron spectrometer by Monte-Carlo simulations
Nucl. Instrum. Methods Phys. Res., Sect. A 647, 63 (2011).

96. A. Komarek, T. Moeller, M. Isobe, Y. Drees, H. Ulbrich, M. Azuma, M. Fernandez-Diaz, A. Senyshyn, M. Hoelzel, G. Andre, Y. Ueda, M. Grueninger and M. Braden
Magnetic order, transport and infrared optical properties in the $ACrO_3$ system (A = Ca, Sr, and Pb)
Phys. Rev. B: Condens. Matter Mater. Phys. 84, 125114 (2011).

97. T. Kordel, D. Holland-Moritz, F. Yang, J. Peters, T. Unruh, T. Hansen and A. Meyer
Neutron scattering experiments on liquid droplets using electrostatic levitation
Phys. Rev. B: Condens. Matter Mater. Phys. 83, 104205 (2011).

98. S. Kozhevnikov, A. Rühm and J. Major
Combination of a reflectometer and a nonmagnetic waveguide for experiments with polarized neutron microbeams
Crystallogr. Rep. 56, 1207 (2011).

99. S. Kozhevnikov, A. Rühm, F. Ott, N. Pleshanov and M. Major
Magnetic layered structure for the production of polarized neutron microbeams
Physica B 406, 2463 (2011).

100. A. Laumann, H. Boysen, M. Bremholm, K. T. Fehr, M. Hoelzel and M. Holzapfel
Lithium migration at high temperatures in $Li_4Ti_5O_{12}$ studied by neutron diffraction
Chem. Mater. 23, 2753 (2011).

101. A. Laumann, K.-T. Fehr, H. Boysen, M. Hoelzel and M. Holzapfel
Temperature-dependent structural transformations of hydrothermally synthetised cubic Li_2TiO_3 studied by *in-situ* neutron diffraction
Z. Kristallogr. 226, 53 (2011).

102. V. Lauter, P. Müller-Buschbaum, H. Lauter and W. Petry
Morphology of thin nanocomposite films of asymmetric diblock copolymer and magnetite nanoparticles
J. Phys.: Condens. Matter 23, 254215 (2011).

103. A. Leenaers, S. van den Berghe, W. van Renterghem, F. Charollais, P. Lemoine, C. **Larousse, A. Röhrmoser and W. Petry**
Irradiation behaviour of ground U(Mo) fuel with and without Si added to the matrix
J. Nucl. Mater. 412, 41 (2011).

104. J. Leist, H. Gibhardt, K. Hradil and G. Eckold
Switching behaviour of modulated ferroelectrics: the kinetics of the field induced lock-in transition in K_2SeO_4
J. Phys.: Condens. Matter 23, 305901 (2011).

105. S. Lenz, A. Rühm, J. Major, R. Berger and J. Gutmann
Softening of PMMA Brushes upon Collapse/Swelling Transition. A Combined

Neutron Reflectivity and Nanomechanical Cantilever Sensor Study
Macromolecules 44, 360 (2011).

106. S. Li, X. Lu, M. Wang, H.-q. Luo, M. Wang, C. Zhang, E. Faulhaber, L.-P. Regnault, D. Singh and P. Dai
Effect of the in-plane magnetic field on the neutron spin resonance in optimally doped $FeSe_{0.4}Te_{0.6}$ and $BaFe_{1.9}Ni_{0.1}As_2$ superconductors
Phys. Rev. B: Condens. Matter Mater. Phys. 84, 024518 (2011).

107. X. Li, H. Breitkreutz, J. Burfeindt, H.-G. Bernhardt, M. Trieloff, J. Hopp, E. Jessberger, W. Schwarz, P. Hoffmann and H. Hiesinger
Evaluation of neutron sources for ISAGE—in-situ-NAA for a future lunar mission
Appl. Radiat. Isot. 69, 1625 (2011).

108. X. Liu, R. Lin Peng, M. Hofmann, S. Johanssen and Y. Wang
In-Situ Neutron Diffraction Studies of Micromechanical Behavior in a Friction Stir Welded AA7475-T761
Metall. Mater. Trans. A 42, 89 (2011).

109. R. Lund, V. Pipich, L. Willner, A. Radulescu, J. Colmenero and D. Richter
Structural and thermodynamic aspects of the cylinder-to-sphere transition in amphiphilic diblock copolymers micelles
Soft Matter 7, 1491 (2011).

110. R. Lund, L. Willner, V. Pipich, I. Grillo, P. Lindner, J. Colmenero and D. Richter
Equilibrium Chain Exchange Kinetics of Diblock Copolymer Micelles: Effect of Morphology
Macromolecules 44, 6145 (2011).

111. A. Léon and J. Wuttke
Hydrogen Release from Sodium Alanate Observed by Time-resolved Neutron Backscattering
J. Phys.: Condens. Matter 23, 254214 (2011).

112. G. Mangiapia, C. Coppola, G. Vitiello, G. D'Errico, L. DeNapoli, A. Radulescu, D. Montesarchio and L. Paduano
Nanostructuring of CyPLOS (Cyclic Phosphate-Linked OligoSaccharides), novel saccharide-based synthetic ion transporters
J. Colloid Interface Sci. 354, 718 (2011).

113. G. Mangiapia, M. Vaccaro, G. D'Errico, H. Frielinghaus, A. Radulescu, V. Pipich, A. Carnerup and L. Paduano
Cubosomes for ruthenium complex delivery: formulation and characterization
Soft Matter 7, 10577 (2011).

114. M. Marques, A. Castanhola Batista, J. Rebelo-Kornmeier, M. Hofmann, J. Nobre and A. Loureiro
Residual Stress Fields after Heat Treatment in Cladded Steel of Process Vessels
Mater. Sci. Forum 681, 364 (2011).

115. S. Masalovich and O. Lykhvar
Tunable magnetostatic cavity for housing a ^{3}He neutron spin filter
J. Phys.: Conf. Ser. 294, 012016 (2011).

116. E. Metwalli, J.-F. Moulin, M. Rauscher, G. Kaune, M. Ruderer, U. Van Bürck, M. Haese-Seiller, R. Kampmann and P. Müller-Buschbaum
Structural investigation of thin diblock copolymer films using time-of-flight grazing-incidence small-angle neutron scattering
J. Appl. Crystallogr. 44, 84 (2011).

117. R. W. Metzke, H. Runck, C. A. Stahl, B. Schillinger, E. Calzada, M. Mühlbauer, M. Schulz, M. Schneider, H.-J. Priebe, W. A. Wall and J. Guttmann
Neutron computed tomography of rat lungs
Phys. Med. Biol. 56, N1 (2011).

118. D. Mikhailova, N. Bramnik, K. Bramnik, P. Reichel, S. Oswald, A. Senyshyn, D. Trots and H. Ehrenberg
Layered Li_xMoO_2 Phases with Different Composition for Electrochemical Appli-

cation: Structural Considerations
Chem. Mater. 23, 3429 (2011).

119. R. Mittal, S. K. Mishra, S. L. Chaplot, S. V. Ovsyannikov, E. Greenberg, D. M. Trots, L. Dubrovinsky, Y. Su, T. Brueckel, S. Matsuishi, H. Hosono and G. Garbarino
Ambient- and low-temperature synchrotron x-ray diffraction study of $BaFe_2As_2$ and $CaFe_2As_2$ at high pressures up to 56 GPa
Phys. Rev. B: Condens. Matter Mater. Phys. 83, 054503 (2011).

120. R. Mole, J. Stride, P. Henry, M. Hoelzel, A. Senyshyn, A. Alberola, C. Gomez-Garcia and P. Wood
Two Stage Magnetic Ordering and Spin Idle Behavior of the Coordination Polymer $Co_3(OH)_2(C_4O_4)_2{\cdot}3H_2O$ Determined Using Neutron Diffraction
Inorg. Chem. 50, 2246 (2011).

121. D. Mukherji, J. Rösler, P. Strunz, R. Gilles, G. Schumacher and S. Piegert
Beyond Ni-based superalloys: Development of CoRe-based alloys for gas turbine applications at very high temperatures
Int. J. Mater. Res. 2011, 1125 (2011).

122. S. Mühlbauer, C. Pfleiderer, P. Böni, E. Forgan, E. Brandt, A. Wiedenmann, U. Keiderling and G. Behr
Time-resolved stroboscopic neutron scattering of vortex lattice dynamics in superconducting niobium
Phys. Rev. B: Condens. Matter Mater. Phys. 83, 184502 (2011).

123. C. Müller, H. Gerstenberg and E. Gutsmiedl
Noise thermometer at the FRM II hot source
Transactions: RRFM-2011, March 20 - 24, Rome, Italy (2011).

124. P. Müller-Buschbaum, D. Magerl, R. Hengstler, J.-F. Moulin, V. Körstgens, A. Diethert, J. Perlich, S. Roth, M. Burghammer, C. Riekel, M. Gross, F. Varnik, P. Uhlmann, M. Stamm, J. Feldkamp and C. Schroer
Structure and flow of droplets on solid surfaces
J. Phys.: Condens. Matter 23, 184111 (2011).

125. B. Náfrádi, T. Keller, H. Manaka, A. Zheludev and B. Keimer
Low-temperature dynamics of magnons in a spin-1/2 ladder compound
Phys. Rev. Lett. 106, 177202 (2011).

126. T. Namsaraeva, B. Bazarov, D. Mikhailova, N. Kuratieva, A. Sarapulova, A. Senyshyn and H. Ehrenberg
Orthomolybdates in the Cs–$Fe^{II,III}$–Mo–O System: $Cs_4Fe(MoO_4)_3$, $Cs_2Fe_2(MoO_4)_3$ and $CsFe_5(MoO_4)_7$
Eur. J. Inorg. Chem. 2011, 2832 (2011).

127. S. Nandi, Y. Su, Y. Xiao, S. Price, X. F. Wang, X. H. Chen, J. Herrero-Martín, C. Mazzoli, H. C. Walker, L. Paolasini, S. Francoual, D. K. Shukla, J. Strempfer, T. Chatterji, C. M. N. Kumar, R. Mittal, H. M. Rønnow, C. Rüegg, D. F. McMorrow and T. Brückel
Strong coupling of Sm and Fe magnetism in SmFeAsO as revealed by magnetic x-ray scattering
Phys. Rev. B: Condens. Matter Mater. Phys. 84, 054419 (2011).

128. H.-Y. Nguyen, S. Keating, G. Bevan, A. Gabov, M. Daymond, B. Schillinger and A. Murray
Seeing through Corrosion: Using Microfocus X-ray Computed Tomography and Neutron Computed Tomography to Digitally "Clean" Ancient Bronze Coins
MRS Proceedings 1319, (2011).

129. K. Nusser, G. Schneider, W. Pyckhout-Hintzen and D. Richter
Viscosity Decrease and Reinforcement in Polymer–Silsesquioxane Composites
Macromolecules 44, 7820 (2011).

130. I.-H. Oh, M. Meven, G. Heger and K.-S. Lee
Neutron Diffraction Analysis of a Single-Crystal Structure of $Rb_{0.51}Tl_{0.49}H_2PO_4$
J. Phys. Soc. Jpn. 80, 084602 (2011).

131. K. Osterloh, T. Bücherl, C. Lierse von Gostomski, U. Zscherpel, U. Ewert and S. Bock
Filtering algorithm for dotted interferences
Nucl. Instrum. Methods Phys. Res., Sect. A 651, 171 (2011).

132. K. Osterloh, D. Fratzscher, M. Jechow, T. Bücherl, B. Schillinger, A. Hasenstab, U. Zscherpel and U. Ewert
Limited View Tomography of Wood with Fast and Thermal Neutrons
International Symposium on Digital Industrial Radiology and Computed Tomography, June 20 - 22, Berlin, Germany (2011)

133. K. Osterloh, D. Fratzscher, A. Schwabe, B. Schillinger, U. Zscherpel and U. Ewert
Radiography and partial tomography of wood with thermal neutrons
Nucl. Instrum. Methods Phys. Res., Sect. A 651, 236 (2011).

134. H. Palancher, A. Bonnin, T. Zweifel, F. Charollais, M. Anselmet, P. Lemoine, V. Honkimäki, T. Buslaps, W. Petry, R. Jungwirth, M. Grasse and B. Stepnik
Quantitative crystallographic analysis of as-fabricated full size IRIS/E-FUTURE nuclear fuel plates
Transactions: RERTR-2011, Oct. 23 - 27, Santiago, Chile (2011).

135. L. C. Pardo, M. Rovira-Esteva, S. Busch, J.-F. Moulin and J. Tamarit
Fitting in a complex χ^2 landscape using an optimized hypersurface sampling
Phys. Rev. E: Stat., Nonlinear, Soft Matter Phys. 84, 046711 (2011).

136. L. Pardo, M. Rovira-Esteva, S. Busch, M. Ruiz-Martin and J. Tamarit
FABADA: a Fitting Algorithm for Bayesian Analysis of DAta
J. Phys.: Conf. Ser. 325, 012006 (2011).

137. I. Perić, C. Takacs, J. Behr, F. Wagner and P. Fischer
The first beam test of a monolithic particle pixel detector in high-voltage CMOS technology
Nucl. Instrum. Methods Phys. Res., Sect. A 628, 287 (2011).

138. L. Peyker, c. Gold, W. Scherer, H. Michor, T. Unruh, G. G. Simeoni, A. Senyshyn, D. T. Adroja, O. Stockert and E.-W. Scheidt
Change of the effective spin degeneracy in $CeNi_{9-x}Cu_xGe_4$ due to the interplay between Kondo and crystal field effects
Europhys. Lett. 93, 37006 (2011).

139. P. Pikart, C. Hugenschmidt, M. Horisberger, Y. Matsukawa, M. Hatakeyama, T. Toyama and Y. Nagai
Positron annihilation in Cr, Cu, and Au layers embedded in Al and quantum confinement of positrons in Au clusters
Phys. Rev. B: Condens. Matter Mater. Phys. 84, 014106 (2011).

140. C. Piochacz and C. Hugenschmidt
The experimental determination of the phase space distribution of a positron beam
J. Phys.: Conf. Ser. 262, 012049 (2011).

141. S. Prevost, S. Riemer, W. Fischer, R. Haag, C. Böttcher, J. Gummel, I. Grillo, M.-S. Appavou and M. Gradzielski
Colloidal Structure and Stability of DNA/Polycations Polyplexes Investigated by Small Angle Scattering
Biomacromolecules 12, 4272 (2011).

142. A. Radulescu, D. Schwahn, J. Stellbrink, M. Monkenbusch, L. J. Fetters and D. Richter
Microstructure and morphology of self-assembling multiblock poly(ethylene-1-butene)-n copolymers in solution studied by wide-Q small-angle neutron scattering and microscopy
J. Polym. Sci., Part B: Polym. Phys. 49, 144 (2011).

143. M. Raichle, D. Reznik, D. Lamago, R. Heid, Y. Li, M. Bakr, C. Ulrich, V. Hinkov, K. Hradil, C. Lin and B. Keimer
Highly anisotropic anomaly in the dispersion of the copper-oxygen bond-bending phonon in superconducting $YBa_2Cu_3O_7$ from inelastic neutron scat-

tering
Phys. Rev. Lett. 107, 177004 (2011).

144. R. Ranjan, V. Kothai, A. Senyshyn and H. Boysen
Neutron diffraction study of the coupling between spin, lattice, and structural degrees of freedom in $0.8BiFeO_3$-$0.2PbTiO_3$
J. Appl. Phys. 109, 063522 (2011).

145. R. Ranjan, A. Senyshyn, R. Garg and H. Boysen
Magnetic structure and magneto-elastic-structural coupling in Cr-modified $SrRuO_3$: A neutron powder diffraction study
J. Appl. Phys. 109, 073908 (2011).

146. J. Rebelo Kornmeier, J. Gibmeier and M. Hofmann
Minimization of spurious strains by using a Si bent-perfect-crystal monochromator: neutron surface strain scanning of a shot-peened sample
Meas. Sci. Technol. 22, 065705 (2011).

147. J. Rebelo-Kornmeier, J. Gibmeier, M. Hofmann and R. Wimpory
Neutron surface residual stress scanning using optimisation of a Si bent perfect crystal monochromator for minimising spurious strains
Mater. Sci. Forum 681, 399 (2011).

148. G. Redhammer, A. Senyshyn, G. Tippelt and G. Roth
Magnetic spin structure of pyroxene-type $MnGeO_3$
J. Phys.: Condens. Matter 23, 254202 (2011).

149. K. Rećko, L. Dobrzyński, A. Senyshyn, H. Fuess, K. Szymański, B. Kotur and W. Suski
Structural and magnetic properties of $Sc_{1.1}Fe_{3.9}Al_8$ alloy
J. Magn. Magn. Mater. 323, 1860 (2011).

150. J. Robinson, D. Tanner, C. Trueman and R. Wimpory
Measurement and Prediction of Machining Induced Redistribution of Residual Stress in the Aluminium Alloy 7449
Exp. Mech. 51, 981 (2011).

151. M. Rovira-Esteva, A. Murugan, L. Pardo, S. Busch, J. Tamarit, S. Pothoczki, G. Cuello and F. Bermejo
Interplay between intramolecular and intermolecular structures of 1,1,2,2-tetrachloro-1,2-difluoroethane
Phys. Rev. B: Condens. Matter Mater. Phys. 84, 064202 (2011).

152. C. Ruthard, M. Maskos, U. Kolb and F. Gröhn
Polystyrene Sulfonate–Porphyrin Assemblies: Influence of Polyelectrolyte and Porphyrin Structure
J. Phys. Chem. B 115, 5716 (2011).

153. V. Ryzhkovsky, V. Goncharov, S. Agafonov, V. Glazkov, V. Somenkov, A. Sazonov and A. Senyshyn
Magnetic Ordering in Mn_3Sb Determined by Neutron Diffraction Data
Journal of Surface Investigation: X-ray, Synchrotron and Neutron Techniques 5, 109 (2011).

154. A. Sanz, A. Nogales, T. Ezquerra, W. Häussler, M. Soccio, N. Lotti and A. Munari
Homogeneous Dynamics within Inhomogeneous Environment in Semicrystalline Polymers
Macromolecules 44, 8124 (2011).

155. B. Schillinger and G. Badurek
First study of macroscopic neutron dark field imaging using scattering grids
Nucl. Instrum. Methods Phys. Res., Sect. A 651, 197 (2011).

156. B. Schillinger, E. Calzada, C. Eulenkamp, G. Jordan and W. Schmahl
Dehydration of moulding sand in simulated casting process examined with neutron radiography
Nucl. Instrum. Methods Phys. Res., Sect. A 651, 312 (2011).

157. B. Schillinger, H. Greuner and C. Linsmeier
Neutron computed tomography of plasma facing components for fusion

experiments
Nucl. Instrum. Methods Phys. Res., Sect. A 651, 202 (2011).

158. W. Schmid, S. Dirndorfer, R. Jungwirth, H. Juranowitsch, W. Petry and T. Zweifel
Tailored model systems for IDL investigation and diffusion barrier optimization
Transactions: RRFM-2011, March 20 - 24, Rome, Italy (2011).

159. L. Schmitt, J. Kling, M. Hinterstein, M. Hoelzel, W. Jo, H.-J. Kleebe and H. Fuess
Structural investigations on lead-free $Bi_{1/2}Na_{1/2}TiO_3$-based piezoceramics
J. Mater. Sci. 46, 4368 (2011).

160. T. Schmitz, K. Appelman, P. Kudejova, C. Schütz, J. Kratz, R. Moss, G. Otto and G. Hampel
Determination of boron concentration in blood and tissue samples from patients with liver metastases of colorectal carcinoma using Prompt Gamma Ray Activation Analysis (PGAA)
Appl. Radiat. Isot. 69, 936 (2011).

161. Schulz, V. Sumerin, S. Heikkinen, B. Pedersen, C. Wang, M. Atsumi, M. Leskelä, T. Repo, P. Pyykkö, W. Petry and B. Rieger
Molecular Hydrogen Tweezers: Structure and Mechanisms by Neutron Diffraction, NMR, and Deuterium Labeling Studies in Solid and Solution
J. Am. Chem. Soc. 133, 20245 (2011).

162. Schulz, P. Schmakat, C. Franz, A. Neubauer, E. Calzada, B. Schillinger, P. Böni and C. Pfleiderer
Neutron depolarisation imaging: Stress measurements by magnetostriction effects in Ni foils
Physica B 406, 2412 (2011).

163. M. Schöbel, W. Altendorfer, H. Degischer, S. Vaucher, T. Buslaps, M. Di Michiel and M. Hofmann
Internal stresses and voids in SiC particle reinforced aluminum composites for heat sink applications
Compos. Sci. Technol. 71, 724 (2011).

164. N. Semioshkina, I. Fiedler, B. Schillinger, A. Ulanovsky, V. Potapov, O. Ivanov, F. Wagner and U. Gerstmann
Comparison of three non-destructive methods to measure ^{90}Sr in human tooth samples
Radiat. Meas. 46, 1897 (2011).

165. D. Sen, J. Melo, J. Bahadur, S. Mazumder, S. Bhattacharya, S. D'Souza, H. Frielinghaus, G. Goerigk and R. Loidl
Arrest of morphological transformation during evaporation-induced self-assembly of mixed colloids in micrometric droplets by charge tuning
Soft Matter 7, 5423 (2011).

166. A. Senyshyn, M. Hoelzel, T. Hansen, L. Vasylechko, V. Mikhailik, H. Kraus and H. Ehrenberg
Thermal structural properties of calcium tungstate
J. Appl. Crystallogr. 44, 319 (2011).

167. M. Serb, R. Wang, M. Meven and U. Englert
The Whole Range of Hydrogen Bonds in One Crystal Structure: Neutron Diffraction and Charge Density Studies of N, N-Dimethylbiguanidinium-Bis(hydrogensquarate)
Acta Crystallogr., Sect. B: Struct. Sci. 67, 552 (2011).

168. L. Simeone, G. Mangiapia, C. Irace, A. Di Pascale, A. Colonna, O. Ortona, L. De Napoli, D. Montesarchio and L. Paduano
Nucleolipid nanovectors as molecular carriers for potential applications in drug delivery
Mol. BioSyst. 7, 3075 (2011).

169. A. Singh, A. Senyshyn, H. Fuess, T. Chatterji and D. Pandey
Neutron powder diffraction study of nuclear and magnetic structures of multiferroic $(Bi_{0.8}Ba_{0.2})(Fe_{0.8}Ti_{0.2})O_3$: Evidence for isostructural phase transition and magnetoelastic and magnetoelectric couplings
Phys. Rev. B: Condens. Matter Mater. Phys. 83, 054406 (2011).

170. A. Singh, A. Senyshyn, H. Fuess and D. Pandey
Ferroelectric and antiferrodistortive phase transition in the multiferroic $(Bi_{0.8}Ba_{0.2})(Fe_{0.8}Ti_{0.2})O_3$: A high temperature neutron powder diffraction study
J. Appl. Phys. 110, 024111 (2011).

171. I. Siouris, R. Kremer and M. Hoelzel
Antiferromagnetic order and spin glass behaviour in Dy_2CuIn_3
J. Magn. Magn. Mater. 323, 2903 (2011).

172. V. Slugen, V. Krsjak, W. Egger, M. Petriska, S. Sojak and J. Veternikova
Fe-Cr alloys behavior after helium implantation
J. Nucl. Mater. 409, 163 (2011).

173. Y. Sohn, K. Sparta, M. Meven and G. Heger
Disorder of $(NH_4)_3H(SO_4)_2$ in the high-temperature phase I
Acta Crystallogr., Sect. B: Struct. Sci. 67, 116 (2011).

174. D. Sokolov, R. Ritz, C. Pfleiderer, T. Keller and A. Huxley
Neutron scattering studies of the lattice expansion in a ferromagnetic superconductor UGe_2 under pressure
J. Phys.: Conf. Ser. 273, 012085 (2011).

175. P. Steffens, O. Friedt, Y. Sidis, P. Link, J. Kulda, K. Schmalzl, S. Nakatsuji and M. Braden
Magnetic excitations in the metallic single-layer ruthenates $Ca_{2-x}Sr_xRuO_4$ studied by inelastic neutron scattering
Phys. Rev. B: Condens. Matter Mater. Phys. 83, 054429 (2011).

176. C. Stock, L. Chapon, A. Schneidewind, Y. Su, P. Radaelli, D. McMorrow, A. Bombardi, N. Lee and S.-W. Cheong
Helical spin waves, magnetic order, and fluctuations in the langasite compound $Ba_3NbFe_3Si_2O_{14}$
Phys. Rev. B: Condens. Matter Mater. Phys. 83, 104426 (2011).

177. R. Stoepler, A. Frei, S. Paul, H. Gerstenberg and W. Petry
The ultracold laboratory at the FRM II
Transactions: RRFM -2011, March 20 - 24, Rome, Italy (2011).

178. M. Strobl, A. Hilger, M. Boin, N. Kardjilov, R. Wimpory, D. Clemens, M. Mühlbauer, B. Schillinger, T. Wilpert, C. Schulz, K. Rolfs, C. Davies, N. O'Dowd, P. Tiernan and I. Manke
Time-of-flight neutron imaging at a continuous source: Proof of principle using a scintillator CCD imaging detector
Nucl. Instrum. Methods Phys. Res., Sect. A 651, 149 (2011).

179. S. Stuiber, G. Wu, J. Nehrkorn, J. Dreiser, Y. Lan, G. Novitchi, C. E. Anson, T. Unruh, A. K. Powell and O. Waldmann
Inelastic Neutron Scattering on an Mn10 Supertetrahedron: Assessment of Exchange Coupling Constants, Ferromagnetic Spin Waves and an Analogy to the Hückel Method
Chem. Eur. J. 17, 9094 (2011).

180. X. Tang, A. Houben, X. Liu, L. Stork and R. Dronskowski
Crystal Structure Refinement of $M(NCNH)_2$ (M = Fe, Co) Based on Combined Neutron and X-ray Diffraction Data
Z. Anorg. Allg. Chem. 637, 1089 (2011).

181. P. Uhlmann, F. Varnik, P. Truman, G. Zikos, J.-F. Moulin, P. Müller-Buschbaum and M. Stamm
Microfluidic emulsion separation—simultaneous separation and sensing by multilayer nanofilm structures
J. Phys.: Condens. Matter 23, 184123 (2011).

182. M. Valldor, R. Hermann, J. Wuttke, M. Zamponi and W. Schweika
Spin correlation in the extended kagome system $YBaCo_3FeO_7$
Phys. Rev. B: Condens. Matter Mater. Phys. 84, 224426 (2011).

183. M. Valldor, O. Heyer, A. Komarek, A. Senyshyn, M. Braden and T. Lorenz

Magnetostrictive Neel ordering of the spin-5/2 ladder compound $BaMn_2O_3$: Distortion-induced lifting of geometrical frustration
Phys. Rev. B: Condens. Matter Mater. Phys. 83, 024418 (2011).

184. C. Wang, S. Baker, M. Lumsden, S. Nagler, W. Heller, G. Baker, P. Deen, M. Cranswick, Y. Su and A. Christianson
Antiferromagnetic order in MnO spherical nanoparticles
Phys. Rev. B: Condens. Matter Mater. Phys. 83, 214418 (2011).

185. L. Wang, U.-C. Sou, H. Yang, L. Chang, C.-M. Cheng, K.-D. Tsuei, Y. Su, T. Wolf and P. Adelmann
Mixed-state Hall effect and flux pinning in $Ba(Fe_{1-x}Co_x)_2As_2$ single crystals (x=0.08 and 0.10)
Phys. Rev. B: Condens. Matter Mater. Phys. 83, 134506 (2011).

186. S. Wellert, M. Karg, O. Holderer, A. Richardt and T. Hellweg
Temperature dependence of the surfactant film bending elasticity in a bicontinuous sugar surfactant based microemulsion: a quasielastic scattering study
Phys. Chem. Chem. Phys. 13, 3092 (2011).

187. S. Wellert, B. Tiersch, J. Koetz, A. Richardt, A. Lapp, O. Holderer, J. Gäb, M.-M. Blum, C. Schulreich, R. Stehle and T. Hellweg
The DFPase from Loligo vulgaris in sugar surfactant-based bicontinuousmicroemulsions: structure, dynamics, and enzyme activity
Eur. Biophys. J. 40, 243 (2011).

188. S. E. Wolf, J. Leiterer, V. Pipich, R. Barrea, F. Emmerling and W. Tremel
Strong Stabilization of Amorphous Calcium Carbonate Emulsion by Ovalbumin: Gaining Insight into the Mechanism of 'Polymer-Induced Liquid Precursor' Processes
J. Am. Chem. Soc. 133, 12642 (2011).

189. Z. Wu, V. Gogonea, X. Lee, R. May, V. Pipich, M. Wagner, A. Undurti, T. Tallant, C. Baleanu-Gogonea, F. Charlton, A. Ioffe, J. DiDonato, K.-A. Rye and S. Hazen
The Low Resolution Structure of ApoA1 in Spherical High Density Lipoprotein Revealed by Small Angle Neutron Scattering
J. Biol. Chem. 286, 12495 (2011).

190. J. Wuttke
Macromolecular Systems in Soft and Living Matter, Lecture notes of the 42nd IFF Spring School 2011
Schriften des Forschungszentrum Jülich, Schlüsseltechnologien 20 (2011).

191. X. Xia, E. Metwalli, M. A Ruderer, V. Körstgens, P. Busch, P. Böni and P. Müller-Buschbaum
Nanostructured diblock copolymer films with emhbedded magnetic nanoparticles
J. Phys.: Condens. Matter 23, 254203 (2011).

192. Y. Xiao, Y. Su, C. Kumar, C. Ritter, R. Mittal, S. Price, J. Perßon and T. Brückel
Physical properties, crystal and magnetic structure of layered $Fe_{1.11}Te_{1-x}Se_x$ superconductors
Eur. Phys. J. B 82, 113 (2011).

193. F. Yang, J. Kaplonski, T. Unruh, E. Mamontov and A. Meyer
A high temperature high pressure cell for quasielastic neutron scattering
Rev. Sci. Instrum. 82, 083903 (2011).

194. F. Yang, T. Kordel, D. Holland-Moritz, T. Unruh and A. Meyer
Structural relaxation as seen by quasielastic neutron scattering on viscous Zr–Ti–Cu–Ni–Be droplets
J. Phys.: Condens. Matter 23, 254207 (2011).

195. Y. Zou, B. Schillinger, S. Wang, X. Zhang, Z. Guo and Y. Lu
Coded source neutron imaging with a MURA mask
Nucl. Instrum. Methods Phys. Res., Sect. A 651, 192 (2011).

196. T. Zweifel, H. Palancher, R. Jungwirth, A. Bonnin, W. Petry, M. Anselmet, F. Charollais, P. Lemoine and L. Beck
Heavy ion irradiation on UMo/Al systems: temperature influence
Transactions: RRFM-2011, March 20 - 24, Rome, Italy (2011).

Theses

Doctoral theses

C. Bernards
Investigation and supersymmetric description of even-even mercury isotopes
Universität zu Köln (2011).

H. Breitkreutz
Coupled Neutronics and Thermohydraulics of High Density Cores at FRM II
Technische Universität München (2011).

L. Canella
Optimisation of the PGAA instrument at FRM II for low background and 2D measurements
Technische Universität München (2011).

Z. Fu
Spin correlations and excitations in spin frustrated molecular and molecule-based magnets
Rheinisch-Westfälische Technische Hochschule Aachen (2011).

C. Gerstl
Kettenformation und Dynamik verschiedener Poly(alkylenoxid)e
Westfälische Wilhelms-Universität Münster (2011).

A. Glavic
Multiferroicity in oxide thin films and heterostructures
Rheinisch-Westfälische Technische Hochschule Aachen (2011).

D. Haug
The Magnetic Phase Diagram of Underdoped $YBa_2Cu_3O_{6+x}$ studied by Neutron Scattering
Universität Stuttgart (2011)

R. Jungwirth
Irradiation behaviour of modified high-performance nuclear fuels
Technische Universität München (2011).

M. Kerscher
Wässrige Tensidsysteme und Mikroemulsionen in der Gegenwart von Oberflächen
Westfälische Wilhelms-Universität Münster (2011).

G. Meierhofer
Neutron capture on 76-Ge
Eberhard Karls Universität Tübingen (2011).

A. Möchel
Lattice dynamics in thermoelectric Zintl phases
Université de Liège, Belgium (2011).

K. Nusser
Struktur und Dynamik von Polymeren in Anwesenheit repulsiver Nanoteilchen
Westfälische Wilhelms-Universität Münster (2011).

Katharina Rolfs
Influence of the alloying element cobalt on the key properties of ferromagnetic shape memory Ni-Mn-Ga single crystals
Technische Universität München (2011).

W. Schmid
Construction of a sputtering reactor for the coating and processing of monolithic U-Mo nuclear fuel
Technische Universität München (2011).

M. Tegel
Iron Pnictide Superconductors
Ludwig-Maximilians-Universität München (2011).

Diploma theses

W. Feldmeier
Numerical investigation of a new ^{129}Xe EDM experiment
Technische Universität München (2011).

M. González Marti
Assessment and further development of pro-

grams for medical therapy using fission neutrons
Technische Universität München (2011).

A. Hamm
Dynamik von Silica gefüllten Polymeren untersucht mittels dielektrischer Spektroskopie und rheologischen Methoden
Universität Regensburg (2011).

T. Huber
Transport and Storage of Ultra-cold Neutrons in Replika Guides
Technische Universität München (2011).

G. Kessler
Magnetic trapping of high-field seeking UCN spin states
Technische Universität München (2011).

E. Lachner
Aufbau einer Sputterkammer zur Präparation dünner Metallschichten
Technische Universität München (2011).

J. Reim
Spindynamik im Schwedenborgit $CaBaCo_2Fe_2O_7$: Untersuchung mit Neutronenstreuung und Spinwellentheorie
Rheinisch-Westfälische Technische Hochschule Aachen (2011).

M. Reiner
Depth resolved Doppler broadening spectroscopy of thin metallic films with a mono energetic positron beam
Technische Universität München (2011).

E. Rosén
Magnetische Eigenschaften und Spinkorrelationen in Co und Fe basierten Swedenborgit-Kristallen
Rheinisch-Westfälische Technische Hochschule Aachen (2011).

J. Sarvas
Optimisation of high density fuel elements for FRM II
Technische Universität München (2011).

P. Schmakat
Neutronen-Depolarisationsmessungen am Kondo-System $CePd_{1-x}Rh_x$ bei tiefen Temperaturen
Technische Universität München (2011).

J. Schmidt
Einfluß von Alpha-Synuclein auf Struktur und Diffusität substratgestützter Membranen
Ludwig-Maximilians-Universität München (2011).

J. Schön
Towards a measurement of the bound beta decay of the neutron
Technische Universität München (2011).

C. Steyer
Sputterdeposition zur Beschichtung von sphärischem UMo Kernbrennstoffpulver
Technische Universität München (2011).

B. Taubenheim
Towards a new ^{129}Xe EDM experiment
Technische Universität München (2011).

S. Wlokka
Die neue UCN-Quelle am FRM II – Produktion ultrakalter Neutronen mit Kryo-Konvertern und Betrachtung ausgewählter Sicherheitsaspekte
Technische Universität München (2011).

Master theses

P. Lazaropoulou
Non Destructive study of ancient metallic artifacts using SEM-EDS, PGAA and SR-XRD
Democritus university of Thrace, Greece (2011).

Bachelor theses

B. Baumeister
Reinigungsverfahren für metallische Uran-Molybdän Kernbrennstoffe
Technische Universität München (2011).

J. Frisch
Monte-Carlo-Simulationen für die Optimierung fokussierender Neutronenleiter
Technische Universität München (2011).

L. Fuchs
Kompensation von externen Magnetfeldern

für das Neutron EDM experiment
Technische Universität München (2011).

T. Greese
Characterization of a Tritium Detector for the Determination of Tritium Activities in $^{4}He/^{3}H$-Mixtures
Technische Universität München (2011).

A. Himpsl
Entwicklung einer Apparatur zur präzisen Ausrichtung eines Cs-Atommagnetometers
Technische Universität München (2011).

M. Huber
Manipulation of the kinetic quantities of a slow neutron beam
Technische Universität München (2011).

L. Kredler
Monte-Carlo simulations for RESEDA: The new CASCADE detector and planned extensions
Technische Universität München (2011).

M.-N. Newrzella
Calculation of a low-field NMR system
Technische Universität München (2011).

S. Obermeier
Entwicklung einer Fernsteuerung zur Bedienung von Maschinenachsen auf Basis eines Atmel AT90USB Mikrocontrollers
Hochschule für Angewandte Wissenschaften München (2011).

S. Reinl
Entwicklung und Konstruktion eines RF-Sputterkopfes
Hochschule für Angewandte Wissenschaften München (2011).

A.-K. Straub
Adiabatischer Transport von laserpolarisiertem Xenon
Technische Universität München (2011).

R. Thiele
Simulation eines Spinpräzessionsexperimentes für Neutronen
Technische Universität München (2011).

Miscellaneous

P. Baur
Neutronenstrukturmessung von Glukosekristallen
Facharbeit, Otto-von-Taube Gymnasium, Gauting (2011).

C. Fuchs
Konstruktion einer neuen HF-Spule für einen NRSE Flipper
Semesterarbeit, Hochschule für Angewandte Wissenschaften München (2011).

Imprint

Publisher:

Technische Universität München
Forschungs-Neutronenquelle
Heinz Maier-Leibnitz (FRM II)
Lichtenbergstr. 1
85747 Garching
Germany

Phone: +49.89.289.14966
Fax: +49.89.289.14995
Internet: www.frm2.tum.de
E-mail: userinfo@frm2.tum.de

Photographic credits:

Uli Benz, TUM
pages 8 (2), 85

Astrid Eckert, Andreas Heddergott, TUM
pages 5, 6 (3), 9 (1), 13, 14, 17 (2), 42, 73, 83

Wenzel Schürmann, TUM
pages 6 (1), 8 (1), 9 (1), 10 (2), 11 (2), 15, 29, 35, 67, 84 (1), 86 (1), 87 (1), 98

Other images: editors, authors, TUM

Editors:

Dr. Henrich Frielinghaus
Dr. Connie Hesse
Elisabeth Jörg-Müller
Dr. Ina Lommatzsch
Dr. Jürgen Neuhaus
Dr. Andreas Ostermann
Dr. Bjørn Pedersen
Petra Riedel
Dr. Astrid Schneidewind
Andrea Voit

Design and graphics:

Ramona Bucher
Sabrina Kressierer, TUM
Benjamin Sanchez

Typesetting:

Ramona Bucher
Dr. Connie Hesse
Andrea Voit